

Diffusion and Conformational Dynamics of Semiflexible Macromolecules and Supramolecular Assemblies on Lipid Membranes

Dissertation

zur Erlangung des akademischen Grades
Doctor rerum naturalium
(Dr. rer. nat.)

vorgelegt
der Fakultät Mathematik und Naturwissenschaften
der Technischen Universität Dresden

von

Christoph Herold

geboren am 18.09.1982 in Dresden, Deutschland.

Gutachter: Prof. Dr. Petra Schwille und Prof. Dr. Josef A. Käs

Eingereicht am: 08. Juni 2012

Tag der Verteidigung: 07. November 2012

“You have to be patient, and single molecules will come to you.”

Claus Seidel

Publications

Parts of this work have been communicated in the following publications:

C. Herold, P. Schwille and E. P. Petrov.

DNA condensation at freestanding cationic lipid bilayers.

Phys. Rev. Lett. **104**, 148102, 2010.

C. Herold, G. Chwastek, P. Schwille and E. P. Petrov.

Efficient electroformation of supergiant unilamellar vesicles containing cationic lipids on ITO-coated electrodes.

Langmuir **28**, 5518-5521, 2012.

Abstract

Understanding the interaction of polyelectrolytes with oppositely charged lipid membranes is an important issue of soft matter physics, which provides an insight into mechanisms of interactions between biological macromolecules and cell membranes. Despite the fact that many (bio)macromolecules and filamentous supramolecular assemblies show semiflexible behavior, prior to this work very little was known about the conformational dynamics and Brownian motion of semiflexible particles attached to freestanding lipid membranes. In order to address these issues, diffusion and conformational dynamics of semiflexible DNA molecules and filamentous *fd*-virus particles electrostatically adsorbed to cationic freestanding lipid membranes were studied on the single particle level by means of optical wide-field fluorescence microscopy.

Supergiant unilamellar vesicles (SGUVs) with diameters larger than 100 μm represent a perfect model of a freestanding membrane. In this work, a method was developed that enabled the reliable and efficient electroformation of cationic SGUVs on ITO-coated coverslips. The utilization of SGUVs as model freestanding lipid bilayers allowed for determination of the previously unknown surface viscosity of DOPC/DOTAP membranes. In particular, the analysis of the translational diffusion coefficients of small (10, 20, 50 nm) membrane-attached anionic polystyrene beads has shown that the surface viscosity of DOPC/DOTAP membranes with $C_{\text{DOTAP}} = 1\text{--}7$ mol% is independent of the DOTAP concentration and equals $\eta = (5.9 \pm 0.2) \times 10^{-10}$ Pa s m.

The fluorescence video-microscopy investigation of single DNA molecules attached to cationic SGUVs revealed a previously unreported conformational transition of a membrane-bound DNA molecule from a 2D random coil, the original conformation in which DNA attaches to the membrane, to a compact globule. This membrane-mediated DNA condensation is favored at high cationic lipid concentrations in the membrane and long DNA contour lengths. The DNA compaction rate in the coil-globule transition is 124 ± 46 kbp/s, and the resulting DNA globule sizes were found to be 250–350 nm at DOPC membranes containing 1 mol% DOTAP and 130–200 nm for 7 mol% DOTAP, indicating a stronger compaction for higher charge densities in the membrane. Additional experiments with freestanding cationic membranes in the gel state and supported cationic lipid membranes with gel-fluid coexistence suggest that the DNA collapse on a freestanding fluid cationic membrane may be initiated by a local lipid segregation in the membrane and is accompanied by local membrane deformations, which eventually stabilize the compact DNA globule.

Furthermore, in this work single molecule studies of random-coil DNA molecules and filamentous *fd*-virus particles on a freestanding cationic lipid bilayer with a low charge density were carried out. The experiments revealed that these particles can be described as semiflexible chains in 2D. Taken together, DNA molecules and *fd*-virus particles cover a broad range of the ratio of contour length and persistence length from 0.4 to 82. The results of this work demonstrate that the mobility of such membrane-attached semiflexible particles is strongly affected by hydrodynamics in the lipid membrane and the surrounding bulk fluid, and can in essence be described using a hydrodynamics-based theory for a disk-shaped solid membrane inclusion with a characteristic size approximately equal to the radii of gyration of the particles.

Contents

Publications	iii
Abstract	v
Introduction	1
1. Basic Concepts	3
1.1. Lipid bilayer membranes	3
1.1.1. Phase transitions in lipid membranes	4
1.1.2. Lipid membrane elasticity	5
1.1.3. Lipid model membranes	6
1.2. Brownian motion	7
1.2.1. Principles of Brownian diffusion	8
1.2.2. Diffusion of cylindrical membrane inclusions	9
1.3. Semiflexible polymers and filaments	13
1.3.1. Theoretical description of single semiflexible biopolymers	13
1.3.2. Diffusion of polymers in a thin viscous film	15
1.3.3. DNA	18
1.3.4. <i>fd</i> -virus	19
2. Materials and Methods	21
2.1. Materials	21
2.2. Formation of lipid model membranes	24
2.2.1. Supported lipid bilayers	24
2.2.2. Electroformation of giant and supergiant unilamellar vesicles	26
2.3. Fluorescence microscopy	27
2.3.1. Fluorescent labeling	27

2.3.2.	Microscopy setup	29
2.3.3.	The point spread function and the lateral optical resolution limit	30
2.4.	Single particle tracking	33
2.4.1.	Tracking of particle positions	34
2.4.2.	Tracking rod-like filaments	36
2.4.3.	Gyration radius and orientation of extended particles	39
2.4.4.	Constructing particle trajectories	41
2.4.5.	Determination of translational diffusion coefficients	42
2.4.6.	Determination of rotational diffusion coefficients	47
2.4.7.	Anisotropy in the translational diffusion of extended particles	51
2.4.8.	Diffusion on curved surfaces of supergiant vesicles	53
3.	Cationic Supergiant Unilamellar Vesicles as an Experimental Model of Freestanding Lipid Membranes	57
3.1.	Efficient electroformation of cationic SGUVs	58
3.1.1.	Experimental details	58
3.1.2.	Aging effects of ITO coverslips with use	59
3.1.3.	Improved electroformation efficiency through mild annealing of the ITO coating	61
3.1.4.	Surface properties of ITO investigated by AFM	62
3.2.	Membrane surface viscosity determination	64
3.2.1.	Anionic polystyrene beads as probes of the membrane surface viscosity	64
3.2.2.	Viscosity of water	66
3.2.3.	Membrane surface viscosity of DOPC/DOTAP membranes	66
3.3.	Conclusion	67
4.	Behavior of DNA Macromolecules on Cationic Lipid Membranes: Effects of DNA–Membrane Interaction Strength and Membrane Properties	69
4.1.	DNA on fluid freestanding cationic membranes	69
4.1.1.	Experimental details	70
4.1.2.	DNA condensation on freestanding fluid cationic lipid bilayers	71
4.1.3.	Diffusion of DNA globules	76
4.1.4.	Implications of the coil–globule transition of membrane-bound DNA macromolecules for cell biology	79
4.2.	DNA on freestanding and supported cationic gel-phase membranes	80
4.2.1.	Experimental details	81
4.2.2.	Behavior of DNA molecules adsorbed to freestanding cationic gel-phase membranes	83

4.2.3. Conformational behavior of DNA molecules at the fluid–gel transition of SLBs	84
4.3. Conclusion	86
5. Brownian Motion and Conformational Dynamics of DNA and <i>fd</i>-Virus on Freestanding Membranes with Low Cationic Lipid Concentration	89
5.1. Experimental details	90
5.2. Conformation of membrane-adsorbed <i>fd</i> -virus particles and random-coil DNA molecules	91
5.2.1. Radius of gyration and persistence length of random-coil DNA molecules on a freestanding membrane	91
5.2.2. Radius of gyration and persistence length of membrane-adsorbed <i>fd</i> -virus particles	95
5.3. Brownian motion of membrane-bound semiflexible DNA molecules in the random coil conformation	97
5.4. Brownian motion of membrane-bound semiflexible <i>fd</i> -virus particles – Transition from semiflexible filament to stiff rod	99
5.5. Conclusion	105
A. Appendix	107
A.1. Simulation of image acquisition for diffusion of <i>fd</i> -virus particles	107
List of Abbreviations	111
Bibliography	113
Acknowledgements	127
Declaration	129

Introduction

As the basis of all living matter, the cell in its entity has been a puzzling and exciting research focus for both biologist and physicists. A pivotal aspect of understanding the underlying functionality of cells lies in the architectural structure that constitutes this highly complex machinery. On the one hand, cells possess a membrane that acts as a selective barrier by physically separating the cellular interior from the extracellular environment and enclosed compartments from the cytoplasm. On the other hand, microfilaments, intermediate filaments and microtubules form a scaffold, the cytoskeleton, which maintains the cell shape. Both membrane and cytoskeletal components can be transferred to and investigated in a soft matter physics context in general and a biophysical context in particular. One aspect of biophysics is to quantitatively investigate isolated systems, such as semiflexible polymers, filaments and membranes in order to assign properties and decipher mechanisms that also apply to the finely tuned and orchestrated working principles in an intact cell. In fact, many of the macromolecules and filaments naturally found in cells can be described as semiflexible filaments. This includes filaments constituting the cell cortex such as actin [1, 2, 3], as well as microtubules [3, 4], DNA [5] and other macromolecules.

For the better part of the last century, basic research focused primarily on the distinct properties of isolated semiflexible molecules, filaments and lipid membranes with little consideration of potential interactions with and dependencies of their respective natural environments. The scientific advancement and accessibility of single molecule techniques, especially fluorescence microscopy, reinforced this tendency. However, mutual influences of these components pose a fascinating problem as they provide substantiated insight into the mechanisms of interplay between (bio)macromolecules and cell membranes. In recent past, scientific approaches shifted towards the investigation of the aforementioned interactions by utilizing artificial model systems that mimic a natural environment without displaying the entire complexity of living cells [6, 7]. An artificial model system can be realized by the adsorption of semiflexible polyelectrolytes, for example DNA, to oppositely charged membranes. In 1999, Maier and Rädler [8, 9] pioneered the application of double-stranded DNA on a flat supported cationic

lipid membrane in order to extract the conformational dynamics and Brownian motion of a polymer in 2D. This was succeeded by studies of similar design but with different polymers and/or lipid membrane content [6]. However, all of these experiments were conducted with lipid membranes situated on a solid support, which alters the intrinsic properties of the membranes by reducing the lipid mobility [10] and inhibiting the ability to deform locally as a reaction to external perturbations. The obvious continuation on this matter would be the investigation of systems which ensure that both membrane and attached semiflexible filaments maintain their complete set of respective intrinsic properties. Surprisingly, very little was known about the conformational dynamics and Brownian motion of single semiflexible filaments in this context prior the present Work.

In order to address this subject, a reliable model system of a freestanding lipid membrane needs to be established. Chapter 3 of this Thesis introduces an efficient protocol for the electroformation of cationic supergiant unilamellar vesicles with diameters larger than 100 μm . These vesicles serve as a perfect experimental platform to investigate the conformational dynamics and Brownian motion of membrane-bound particles by means of fluorescence wide-field microscopy and single particle tracking. Subsequent Chapters report on the conformational dynamics and Brownian motion of semiflexible double-stranded DNA molecules and filamentous *fd*-virus particles, which are adsorbed to freestanding cationic lipid bilayers at different membrane-particle interaction strengths controlled by the charge density in the lipid membrane.

Basic Concepts

1.1. Lipid bilayer membranes

Lipid bilayer membranes are one of the most important structures of living organisms. As a physical barrier, they separate internal cellular structures from the surrounding environment and organize the cellular interior into compartments. Together with proteins and protein complexes, they allow for a selective permeability, e.g. by endocytosis and exocytosis, or are used to maintain gradients, such as the proton gradient that allows for the production of the biological energy storage unit ATP (adenosine triphosphate) in mitochondria and chloroplasts, just to name a few of the countless processes dependent on lipid membranes.

Lipid bilayers are built from two layers of amphiphilic lipid molecules. Each amphiphilic lipid molecule consists of a polar, and thus hydrophilic, head and non-polar, and thus hydrophobic, hydrocarbon chains. In general, the spontaneous self-assembly of a membrane structure is driven by the principle of maximum entropy. If the individual lipids are dissolved in an aqueous medium, the water molecules have to form an organized hydration shell around the non-polar hydrocarbon chains and therefore this system's entropy is reduced. As a consequence, lipid molecules (self)-assemble in such a fashion that only the polar heads are exposed to water, and entropy is gained in this case.

A lipid bilayer is formed if the average overall shape of the single lipid is close to that of a cylinder. Such a membrane has a typical thickness of about 4 nm [11], defined by the size of two lipid molecules, one sitting in the upper and the other in the lower leaflet of the bilayer. Normally, lipid bilayers which are surrounded by water will form closed vesicles to shield all hydrophobic parts. That is, if the energy needed to bend the membrane into the vesicle shape is less than the interaction energy between water and the exposed hydrophobic chains at the border of the membrane [12].

The mechanical properties of a lipid bilayer depend mainly on the type of the lipid head groups, the hydrophobic chain lengths and the number and position of double bonds in the chains. This section gives a brief overview on some lipid bilayer properties, such as the lipid phase transition and the membrane elasticity. In the last part lipid model membranes used in *in vitro* studies are discussed.

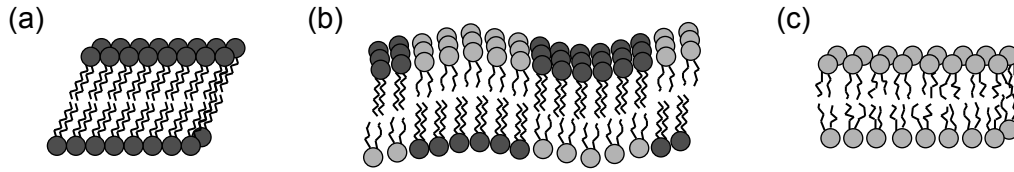


Figure 1.1: Schematic illustration of lipid membrane phases: (a) $L_{\beta'}$, (b) $P_{\beta'}$ and (c) L_{α} . (adapted from [13])

1.1.1. Phase transitions in lipid membranes

Lipids bilayers can undergo a phase transition between a solid-ordered or gel phase $L_{\beta'}$ and a liquid disordered or fluid phase L_{α} via a ripple phase $P_{\beta'}$. In the gel phase $L_{\beta'}$ all hydrocarbon chains are aligned and the head groups are highly ordered. When the temperature is raised the ripple phase $P_{\beta'}$ forms prior to melting and shows periodic one-dimensional ripples that might be caused by periodic arrangements of gel and fluid domains [13]. Above the melting temperature T_m the order in chains and of the head groups is lost and the membrane is in the fluid phase L_{α} . The different phases are sketched in Figure 1.1.

The melting temperature T_m depends strongly on the length and saturation of the hydrocarbon chains. Lipids with shorter chains have a lower T_m than lipids with longer chains and lipids with unsaturated chains have a significantly lower T_m than those with saturated chains due to higher disorder in the unsaturated chains that might assume a cis-conformation. For example, T_m is -20 °C for membranes formed from unsaturated DOPC (18:1 PC),¹ while for saturated DSPC (18:0 PC) $T_m = 54.7$ °C, and for a membrane consisting of lipids with shorter saturated chains like DMPC (14:0 PC) the melting temperature is only 23.6 °C [13].

If the lipid membrane consists of two – or more – lipids with different melting temperatures, gel and fluid phases may coexist in a certain temperature interval between the two T_m . In this case the gel phase domain will be enriched with the higher melting lipid and the fluid phase domain will be enriched with the lower melting lipid [13].

Naturally, the area a single lipid occupies in the membrane is smaller in the high ordered gel phase compared to the disordered fluid phase. For DMPC, an area per lipid of 47 Å² was measured at 10 °C in the gel phase [14]. This value increases to about 60 Å² at 30 °C, when the membrane is in the fluid phase [15].

Also the individual lipid mobility is different in both phases. Lipids in a highly ordered gel-phase membrane move only very slowly, with reported diffusion coefficients in the range of 10^{-3} – 10^{-8} μm²/s [16]. In a fluid-phase membrane the lipid mobility is much higher and lateral diffusion coefficients in the range between 1 and 10 μm²/s are observed [16]. For example, a diffusion coefficient of 6.3 μm²/s was found for a fluorescent lipid analogue probe in a DOPC vesicle at room temperature [17]. This drastic change in lipid mobility is also reflected in

¹An 18:1 hydrocarbon chain consists of 18 carbon atoms with 1 double bond.

the membrane viscosity felt by any object incorporated or associated with a membrane. The membrane viscosity grows exponentially when approaching the phase transition from the fluid to the gel phase [18].

1.1.2. Lipid membrane elasticity

A lipid bilayer membrane has elastic properties. From the three types of elastic deformations, shearing, stretching and bending, only two remain in a fluid membrane because in reaction to shearing forces the lipids react by flowing and rearranging [19]. The elastic reaction to stretching forces is limited to only small deformations, because already area changes by about one percent lead to rupture of the membrane [20]. The third elastic deformation, membrane bending, is dominating the overall appearance of lipid bilayers, for example the shape that vesicles assume.

The theoretical description of membrane bending originates from the works of Canham [21], Helfrich [22] and Evans [23] in the 1970s. The bending energy per unit area g_b at a certain membrane position is given by the Helfrich equation [22]

$$g_b = \frac{\kappa}{2}(C_x + C_y - C_0)^2, \quad (1.1)$$

with the principle radii of curvature C_x and C_y , the spontaneous curvature C_0 and the bending rigidity κ which is a measure of the softness of the lipid bilayer.

Since fluid lipid membranes are rather soft they undergo thermally induced fluctuations which, in part, can be visualized by optical microscopy. A quasi spherical vesicle with radius R that encloses a volume $V = (4\pi/3)R^3$ by a membrane with area $A = 4\pi R^2 + \Delta$ might show observable shape fluctuation if the excess area Δ is large enough and the vesicle is not additionally tensed, for example by a negative osmotic gradient between the enclosed medium and the surrounding medium. In Figure 1.2 two giant unilamellar DOPC vesicles are shown. While one seems perfectly spherical, the other shows large scale shape fluctuations,

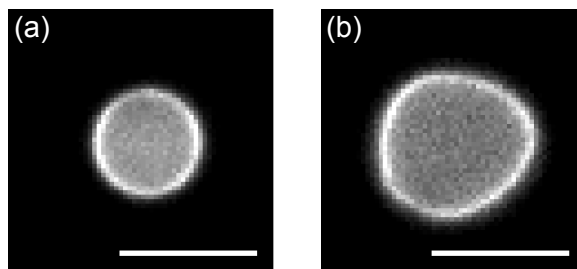


Figure 1.2: Fluorescent wide-field microscopy images of giant unilamellar DOPC vesicles. (a) Spherical vesicle that does not show noticeable shape fluctuations. (b) Distorted vesicle exhibiting strong shape fluctuations. Scale bar: 5 μm . Fluorescent membrane label: 0.1 mol% DiO .

resulting in significant distortions. The power spectral density of those shape fluctuations around the mean spherical shape are dependent on the bending rigidity and thus were used to determine κ [24, 25, 26, 27]. For DOPC vesicles κ was found to be about 2×10^{-20} J [25]. It is important to note that small scale fluctuations may be present on a membrane, even if large scale fluctuations are not detectable by optical microscopy.

1.1.3. Lipid model membranes

Lipid bilayers are a highly versatile system, as due to their self-assembly they can be easily used as a model for minimal biological systems [28] whose properties can be easily altered by the chosen lipid composition. Apart from a change of the pure mechanical properties, charged lipids, such as anionic phosphatidylserine (PS) or cationic trimethylammonium-propane (TAP) lipids, can be introduced to create an electrostatic potential that leads to attraction of oppositely charged biological molecules or colloidal particles to the membrane. With these possibilities lipid membranes are as important as fascinating object of interest in biology, biochemistry, biophysics and more general, soft matter physics.

Several different types of lipid model membranes exist. In this Section and this Thesis, the focus is on systems with single (unilamellar) lipid bilayers. In principle, three different membrane model systems exist for unilamellar bilayers which are sketched in Figure 1.3: *(i)* Unilamellar vesicles (see Figure 1.3(a)) which exist with a broad spectrum of sizes. Small unilamellar vesicles (SUVs) with diameters from 10 nm to 100 nm, large unilamellar vesicles (LUVs) with diameters from 100 nm to 1 μm and giant unilamellar vesicles (GUVs) with diameters from 1 μm to 100 μm . For diameters larger 100 μm the term supergiant unilamellar vesicles (SGUVs) is suggested in this Thesis. The lipid membrane of unilamellar vesicles is on both sides in contact with the aqueous solution and of course, bent to obtain the usually spherical vesicle shape. In contrast to this, *(ii)* the supported lipid bilayer (SLB) follows the curvature of a solid support and is therefore, in the simplest case, flat (see Figure 1.3(b)). A thin aqueous film between the lower leaflet of the bilayer and the solid support acts as a lubricant that allows for the lateral mobility of lipids in the membrane. *(iii)* Another possibility to form a flat but non-supported membrane, is the so called black lipid bilayer (BLB), spanned over a solid aperture as drawn in Figure 1.3(c).

All types of model membranes have advantages and disadvantages and the chosen system depends much on the specific scientific demands on the experiment. The flat membranes obtained from SLBs and BLBs can be easily imaged using fluorescence microscopy. Furthermore, the solid support of the SLB allows for atomic force microscopy (AFM) measurements.

The main disadvantages of the BLB is that it usually has a shorter long term stability compared to vesicles and SLBs, and in addition, the experimental preparation process demands the presence of hydrocarbon solvents. Traces of this solvent might be present in the readily

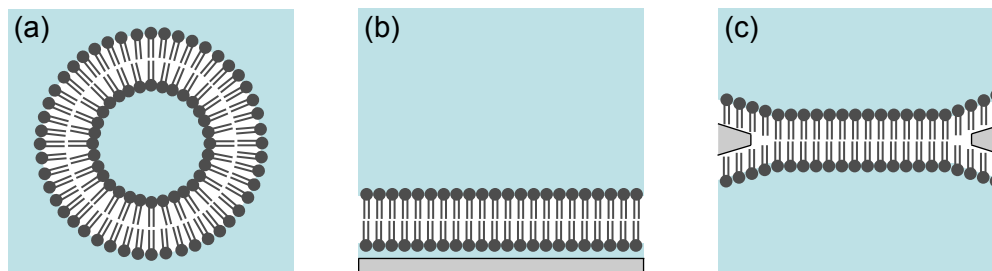


Figure 1.3: Schematic drawing of lipid model membrane systems. (a) Unilamellar vesicle. (b) Supported lipid bilayer. (c) Black lipid membrane.

assembled bilayer [29]. This can be circumvented, if only micrometer-sized apertures are used and GUVs are burst to form the bilayer over these holes [30], resulting in comparatively small, micrometer sized, freestanding membrane areas.

The membrane properties of the very stable SLBs, on the other hand, are quite strongly influenced by the solid support. The lipid mobility in a SLB can be strongly inhibited [10]. It was found that the diffusion coefficients of a membrane probe can be about five times smaller in an SLB compared to a freestanding membrane [31]. Furthermore, the lipid phase transition from gel to fluid phase is completely different, as the transition temperature region is broadened and shifted to a higher T_m [32, 33]. For a supported DMPC membrane for example, AFM reveals gel domains at a temperature as high as 30 °C [32]. These changes in the melting temperature were attributed in part to an independent melting of the two bilayer leaflets [33]. The solid support also changes the elastic behavior of the membrane resulting in virtually complete suppression of thermally induced fluctuations [34]. In addition, membrane defects as small as several nm are more than common, even in a SLB that seems homogeneous in fluorescent microscopy [32, 33, 35, 36]. If the area per lipid is changed, for example due to temperature changes, the bilayer reacts to this by formation or expansion of these defects [35].

Unilamellar vesicles are stable, solvent free and the membrane is undisturbed by influences of any support. However, only SGUVs have a membrane that can be considered flat on the scale of tens of micrometers and thus allow for the efficient application of single particle tracking in wide-field fluorescence microscopy (for details see Section 2.4.8). For these reasons, SGUVs are an intriguing model system for freestanding lipid membranes.

1.2. Brownian motion

The random motion of microscopic objects in a liquid at rest is named after Robert Brown who, in 1827, famously described the movement and rotation of pollen grains and smaller particles released from the pollen if immersed in water [37]. Brown carried out additional

studies to investigate the pollen of dead plants, pit-coal and a variety of minerals he was able to grind to a powder. Since all particles exhibited a similar behavior, he ruled out that the observed vivid particle motion was an active process of living matter. Brownian motion is caused by the frequent collisions of the particles with the surrounding molecules of the medium that move due to their thermal kinetic energy. In fluid media these collisions occur at a rate $k_{\text{coll}} = 10^{21} \text{ s}^{-1}$ [38] leading to a random particle motion without memory at observation rates $k_{\text{obs}} \ll k_{\text{coll}}$ for very small particles. However, this is not entirely true for observation rates $> 1 \text{ kHz}$. Because in general, memory effects are present due to the inertia of the viscous liquid medium in which the particles are immersed. But these memory effects vanish completely for observation rates $< 1 \text{ kHz}$ and particles $< 10 \text{ }\mu\text{m}$ in water [39]. Therefore, Brownian motion of these particles observed at millisecond time resolution constitutes a Markov process [40].

1.2.1. Principles of Brownian diffusion

The molecular interpretation of Brownian motion was proposed by Einstein in 1905 [41] and confirmed experimentally by Perrin only a few years later [42] providing indirect evidence for the existence of atoms and molecules. Quantitatively the stochastic process of Brownian motion is described by the diffusion equation or Fick's second law [40]

$$\frac{\partial \rho(\mathbf{r}, t)}{\partial t} = D \nabla^2 \rho(\mathbf{r}, t), \quad (1.2)$$

where D denotes the diffusion coefficient. The solution $\rho(\mathbf{r}, t)$ of Equation (1.2) is the conditional probability to find a Brownian particle at an interval $[\mathbf{r}, \mathbf{r} + d\mathbf{r}]$ at time t (with $t \gg k_{\text{coll}}^{-1}$), provided that at time $t = 0$ it was at the origin. With proper normalization $\int \rho(\mathbf{r}, t) d\mathbf{r} = 1$ the unique solution $\rho(\mathbf{r}, t)$ for n -dimensional diffusion in a uniform unbounded medium is:

$$\rho(\mathbf{r}, t) = \frac{1}{(4\pi Dt)^{\frac{n}{2}}} \exp\left(-\frac{\mathbf{r}^2}{4Dt}\right). \quad (1.3)$$

This is an n -dimensional Gaussian distribution with variance $\sigma^2 = 2nDt$. In every individual dimension Brownian motion is described by

$$\rho(x, t) = \frac{1}{\sqrt{4\pi Dt}} \exp\left(-\frac{x^2}{4Dt}\right). \quad (1.4)$$

With the known $\rho(\mathbf{r}, t)$ the mean squared displacement (MSD) of an ensemble of Brownian particles can be calculated, leading to the Einstein-Smoluchowski relation of a linear dependence between MSD and time [41, 43].

$$\langle \mathbf{r}^2 \rangle = \int \mathbf{r}^2 \rho(\mathbf{r}, t) d\mathbf{r} = 2nDt \quad (1.5)$$

In experimental works the fact that all n dimensions partition equally and independently to the diffusion process is often used to reduce the analysis to a lower dimensionality, circumventing the difficulties of three dimensional particle tracking.

Furthermore, because Brownian diffusion (also called normal diffusion) is a stationary ergodic process the ensemble average is equivalent to a time average over a single particle trajectory [44].

$$\langle \mathbf{r}^2 \rangle = \int |\mathbf{r}(t' + t) - \mathbf{r}(t')|^2 dt' \quad (1.6)$$

The diffusion coefficient D follows the Einstein relation [38, 41]

$$D = \frac{k_B T}{\zeta}, \quad (1.7)$$

with the thermal energy ² $k_B T$ and the friction coefficient ζ . In case of a spherical particle in a uniform 3D viscous medium the Stokes relation applies, giving $\zeta = 6\pi\mu a$ with hydrodynamic radius a and fluid bulk viscosity μ , resulting in

$$D = \frac{k_B T}{6\pi\mu a}. \quad (1.8)$$

By analogy to the translational Brownian diffusion, the rotational diffusion laws can be derived [45]. The rotational motion of an object about a single fixed axis is described by the angular MSD

$$\langle \theta^2 \rangle = \int |\theta(t' + t) - \theta(t')|^2 dt' = 2D_R t \quad (1.9)$$

and in case of a spherical particle in a uniform 3D viscous medium the rotational diffusion coefficient D_R is

$$D_R = \frac{k_B T}{\zeta_R} = \frac{k_B T}{8\pi\mu a^3}. \quad (1.10)$$

1.2.2. Diffusion of cylindrical membrane inclusions

While in the previous section the friction and thus the diffusion coefficient was determined for particles which are freely suspended in a bulk fluid, Brownian motion also occurs for particles embedded in quasi two-dimensional systems, as sketched in Figure 1.4. Diffusion processes of membrane proteins or lipid domains in a lipid membrane are typical examples for such systems, where a cylindrical inclusion with radius a is diffusing in a flat layer with surface viscosity ³ η , which is surrounded by bulk fluids with viscosities μ_1 and μ_2 . In such a two-dimensional system a consistent definition of the friction ζ is more difficult. Here, the translational mobility $1/\zeta$ is not well defined if the hydrodynamic Stokes equations are reduced

²With the Boltzmann constant $k_B = 1.3806 \times 10^{-23}$ J K⁻¹ and the absolute temperature T .

³The surface viscosity η of a thin layer of a homogeneous fluid is related to the bulk viscosity μ of the fluid constituting the layer through the thickness h of the layer by $\eta = \mu h$

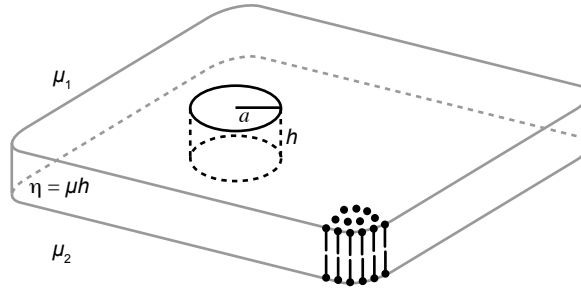


Figure 1.4: Sketch of a cylindrical object with radius a diffusing in a fluid membrane of height h and surface viscosity η surrounded by fluid media with bulk viscosities μ_1 and μ_2 .

to only the viscous response of the 2D fluid surrounding the inclusion [46]. This arises from the fact that for a steady, two-dimensional motion of a viscous, incompressible fluid around a cylinder at rest, the necessary boundary condition of zero velocity at the surface of the cylinder and constant velocity infinitely far away from the cylinder cannot be met simultaneously, the so-called Stokes' paradox [16].

Saffman and Delbrück (SD) were first to realize that diffusion in a membrane is essentially a 3D problem, where the motion of the inclusion leads to a momentum transfer to the bulk solvent above and below the membrane [47, 48]. To describe the influence of the bulk solvent a hydrodynamic length scale, the so-called Saffman-Delbrück length, is introduced

$$l_{\text{SD}} = \frac{\eta}{(\mu_1 + \mu_2)}. \quad (1.11)$$

This length represents the distance in the membrane beyond which the normally logarithmically dependent long-range fluid flows in the membrane caused by the motion of the inclusion can be neglected, because of a rapid decay due to the drag of the surrounding fluid [49]. Using l_{SD} , a reduced inclusion radius can be defined

$$\epsilon = a/l_{\text{SD}}. \quad (1.12)$$

The model that Saffman and Delbrück developed was meant to describe the mobility of membrane proteins whose radii are of order of a few nanometer, thus meeting the condition $\epsilon \ll 1$ given a typical SD length in the range of 250–2500 nm corresponding to membrane surface viscosities in the the range of 5×10^{-10} to 5×10^{-9} Pa s m [50] surrounded by water with the viscosity $\mu_{1,2} = 1 \times 10^{-3}$ Pa s. The friction coefficient for translational motion found

in the SD approximation [47, 48] is

$$\zeta_{\text{T}}^{\text{SD}} = \frac{4\pi\eta}{\ln(2/\epsilon) - \gamma}, \quad (1.13)$$

with the Euler constant $\gamma = 0.57721566490153\dots$. The friction coefficient for rotational motion in the same approximation is

$$\zeta_{\text{R}}^{\text{SD}} = 4\pi\eta a^2. \quad (1.14)$$

However, the Saffman-Delbrück model is only valid for membrane inclusions with sizes that are at the same time: (i) significantly larger than the size of an individual lipid molecule [51, 52], because of a breakdown of the hydrodynamic calculations for too small inclusion radii [51]; and (ii) significantly smaller than the reduced inclusion radius ϵ .

A more general hydrodynamic model for the diffusion of membrane inclusions of arbitrary radii and for arbitrary viscosities of the membrane and surrounding fluids was proposed by Hughes, Pailthorpe and White (HPW) [53]. Since the solutions given in [53] demand complicated numerical calculations before application to any measured data, for practical purposes Petrov and Schuille (PS) published a closed-form expression to closely approximate the HPW solutions [54, 55].

For translational diffusion of a membrane inclusion the friction coefficient is [54]

$$\zeta_{\text{T}}^{\text{HPW PS}} = \frac{4\pi\eta[1 - (\epsilon^3/\pi) \ln(2/\epsilon) + c_1\epsilon^{b_1}/(1 + c_2\epsilon^{b_2})]}{\ln(2/\epsilon) - \gamma + 4\epsilon/\pi - (\epsilon^2/2) \ln(2/\epsilon)}, \quad (1.15)$$

and thus the diffusion coefficient

$$D_{\text{T}}^{\text{HPW PS}} = \frac{k_{\text{B}}T}{4\pi\eta} \frac{\ln(2/\epsilon) - \gamma + 4\epsilon/\pi - (\epsilon^2/2) \ln(2/\epsilon)}{[1 - (\epsilon^3/\pi) \ln(2/\epsilon) + c_1\epsilon^{b_1}/(1 + c_2\epsilon^{b_2})]} \quad (1.16)$$

with

$$c_1 = 0.73761,$$

$$b_1 = 2.74819,$$

$$c_2 = 0.52119,$$

$$b_2 = 0.51465.$$

The expression for the rotational friction is derived in [55]

$$\zeta_{\text{R}}^{\text{HPW PS}} = \frac{4\pi\eta^3}{(\mu_1 + \mu_2)^2} [\epsilon^2 + 4\epsilon^3/(3\pi) + c_{\text{R1}}\epsilon^{b_{\text{R1}}}/(1 + c_{\text{R2}}\epsilon^{b_{\text{R2}}})], \quad (1.17)$$

and with that the diffusion coefficient

$$D_{\text{R}}^{\text{HPW PS}} = \frac{k_{\text{B}}T(\mu_1 + \mu_2)^2}{4\pi\eta^3} \frac{1}{\epsilon^2 + 4\epsilon^3/(3\pi) + c_{\text{R1}}\epsilon^{b_{\text{R1}}}/(1 + c_{\text{R2}}\epsilon^{b_{\text{R2}}})}, \quad (1.18)$$

where

$$\begin{aligned} c_{\text{R1}} &= 0.31943, \\ b_{\text{R1}} &= 2.91587, \\ c_{\text{R2}} &= 0.60737, \\ b_{\text{R2}} &= 0.68319. \end{aligned}$$

Expressions (1.16) and (1.18) have been successfully used to describe the translational and rotational diffusion of lipid membrane domains with radii of several micrometer [54, 55].

Asymptotic behavior

Expressions (1.16) and (1.18) describe the translational and rotational diffusion coefficients of membrane inclusions in dependence of the inclusion size and the viscosities of the membrane and the surrounding media.

For very small membrane inclusions, $\epsilon \ll 1$, the translational and rotational diffusion coefficients are dominated by the influence of the membrane surface viscosity and described by the SD approximation:

$$D_{\text{T}}^{\text{SD}} = \frac{k_{\text{B}}T}{4\pi\eta} (\ln(2/\epsilon) - \gamma), \quad (1.19)$$

$$D_{\text{R}}^{\text{SD}} = \frac{k_{\text{B}}T}{4\pi\eta a^2}. \quad (1.20)$$

Whereas in this case the translational diffusion coefficient has a weak logarithmic dependence on the viscosities of the surrounding media, the rotational diffusion coefficient is even independent of the surrounding bulk viscosities. Furthermore in this approximation the size dependence of both diffusion coefficients is weaker than for three-dimensional diffusion in a bulk medium. For the translational diffusion coefficient of a particle in a bulk medium one expects $D \sim a^{-1}$, and for the rotational diffusion coefficient $D_{\text{R}} \sim a^{-3}$. In case of a particle incorporated into a membrane for $\epsilon \ll 1$ one finds $D_{\text{T}}^{\text{SD}} \sim \ln a$ for translational diffusion and $D_{\text{R}}^{\text{SD}} \sim a^{-2}$ for rotational diffusion.

For very large membrane inclusions, $\epsilon \gg 1$, the translational and rotational diffusion coefficients are both independent of the membrane surface viscosity and dominated by the bulk viscosity of the surrounding media:

$$D_{\text{T}}^{\text{HPW large}} = \frac{k_{\text{B}}T}{8(\mu_1 + \mu_2)a}, \quad (1.21)$$

$$D_{\text{R}}^{\text{HPW large}} = \frac{3k_{\text{B}}T}{16(\mu_1 + \mu_2)a^3}. \quad (1.22)$$

The dependence on the inclusion size a in this approximation is similar to the free diffusion in a bulk.

1.3. Semiflexible polymers and filaments

Polymers are, by definition, molecules that are built from repetitive sequences of monomeric units. Many biological molecules match this definition and these biopolymers can be classified in three different categories: nucleic acids, proteins and polysaccharides. Importantly, the structural appearance of biomacromolecules is closely correlated with their biological function and controlled by the flexibility of the polymer, the interactions of the individual building blocks with each other and the interaction with the surrounding solvent medium [56]. The conformation of very large biopolymers such as DNA molecules, actin filaments or microtubules and their dynamics can be resolved and investigated by fluorescence microscopy.

In the first part of this Section the basic theoretical description of semiflexible linear biopolymers by the worm-like chain (WLC) model is introduced and theoretical models for diffusion of polymers in a membrane are discussed. In the last part of this Section, the general properties of semiflexible double-stranded DNA molecules and *fd*-virus particles are discussed.

1.3.1. Theoretical description of single semiflexible biopolymers

The worm-like chain (WLC) model first formulated by Kratky and Porod in 1949 [57] treats a single, isolated polymer chain as a continuous thin elastic filament that obeys Hooke's law under small deformations. In many cases, conformations, thermal shape fluctuations and the response to external forces of large linear biopolymers, such as actin [1, 2, 3, 58], microtubules [3, 4] and DNA [5, 59, 60, 61], are successfully described by the WLC model.

Figure 1.5 shows a sketch of a semiflexible filament. At two positions on the filament s and s' the unit tangent vector \mathbf{t} is displayed. The total bending energy E_b of such a filament of length L is [56]:

$$E_b = \int_0^L \frac{\kappa}{2} \left(\frac{\delta \mathbf{t}}{\delta s} \right)^2 ds, \quad (1.23)$$

with the characteristic bending rigidity κ . In three-dimensional space, the directional correlation function of the tangential vector decays exponentially,

$$\langle \mathbf{t}(s) \cdot \mathbf{t}(s') \rangle_{3\text{D}} = \exp \left(-\frac{|s' - s|}{l_p} \right). \quad (1.24)$$

Here, the persistence length l_p serves as a measure of the length scale at which the orientational correlation within the filament is lost and therefore it can be used as an indicator of the

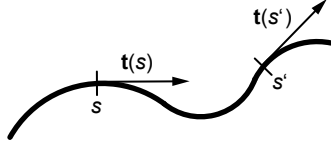


Figure 1.5: Sketch of a semiflexible filament with unit tangent vectors \mathbf{t} at filament positions s and s' .

filament flexibility. The relation between the bending rigidity and the persistence length is $l_p = \kappa/(k_B T)$ [56].

The characteristic size of a polymer can be characterized by the radius of gyration R_g , the square-root of the second moment of the mass distribution of the polymer filament. In the WLC model, the mean squared radius of gyration depends on the length of the filament and the persistence length [56]:

$$\langle R_g^2 \rangle = \frac{l_p}{3L^2} \left[L^3 - 3L^2 l_p + 6L l_p^2 - 6l_p^3 \left(1 - \exp\left(-\frac{L}{l_p}\right) \right) \right], \quad (1.25)$$

with the limiting forms

$$\langle R_g^2 \rangle = \frac{1}{12} L^2, \quad L \ll l_p \text{ (stiff rod)} \quad (1.26)$$

$$\langle R_g^2 \rangle = \frac{1}{3} L l_p, \quad L \gg l_p \text{ (Gaussian random coil)}. \quad (1.27)$$

The conformation of a polymer is also reflected by its end-to-end distance d_{ee} , and a closed form expression for the mean squared end-to-end distance exists in the WLC model [56],

$$\langle d_{ee}^2 \rangle = 2l_p^2 \left[\frac{L}{l_p} - 1 + \exp\left(-\frac{L}{l_p}\right) \right], \quad (1.28)$$

with the limiting forms

$$\langle d_{ee}^2 \rangle = L^2, \quad L \ll l_p \text{ (stiff rod)} \quad (1.29)$$

$$\langle d_{ee}^2 \rangle = 2L l_p, \quad L \gg l_p \text{ (Gaussian random coil)}. \quad (1.30)$$

All the equations above are valid in three-dimensional space. However, if the polymer is confined to a two-dimensional space, the directional correlation function of the tangential vector

$$\langle \mathbf{t}(s) \cdot \mathbf{t}(s') \rangle_{2D} = \exp\left(-\frac{|s' - s|}{2l_p}\right), \quad (1.31)$$

decays with twice the persistence length l_p of a filament in three-dimensional space [59]. Therefore, in Equations (1.25) and (1.28), l_p has to be replaced by $2l_p$ for the consistent use

of the persistence length $l_p = \kappa/(k_B T)$. With that, one obtains for the mean squared radius of gyration of a semiflexible polymer in 2D

$$\langle R_g^2 \rangle_{2D} = \frac{2l_p}{3L^2} \left[L^3 - 6L^2 l_p + 24Ll_p^2 - 48l_p^3 \left(1 - \exp\left(-\frac{L}{2l_p}\right) \right) \right], \quad (1.32)$$

with the limiting forms

$$\langle R_g^2 \rangle_{2D} = \frac{1}{12} L^2, \quad L \ll l_p \text{ (stiff rod)} \quad (1.33)$$

$$\langle R_g^2 \rangle_{2D} = \frac{2}{3} Ll_p, \quad L \gg l_p \text{ (Gaussian random coil)}, \quad (1.34)$$

and for the mean squared end-to-end distance in 2D,

$$\langle d_{ee}^2 \rangle_{2D} = 8l_p^2 \left[\frac{L}{2l_p} - 1 + \exp\left(-\frac{L}{2l_p}\right) \right], \quad (1.35)$$

with the limiting forms

$$\langle d_{ee}^2 \rangle_{2D} = L^2, \quad L \ll l_p \text{ (stiff rod)} \quad (1.36)$$

$$\langle d_{ee}^2 \rangle_{2D} = 4Ll_p, \quad L \gg l_p \text{ (Gaussian random coil)}. \quad (1.37)$$

1.3.2. Diffusion of polymers in a thin viscous film

For a polymer which is adsorbed to a freestanding fluid lipid membrane one can expect similarities in the dependence of the translational and rotational diffusion to the diffusion of cylindrical membrane inclusions described by the HPW hydrodynamic theory (see Section 1.2.2). The similarity should manifest mainly in the presence of a transition from membrane viscosity dominated diffusion for small polymer sizes compared to the hydrodynamic length scale $l_{SD} = \eta/(\mu_1 + \mu_2)$, to bulk viscosity dominated diffusion for large polymer sizes.

No theoretical treatment of the diffusion of semiflexible polymer on a membrane can be found in the literature. However, for both limiting cases, the very soft Gaussian chain random coil and the very stiff straight rod, theoretical predictions of translational and rotational diffusion coefficients exist.

Diffusion of a Gaussian chain polymer in a membrane

The diffusion of a Gaussian polymer chain of arbitrary size in a fluid membrane is described in the work of Ramachandran, Komura, Seki and Gompper [62] referred to as RKSG in the following. They use the radius of gyration of the polymer as the characteristic inclusion size.

For the translational diffusion of a Gaussian polymer of arbitrary R_g the diffusion coefficient

is [62]

$$D_{\text{T}}^{\text{RKSG}} = \frac{k_{\text{BT}}}{4\pi\eta} \frac{1}{\epsilon^4} \left[(\pi \operatorname{erfi}(\epsilon) - \operatorname{Ei}(\epsilon^2)) \exp(-\epsilon^2) + \frac{4\sqrt{\pi}}{3} \epsilon^3 + \epsilon^2 - (\ln \epsilon^2 + \gamma)(\epsilon^2 - 1) - 2\sqrt{\pi}\epsilon \right], \quad (1.38)$$

with the reduced inclusion size $\epsilon = R_{\text{g}}/l_{\text{SD}}$ and Euler's constant γ . It is important that γ is used up to 14th digit at least because otherwise the computation for small ϵ is inaccurate and unstable. The function $\operatorname{erfi}(x)$ is the imaginary error function and $\operatorname{Ei}(x)$ is the exponential integral.

Furthermore, in [62] the relaxation times of a polymer in a membrane are given. As the longest relaxation time is equivalent to the rotational relaxation time τ_{R} , the rotational diffusion coefficient $D_{\text{R}} = 1/(2\tau_{\text{R}})$ can be calculated and is

$$D_{\text{R}}^{\text{RKSG}} = \frac{k_{\text{BT}}}{(32/\pi)\eta R_{\text{g}}^2} \frac{[\pi^2 - \sqrt{2}\pi^{3/2}\epsilon + 2 \ln(\pi/\epsilon^2)\epsilon^2 + \sqrt{2\pi}\epsilon^3]}{(\pi^2 + \epsilon^4)}. \quad (1.39)$$

Diffusion of a stiff straight rod in a membrane

In the limit of a stiff straight rod of length L , translational and rotational diffusion in a membrane are described by a model by Levine, Liverpool and MacKintosh (LLM) [63, 64]. Independently at the same time, a theory giving similar results was developed by Fischer [65, 66]. Both theories assume filaments with high aspect ratios of filament length to filament diameter and calculate the viscous drag coefficients and drag forces, respectively. They treat the lateral diffusion of the filament differently than the HPW and RKSG theory. Instead of the mean two-dimensional diffusion coefficient D_{T} , the diffusion parallel (D_{\parallel}) and perpendicular (D_{\perp}) to the filament's long axis orientation are investigated, where $D_{\text{T}} = (D_{\parallel} + D_{\perp})/2$. This is meaningful and necessary due to anisotropy in hydrodynamic drag experienced by a strongly anisotropic object such as a rod-like filament with high aspect ratio. With an increasing length L of the rod the anisotropy in the viscous drag is found to become larger resulting in progressively more different values of the diffusion coefficients D_{\parallel} and D_{\perp} [63, 64, 65].

In the LLM and Fischer theories the filament length L is used as the characteristic inclusion size. For both theories no closed-form expression for the description of the diffusion coefficients of filaments of arbitrary lengths are available. However, the asymptotic behavior for very large and very short rods compared to the hydrodynamic length scale are reported, and are summarized in Table 1.1.

Table 1.1.: Overview of asymptotic behavior of diffusion coefficients for small and large polymers in a fluid membrane (surface viscosity η) surrounded by bulk media (viscosities μ_1, μ_2) according to RKSG theory (Gaussian chain) and LLM and Fischer theories (both for straight rod) and comparison to the HPW theory for a cylindrical disk.

	asymptotic behavior of small and large inclusions		effective radius a (cylindrical disk, HPW)	
	$\epsilon \ll 1$ *	$\epsilon \gg 1$ *	$\epsilon \ll 1$ *	$\epsilon \gg 1$ *
HPW [53] (cylindrical disk of radius a)				
D_T	$\frac{k_B T}{4\pi\eta} \left(\ln \frac{2l_{SD}}{a} - \gamma \right)$	$\frac{k_B T}{8(\mu_1 + \mu_2)a}$	—	—
D_R	$\frac{k_B T}{4\pi\eta a^2}$	$\frac{k_B T}{(16/3)(\mu_1 + \mu_2)a^3}$	—	—
RKSG [62] (flexible Gaussian chain with radius of gyration R_g)				
D_T	$\frac{k_B T}{4\pi\eta} \left(\ln \frac{l_{SD}}{R_g} - \frac{\gamma}{2} + \frac{3}{4} \right)$	$\frac{k_B T}{3\sqrt{\pi}(\mu_1 + \mu_2)R_g}$	$a \approx 0.71R_g$	$a \approx 0.66R_g$
D_R	$\frac{k_B T}{(32/\pi)\eta R_g^2}$	$\frac{k_B T}{(32/\sqrt{2\pi^3})(\mu_1 + \mu_2)R_g^3}$	$a \approx 0.9R_g$	$a \approx 0.91R_g$
LLM [63, 64] (stiff straight rod of length L)				
D_\perp	stated to scale similar to HPW; converges to same values as D_\parallel	$\frac{k_B T}{\pi(\mu_1 + \mu_2)L}$	—	$a \approx 0.39L$ $\approx 1.36R_g^\dagger$
D_\parallel	stated to scale similar to HPW; converges to same values as D_\perp	$\frac{k_B T}{\pi(\mu_1 + \mu_2)L} \ln \left(0.43 \frac{L}{l_{SD}} \right)$	—	different scaling
D_R	$\frac{k_B T}{1.48\eta L^2}$	$\frac{k_B T}{0.25(\mu_1 + \mu_2)L^3}$	$a \approx 0.34L$ $\approx 1.19R_g^\dagger$	$a \approx 0.36L$ $\approx 1.25R_g^\dagger$
Fischer [65, 66] (stiff straight rod of length L)				
D_\perp	$\frac{k_B T}{4\pi\eta} \left(\ln \frac{8l_{SD}}{L} - \gamma - 1/2 \right)$	$\frac{k_B T}{\pi(\mu_1 + \mu_2)L}$	$a \approx 0.41L$ $\approx 1.43R_g^\dagger$	$a \approx 0.39L$ $\approx 1.36R_g^\dagger$
D_\parallel	$\frac{k_B T}{4\pi\eta} \left(\ln \frac{8l_{SD}}{L} - \gamma + 1/2 \right)$	$\frac{k_B T}{\pi(\mu_1 + \mu_2)L} \ln \left(0.48 \frac{L}{l_{SD}} \right)$	$a \approx 0.15L$ $\approx 0.53R_g^\dagger$	different scaling
D_R	$\frac{k_B T}{(\pi/2)\eta L^2} \ddagger$	$\frac{k_B T}{(\pi/12)(\mu_1 + \mu_2)L^3}$	$a \approx 0.35L$ $\approx 1.22R_g^\dagger$	$a \approx 0.37L$ $\approx 1.27R_g^\dagger$
* $\epsilon = a/l_{SD}$ for HPW; $\epsilon = R_g/l_{SD}$ for RKSG; $\epsilon = L/l_{SD}$ for LLM and Fischer				
† rod length L related to the radius of gyration R_g according to Equation (1.33)				
‡ assuming a missprint in [66], otherwise $D_R = (k_B T)/((\pi/4)\eta L^2)$ and $a \approx 0.25L \approx 0.87R_g$ for $\epsilon \ll 1$				

Comparison of the asymptotic expressions for diffusion coefficients of a Gaussian chain polymer and a stiff straight rod in a membrane with the asymptotic expressions for diffusion coefficients of a cylindrical membrane inclusion

In order to compare the RKSG, LLM and Fischer theories with the HPW theory, the asymptotic behavior of the diffusion coefficients in case of very small ($\epsilon \ll 1$) and very large reduced

characteristic size ($\epsilon \gg 1$) are summarized in Table 1.1. If the scaling is similar to the HPW theory the effective inclusion radius a of a respective cylindrical disk is provided.

Interestingly, all asymptotic expressions of RKSG, LLM and Fischer scale similar to the asymptotic behavior expected for a cylindrical membrane inclusion according to HPW [53], with the sole difference in scaling found for the translational diffusion coefficients parallel to a very long stiff straight rod in the LLM and Fischer theory.

Judging from the asymptotic expressions, the rotational diffusion coefficients of a flexible Gaussian chain in a viscous membrane according to RKSG can be described by the HPW model for a cylindrical membrane inclusion with a radius a that is only 10 % smaller than the radius of gyration of the polymer chain. The rotational diffusion of a stiff straight rod according to LLM and Fischer, on the other hand, can as well be described by the HPW model for a cylindrical membrane inclusion with a radius a which in this case is about 20 % larger than the radius of gyration of the rod-like filament.

For the translational diffusion similar arguments can be made. The translational diffusion coefficients of a flexible Gaussian chain according to RKSG can be described by the HPW model for a cylindrical membrane inclusion with a radius a that is about 30–40 % smaller than the radius of gyration of the polymer chain. And the translational diffusion coefficients for diffusion perpendicular to a stiff straight rod according to LLM and Fischer, can be described by the HPW model for a cylindrical membrane inclusion with a radius a which is about 40 % larger than the radius of gyration of the rod-like filament.

1.3.3. DNA

Deoxyribonucleic acid (DNA) is responsible for the storage of the biological information, and the double helix structure of a double-stranded DNA (dsDNA) molecule is probably the most recognizable structure of all biomolecules. A single strand of the DNA molecule is built from sequences of the four different bases, or nucleotides, adenine (A), thymine (T), guanine (G) and cytosine (C) linked via a sugar-phosphate backbone. The second strand of a dsDNA inversely matches the other in a way that the base pairs A-T and G-C are formed, which link the two strands by two and three hydrogen bonds per base pair, respectively. Under physiological conditions, the dsDNA molecule assumes the so called B-form (native form), a double helix structure in which adjacent base pairs are separated by 3.4 Å (see Figure 1.6). A rotation of 36 ° between consecutive base pairs leads to a repetition of the helical structure after 10.5 bp. The diameter of a dsDNA molecule is about 20 Å [67].

Since they are storing the genetic code, organisms rely on an accurate reproduction of DNA molecules. As a consequence, the DNA of an organism has a very specific length. In bacteria cells, circular plasmid DNA exists in addition to the DNA packed in the chromosome. These DNA molecules of usually several kbp length can be easily produced and purified for *in vitro*

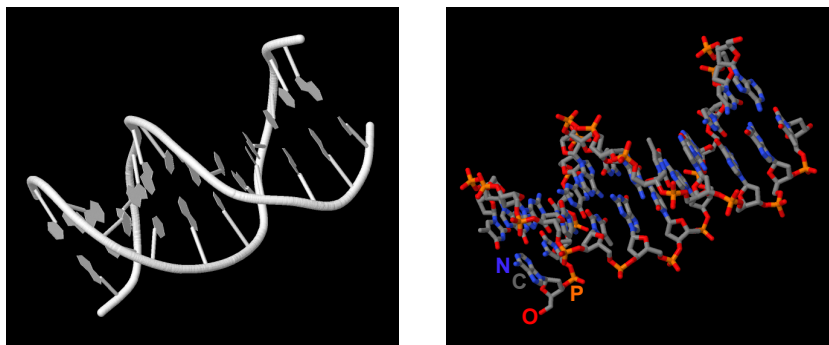


Figure 1.6: Double helical structure of DNA (B-form). Images were created using Jmol and the structure data of DNA [68] available at [69]

investigations. Shorter DNA fragments of defined length can be obtained using restriction enzymes that cut the DNA at a specific target motif. Therefore, DNA is an experimentally highly versatile molecule to probe its very own physical properties and its interaction with other components, such as a lipid membrane, at different length scales.

The phosphate groups along the DNA backbone have a low pKa value of about 1. This means that at pH 7 all phosphate groups are deprotonated and therefore, negatively charged [67]. The resulting charge of a dsDNA molecule is $2 e^-$ per bp or $5.9 e^-$ per nm.

Since DNA is a strong polyelectrolyte, its persistence length is dependent on the ionic strength of the surrounding medium, as the presence of counterions screens electrostatic repulsion forces. The overall persistence length l_p is a sum of the intrinsic persistence length $l_{p,0}$ and the electrostatic persistence length $l_{p,e}$ [70, 71],

$$l_p = l_{p,0} + l_{p,e}. \quad (1.40)$$

If the ionic strength is decreased, the electrostatic interactions stiffen the DNA molecule, and the electrostatic persistence length $l_{p,e}$ grows. At physiological buffer conditions the DNA persistence length of $l_p \approx 50$ nm was measured by multiple techniques [72, 73]. Single molecule imaging of very long T4-DNA (165.6 kbp) revealed that the persistence length can increase up to $1.7 \mu\text{m}$ at a salt concentration of 10^{-6} M [74].

1.3.4. *fd*-virus

The *fd*-virus is a filamentous bacteriophage that infects *Escherichia coli* (*E. coli*) bacteria. It is one of the simplest organisms possible, as it consists only of a filamentous protein shell enclosing a circular single stranded DNA of 6408 nucleotides [75] that encodes five different types of shell proteins. The major part of the coating is built from about 2800 units of one small protein and only at the ends, five of each of the other proteins form the caps [76].

As the length of the DNA determines the length of the individual *fd*-virus [77], the virus

length distribution is highly monodisperse [78]. A *wild type fd*-virus has a length $L_0 = 880$ nm and a diameter of only 6.6 nm [75].

The outer surface of the protein shell is strongly negatively charged and exhibits a line charge density along the filament of about $10 e^-$ per nm at pH 7.4 [79].

When grown in some *E. coli* host strains the *fd*-virus tends to form purely linear multimeric structures, resulting in rod like filaments of multiple length of a single virus. This is especially the case for *E. coli* strains that possess the DNA repair protein recA^+ [77]. If multimers are formed, the length distribution of viruses is very polydisperse. However, the individual *fd*-virus length is not random, as multimers, called $[fd]_m$, have a length m -times that of the monomer, where m is an integer number. This means that the degree of multimerization of an individual virus filament can be easily determined by fluorescence imaging microscopy and virus multimers can be sorted and analyzed with knowledge of their exact size. Multimers with m as large as 10 are not uncommon.

Due to the protein shell of the virus filament, the persistence length is much larger than that of a dsDNA molecule. Light scattering experiments revealed the most commonly used value of $l_p = 2.2 \mu\text{m}$ [76]. More recently, $l_p = 2.8 \pm 0.7 \mu\text{m}$ was found using a filament shape fluctuation analysis, that made use of long multimeric viruses observed by fluorescence microscopy [80]. As the persistence length is larger than the length of monomers or dimers of the *fd*-virus, these particles are very stiff and almost rod-like, whereas longer multimers are more flexible and show thermally induced shape fluctuations.

Materials and Methods

2.1. Materials

This section gives an overview of all materials used in the experiments conducted for this thesis.

Lipids

All lipids were purchased in chloroform solution from Avanti Polar Lipids (USA). Structures of zwitterionic phospholipids DOPC (1,2-dioleoyl-sn-glycero-3-phosphocholine) and DMPC (1,2-dimyristoyl-sn-glycero-3-phosphocholine), as well as cationic lipids DOTAP (1,2-dioleoyl-3-trimethylammonium-propane), and DMTAP (1,2-dimyristoyl-3-trimethylammonium-propane) are shown in Figure 2.1. In addition for some experiments the anionic lipid DOPS (1,2-dioleoyl-sn-glycero-3-phospho-L-serine) and the cationic lipid EDOPC (1,2-dioleoyl-sn-glycero-3-ethylphosphocholine) were used.

The membranes formed by the unsaturated acyl chain lipids DOPC and DOTAP are in the fluid state for all molar mixtures of the two at room temperature (24 °C). Membranes from mixtures of lipids with saturated acyl chains DMPC and DMTAP can be in the gel state at this temperature depending on the molar fraction of DMTAP. While the fluid–gel transition temperature T_m of pure DMPC is about 24.5 °C it increases to $T_m = 26.8$ °C when 9 mol.% DMTAP are added and up to a maximum $T_m = 37.1$ °C for 43 mol.% of DMTAP [81].

DNA

Linearized double-stranded λ -phage plasmid DNA of 48.502 kbp and double stranded DNA fragments of 20 kbp, 10 kbp and 5 kbp were purchased from Fermentas (Germany).

fd-virus

A sample of Alexa-488 labeled *wild type fd*-virus was supplied by Dr. M. Paul Lettinga (Forschungszentrum Jülich, Germany). Viruses were grown in a JM101 host *E.Coli* strain and stored in 20 mM phosphate buffer at pH 7.5.

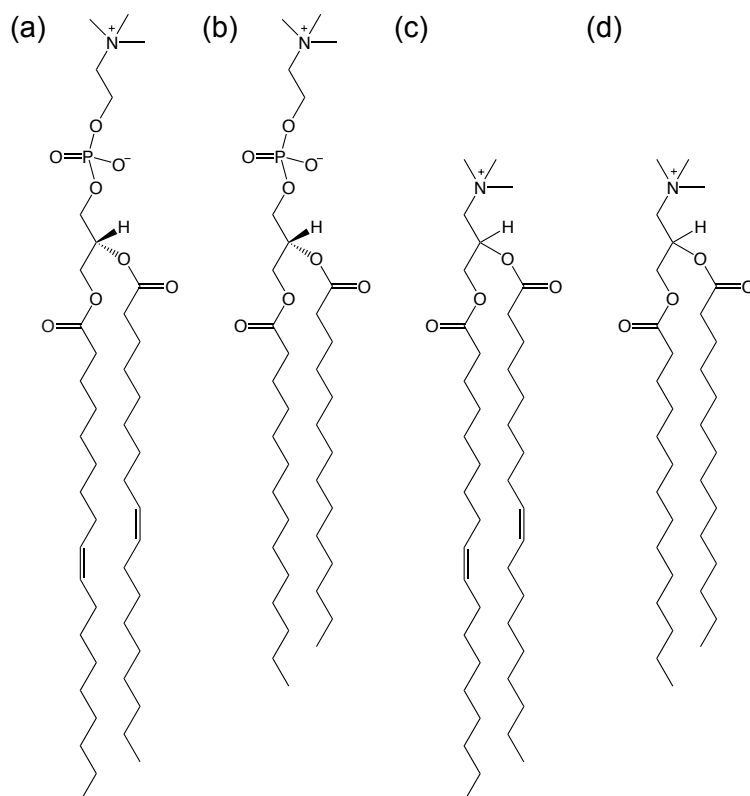


Figure 2.1: Structure formulas of zwitterionic phospholipids DOPC (a), DMPC (b) and of cationic lipids DOTAP (c) and DMTAP (d).

Water and buffer

Experiments were carried out in deionized, ELGA purified water, dd-H₂O. Before use, water was degassed to remove carbon dioxide and oxygen in order to gain a pH value of about 7 and decrease photo-oxidation of the fluorescent dyes. Following the degassing under vacuum in a desiccator, the volume above the water within the vessel was filled with nitrogen. The water was transferred into the sample chamber immediately thereafter.

For atomic force microscopy experiments 1x PBS (137 mM NaCl, 2.7 mM KCl, 10 mM Na₂HPO₄ and 2 mM KH₂PO₄) was used.

Fluorescent beads

Yellow-green fluorescent, carboxylate-modified polystyrene beads (FluoSpheres) were ordered from Invitrogen (Germany). These negatively charged beads with diameters of 20 nm, 40 nm and 100 nm were ultra-centrifuged at 100,000 g for 30 minutes, the supernatant was removed, and the beads were resuspended in dd-H₂O and diluted up to 10⁶ times before use.

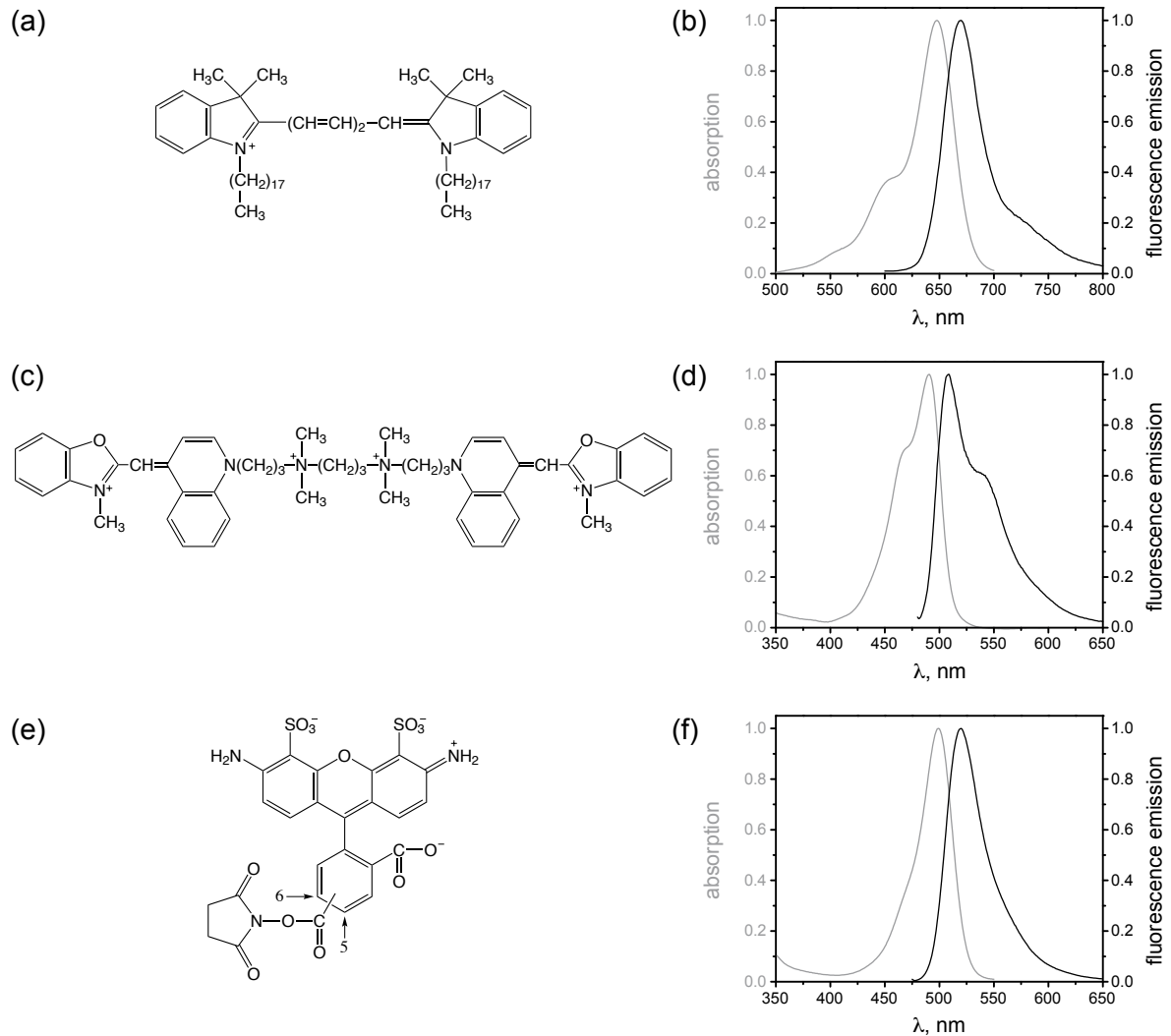


Figure 2.2: Structure formulas and spectra of absorption (grey) and fluorescence emission (black) of the fluorescent labels DiD (a, b), YOYO-1 (c, d), and Alexa-488 succinimidyl ester (e, f) as available by the producer.

Fluorescent dyes and labels

Lipid membranes were labeled with the red fluorescent membrane label DiD (1,1'-dioctadecyl-3,3,3',3'-tetramethylindodicarbocyanine; Sigma, Germany; see Figure 2.2(a,b)). The intercalating green fluorescent YOYO-1 (Invitrogen, Germany; see Figure 2.2(c,d)) was used to label DNA. Alexa-488 succinimidyl ester (Invitrogen, Germany; see Figure 2.2(e,f)) was used to fluorescently label *fd*-virus particles.

ITO-coated coverslips

Glass coverslips, #1.5, from Mentzel Gläser (Germany) with a diameter of 25 mm were coated with a 100 nm thick indium-tin oxide (ITO) layer ($\text{In}_2\text{O}_3 : \text{SnO}_2$, 90 : 10) by reactive magnetron sputtering at GeSim (Grosserkmannsdorf, Germany).

2.2. Formation of lipid model membranes

The interaction of negatively charged DNA macromolecules, *fd*-virus particles, and polystyrene beads with lipid membranes was studied using synthetic cationic lipid model membranes prepared according to standard protocols. The formation of mica supported lipid bilayers (SLBs) and electroformed giant unilamellar vesicles (GUVs) are described in this section.

2.2.1. Supported lipid bilayers

For all SLB experiments the same chamber design as shown in Figure 2.3 is used. A thin sheet of freshly cleaved mica is glued to a plasma-cleaned glass coverslip by a thin film of 518 F immersion oil (Zeiss, Germany). A cylindrical plastic ring is attached with NOA 88 UV-glue (Norland, NJ, USA) on top of the mica sheet creating the sample chamber. Since mica easily cleaves along its [001] planes, the substrate surface is very smooth and well suited to support the lipid membrane. The membrane is very close to the substrate but lubricated in a thin film of water between the lower leaflet of the lipid bilayer and the support, allowing for motion of the lipids in the membrane.

A flat lipid membrane formed on a flat substrate can be obtained in different ways which will be described in what follows.

Supported lipid bilayers from liposomes

SLBs can be deposited on the substrate by bursting and fusing small unilamellar vesicles (SUVs) [82]. SUVs are produced by first drying the desired lipid mixture dissolved in chloroform under a stream of nitrogen in a 1.5 ml glass vial for 10 min and desiccating in vacuum for 1 h. The resulting lipid film on the bottom of the glass vial is rehydrated in 10 mM Hepes buffer (pH 7.0) for 1 h at a temperature above the highest gel-fluid transition temperature T_m of the involved lipids. Afterwards, the sample is vortexed for three minutes to produce a suspension of multilamellar vesicles (lipid concentration: 10 mg/ml) which can be stored at $-20\text{ }^\circ\text{C}$ for several weeks. The multilamellar vesicle solution is diluted to a final lipid concentration of 0.7 mg/ml and placed in a bath sonicator at $T > T_m$, where shear forces destroy the multilamellar vesicles and create SUVs.

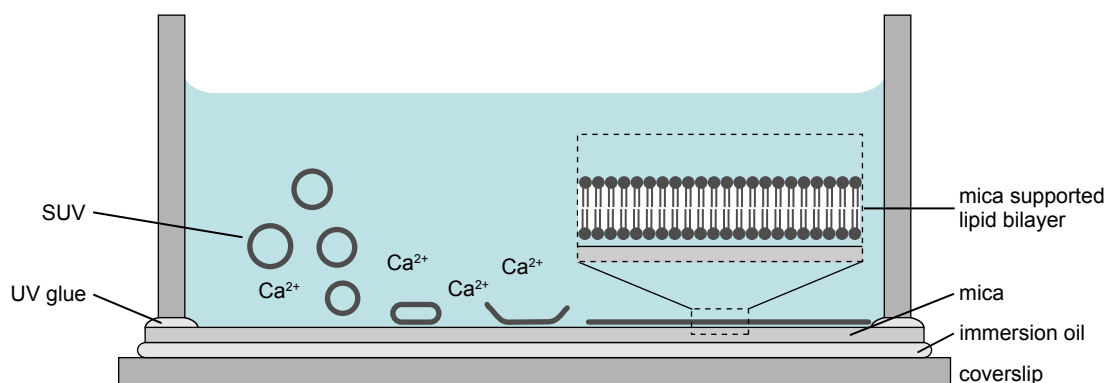


Figure 2.3: Formation of a mica supported lipid bilayer from SUVs. To create the sample chamber with the supporting mica substrate, a thin freshly cleaved sheet of mica is attached to the coverslip using a thin film of immersion oil. A plastic cylinder is glued on top of the mica with a UV-glue, sealing the chamber that is afterwards filled with the SUV solution containing Ca^{2+} ions to facilitate SUV fusion, bursting, and SLB formation.

The SUV solution is filled into the sample chamber and incubated for 10 min ($T > T_m$) with 3 mM CaCl_2 added. SUVs attach to the mica support, burst, and fuse to form a continuous single SLB with the help of the Ca^{2+} ions [83], as depicted in Figure 2.3. To remove excess SUVs, the sample chamber is repeatedly washed (no less than 10 times) with buffer ($T > T_m$). During the final step the washing buffer can be replaced by deionized water. It is important to make sure that the SLB stays covered with the aqueous medium at all times and is never allowed to dry.

Supported lipid bilayers by spin coating

Alternatively, another method to create cationic SLBs was used, leading to a very homogeneous membrane without artifacts, such as remaining holes or SUVs attached to the surface, as observed by fluorescence microscopy. To this end, the protocol [84] describing the rehydration of a lipid film deposited by spin coating and initially intended to form multiple SLBs was slightly altered to obtain a single supported membrane.

Lipid mixtures in chloroform are dried under a stream of nitrogen and dissolved in hexane/methanol (97:3 v/v) with a lipid concentration of about 7 mg/ml. A droplet of 30 μl of this solution is placed on the mica surface and spun at 3000 rpm for 40 s on a spincoater. After overnight desiccation under vacuum the lipid film is rehydrated in deionized water at $T > T_m$ for 1 h and subsequently gently washed several times. Using deionized water or 10 mM HEPES buffer without additional salt prevents formation of bilayer stacks but instead results in a single homogeneous lipid bilayer on the mica support.

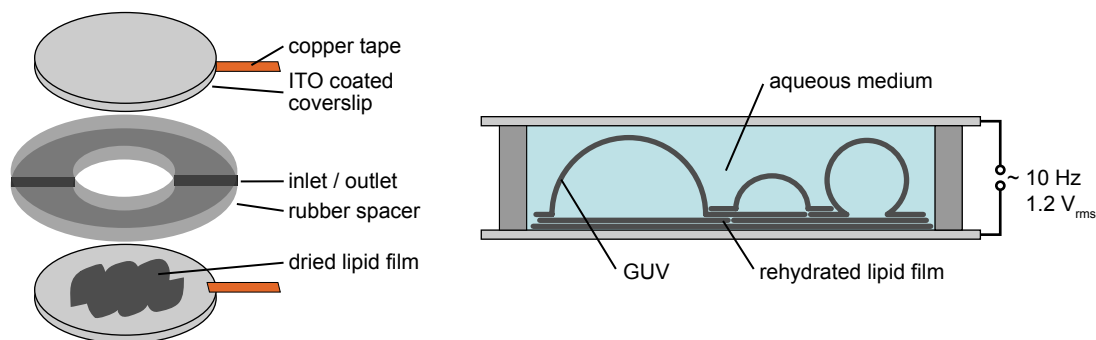


Figure 2.4: Electroformation of GUVs and SGUVs using ITO-coated coverslip electrodes. The lipid mixture in chloroform is spread in a snake like pattern on the lower of the two ITO-coated coverslips and dried under vacuum. The left-hand side shows the assembly of the electroformation chamber simultaneously serving as observation chamber. It is built from two ITO-coated coverslips with their ITO-coated surfaces facing each other, separated by a silicon rubber spacer of 3 mm height that has inlet and outlet openings to fill the chamber and exchange the medium after vesicle formation. A copper tape strip is attached with conductive glue to each ITO coverslip providing contacts for the function generator. A sinusoidal ac electric field of 10 Hz and 1.2 V_{rms} is applied, facilitating GUV and SGUV formation from the hydrated lipid film in low salt aqueous medium (right-hand side).

2.2.2. Electroformation of giant and supergiant unilamellar vesicles

Giant and supergiant unilamellar vesicles (GUVs and SGUVs) were grown using the electroformation technique developed by Angelova and co-workers. A lipid film is spread and dried on electrodes made of platinum wire [85, 86] or ITO coating on glass coverslips [87]. Rehydrating the lipids in a low salt aqueous medium and applying an electric field facilitates swelling of the lipid film and formation of giant vesicles with a single lipid bilayer membrane. The quality of the resulting vesicles strongly depends on the properties of the spread lipid film and the lipids used [11, 85, 88]. If the deposited lipid film contains too many stacked bilayers ($\gtrsim 50$), GUVs with 1 μm to 10 μm diameter are formed. Fewer layers in the lipid film (5 to 30) lead to creation of larger SGUVs (100 μm diameter and more) sitting in a dome shape on the electrode [85, 88].

Electroformation based on ITO coated coverslip electrodes first proposed in [87] was chosen for all (S)GUV experiments, the advantage of the ITO coverslips being the large and planar growth area and their transparency to visible light, which allows for further experiments in the same chamber without removing the (S)GUVs from the electrodes.

For the purpose of mimicking a freestanding bilayer, SGUVs with diameters $>100 \mu\text{m}$ are desirable. At this size the membrane at the upper pole region of the vesicle has a very low curvature at a lateral extension of 10 to 20 μm , thus enabling tracking and conformation analysis for single macromolecule and particles. Additionally, SGUVs should be sparse enough to allow interaction of the added particles of interest with a particular SGUV's membrane but without interference of other close by vesicles. The following preparation procedure yields

sparse vesicle densities with normally 5 to 10 SGUVs per mm^2 electrode area.

First, a lipid solution in chloroform with a total lipid concentration of 10 mg/ml is prepared. Then, 0.7 μl of this lipid solution is spread in a snake-like pattern without overlap on a $1.5 \times 1.5 \text{ cm}^2$ area, using a 5 μl Hamilton syringe. At this concentration a lipid film of approximately 10 bilayer thickness is formed, assuming an area per lipid of 0.72 nm^2 [15]. After drying the deposited lipid film on the ITO glass for 30 min in vacuum, the electroformation chamber is assembled as depicted in Figure 2.4. The ITO-coated surfaces of the coverslips face each other and are separated by a 3 mm thick silicon rubber ring that has inlet and outlet openings but otherwise seals the chamber. Copper tape contacts (SPI, USA) are conductively attached to the ITO-coated surfaces allowing for a connection to a voltage source. The assembled vesicle formation chamber is slowly filled with 300 μl of deionized water, and afterwards a sinusoidal ac electric field of 10 Hz and $1.2 V_{\text{rms}}$ is applied for 120 min. Electroformation is carried out at a temperature above the highest gel–fluid transition temperature T_m of the involved lipids.

Using the inlet and outlet openings of the rubber spacer, the medium surrounding the SGUVs can be exchanged after vesicle electroformation, and the particles of interest – the ones whose interaction with the membrane is to be studied – can be flushed in at a controlled rate using a syringe pump. Low flow rates of 5 to 10 $\mu\text{l}/\text{min}$ are advisable in order to protect the relatively fragile SGUVs bound to the coverslip surface from strong shear forces created by the flow.

2.3. Fluorescence microscopy

2.3.1. Fluorescent labeling

To visualize the interaction of the lipid membrane and polyelectrolytes or colloids adsorbed to its surface by means of fluorescence microscopy, the individual components are labeled with the fluorescent dyes shown in Figure 2.2. The dyes were chosen such that the red fluorescence of the membrane is well distinguishable from the green fluorescence of the polyelectrolytes or colloids. They can be separately detected with the use of appropriate emission filters allowing for only minimal bleed-through of the fluorescence signal to the other channel when simultaneously imaged.

Lipid membrane

A small fraction of 0.1 mol% of the red fluorescent lipid analogue dye DiD was added to the chloroform dissolved lipid mixtures before formation of the lipid model membranes. This fluorescent dye was shown not to alter the mechanical membrane properties if less than 2 mol% were added [89]. Note that DiD has a single positive charge located at the head group as seen in Figure 2.2(a).

DNA

DNA molecules were labeled with the green fluorescent intercalating dye YOYO-1. The fluorescence quantum yield of this marker is about 1000-fold higher when it intercalates into DNA than in free aqueous solution [90], and therefore the unbound probe creates only little background fluorescence. A labeling density of 0.2 dye/bp was chosen. At this labeling ratio close to the saturation value of about 0.25 dye/bp [91, 92], a homogeneous distribution of the dye molecules over all DNA molecules in the sample is ensured. At lower dye/bp ratios, the staining might induce long-lived inhomogeneous labeling distributions of the DNA molecules caused by the high affinity of the dye to the DNA [91]. While the DNA persistence length is not affected by the labeling [92] at a ratio of 0.2 dye/bp, it was shown that due to binding of the YOYO-1 the DNA contour length grows by about 30 % [92]. This means the known nominal length of DNA fragments can be converted into a contour length using a distance of 0.442 nm/bp .

In order to prevent inter-chain linking between different DNA molecules by the bisintercalating YOYO-1, the dye is added only to a dilute DNA solution of about $3 \text{ ng}/\mu\text{l}$. In detail, $9 \mu\text{l}$ of $10 \mu\text{M}$ YOYO-1 in dd-H₂O are added to $91 \mu\text{l}$ of DNA (base pair concentration: $5 \mu\text{M}$) in 10 mM HEPES buffer, pH 7.0. The sample incubated for no less than one hour at room temperature after gentle mixing by repeated pipetting of the staining solution.

fd-virus

The viruses were supplied already labeled with the green fluorescent Alexa-488 succinimidyl ester (Figure 2.2(e,f)). The staining had been performed according to a procedure described in [93] resulting in homogeneously labeled viruses with about 300 Alexa-488 dye molecules per unit virus length.

Photobleaching

Fluorescent dyes in the excited state are vulnerable to reactions with molecular oxygen. These reactions can destroy the fluorophore and permanently render the molecule to be non-fluorescent – the phenomenon known as photobleaching. Moreover, not only the dye molecule might be destroyed. It is known that the DNA intercalating dye YOYO-1 can cause photo-induced DNA double strand breaking (photocleavage) due to the generation of hydroxyl radicals [94].

In order to prevent photobleaching and photocleavage, degassed water with a reduced concentration of dissolved oxygen was used in all experiments. Furthermore, the exciting laser power density was kept low, usually at values of only a few hundred mW/cm^2 , and never exceeding $5 \text{ W}/\text{cm}^2$. The possibility to employ chemical agents that reduce photobleaching and

-cleavage was not explored, to minimize the number of unknown interactions of the ingredients in the sample.

2.3.2. Microscopy setup

The epifluorescence setup is built around a commercial Zeiss Axiovert 200 inverted microscope body and schematically sketched in Figure 2.5. The optical path for the fluorescence excitation uses the 488 nm and 647 nm lines of an Innova 70C Spectrum Ar/Kr ion gas laser (Coherent, Germany) operated in the multi-line mode. The laser lines are coupled into a single-mode optical fiber, after which a telescope is installed to expand the beam diameter. Using two mirrors, one of which is placed on a horizontally adjustable micrometer table, the beam is coupled into the back port of the microscope via a lens which focusses the laser beam reflected off a dichroic mirror onto the back-focal spot of the objective. As a result, a parallel beam leaves the objective propagating along the optical axis and illuminating the sample in the wide-field mode. In this configuration fluorescent structures in the sample located at distances of up to 0.6 mm above the coverslip can be explored. An LD C-Apochromat (40x, 1.1 numerical aperture (NA), water immersion) long-distance objective (Zeiss) was used for experiments with GUVs.

Alternatively, the micrometer table can be used to shift the focussed laser beam laterally away from the focal spot of the objective within the back-focal plane, thereby creating an angle at which the parallel beam exits the objective. If the lateral distance to the focal spot and thus the exiting angle is large enough, total internal reflection of the laser beam at the interface of the coverslip and the sample medium can be achieved. In this case only fluorophores within a distance of about 100 nm above the coverslip are efficiently excited by the evanescent field of the reflected laser beam. Total internal fluorescence microscopy (TIRF) was therefore applied to image DNA molecules on a supported lipid bilayer. This provided high signal to noise ratios of the resulting image due to the reduction of background fluorescence. In TIRF experiments an α Plan Apochromat (100x, 1.46 NA, oil immersion) objective (Zeiss) was used.

In the emission pathway, fluorescence is collected by the same objective, and after passing through the dichroic mirror, leaves the microscope at a side port. After that, it enters a W-View beamsplitter (Hamamatsu, Germany), where the green and red channel are divided and detected by an iXon 3 DU 897 electron multiplying charge coupled device (EMCCD) camera (Andor, Ireland). The separation of the two channels in the beamsplitter is realized by a 560 nm short-pass dichroic mirror reflecting the red and transmitting the green fluorescence. After passing through the HQ 525/50 and HQ 700/75 emission bandpass filters in the respective green and red pathways, both signals are rejoined laterally next to each other on the chip of the camera, using a set of mirrors and a 560 nm long-pass dichroic mirror. The pixel resolution of the resulting image is 389 nm/pixel using the 40x objective and 158 nm/pixel for

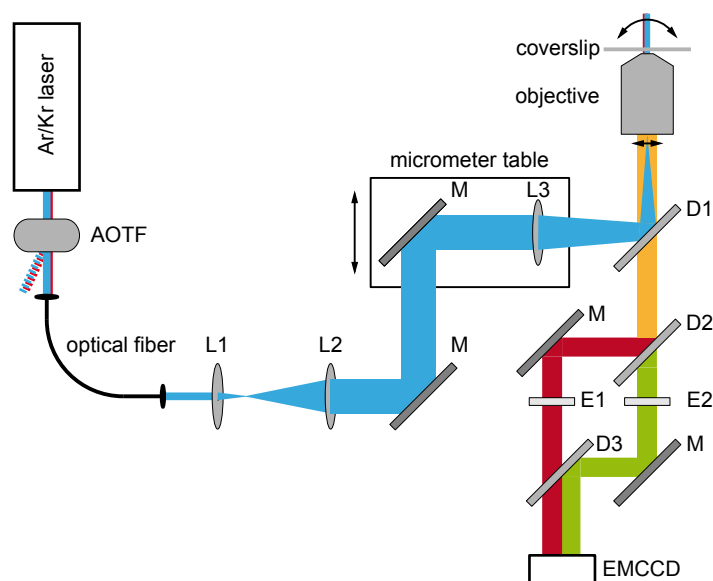


Figure 2.5: Schematic sketch of the epifluorescence microscopy setup. An Ar/Kr ion gas laser provides the 488 nm and 647 nm laser lines selected by an AOTF and coupled into a single mode optical fiber. After the fiber lenses L1 and L2 expand the beam diameter. Finally the laser is coupled into the microscope using a mirror M and lens L3 mounted on a micrometer table. Lens L3 focuses the beam to the back focal plane of the objective after being reflected off the excitation dichroic mirror D1. By lateral displacement of the micrometer table the focussed beam can be moved within the back focal plane of the objective, creating angles of the exiting laser large enough to allow TIRF microscopy due to total internal reflection of the beam at the coverslip–sample medium interface. The collected fluorescence emission passes D1 and is spectrally separated by the emission dichroic mirror D2. After passing through bandpass emission filters E1 or E2 the dichroic mirror D3 facilitates the spatial separation of the two spectral channels on the chip of the EMCCD camera that is used to acquire the fluorescence images.

the 100x objective. To obtain a higher pixel resolution for experiments with *fd*-virus on GUVs, an additional lens was placed in the emission pathway, leading to 75 nm/pixel when the 40x objective was deployed. The camera controls an acousto-optic tunable filter (AOTF) in the excitation laser pathway, blocking the fluorescence excitation when no image is acquired and thereby reducing unnecessary photobleaching of the fluorophores. Furthermore, the AOTF is used to select the laser lines illuminating the sample.

2.3.3. The point spread function and the lateral optical resolution limit

Point spread function of a fluorescent dipole image by a fluorescence microscope

The point spread function (PSF) describes the diffraction intensity pattern recorded at an area detector – such as a CCD camera chip – in the image space that originates from a single point-like source in the object space, imaged by an optical system. It is rotationally symmetric in the image plane and called the Airy pattern if the optical system has a circular aperture. In

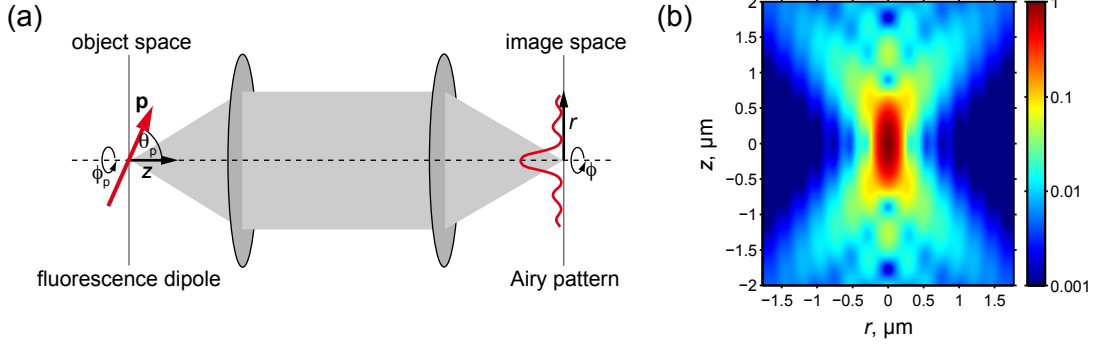


Figure 2.6: PSF of a microscope for a fluorescent dipole. (a) Schematic of a fluorescent dipole \mathbf{p} with orientation $\phi_{\mathbf{p}}$, $\theta_{\mathbf{p}}$ in the object space imaged by a lens, creating an Airy pattern on the detector in the image space. (b) Normalized PSF of a fluorescent dipole averaged over all dipole orientations with homogeneous circular polarized wide field excitation, imaged by an objective with NA = 1.1 and water immersion refractive index $n = 1.33$. The Intensity pattern along the image space coordinate r is rotational symmetric in the image plane for every axial distance z of the dipole from the objective focal plane in the object space. The intensity values are color coded using a logarithmic scaling.

fluorescence microscopy the point source is constituted by an emission dipole of a fluorescent dye molecule. Figure 2.6(a) sketches a fluorescent dipole \mathbf{p} imaged by an ideal lens. The intensity distribution of the emitted fluorescence recorded at the image plane along an angle ϕ can be calculated as a function of the dipole orientation $\phi_{\mathbf{p}}$, $\theta_{\mathbf{p}}$ in object space [95]:

$$I = [|I_0|^2 + |I_2|^2 + 2\Re\{I_0 I_2^*\} \cos(2(\phi_{\mathbf{p}} - \phi))] \sin^2 \theta_{\mathbf{p}} + 4|I_1|^2 \cos^2 \theta_{\mathbf{p}}, \quad (2.1)$$

where I_0 , I_1 and I_2 are the integrals

$$\begin{aligned} I_0 &= \int_0^\alpha \cos^{1/2} \theta \sin \theta (1 + \cos \theta) J_0 \left(\frac{v \sin \theta}{\sin \alpha} \right) \exp \left(i2u \frac{\sin^2 \frac{\theta}{2}}{\sin^2 \alpha} \right) d\theta \\ I_1 &= \int_0^\alpha \cos^{1/2} \theta \sin^2 \theta J_1 \left(\frac{v \sin \theta}{\sin \alpha} \right) \exp \left(i2u \frac{\sin^2 \frac{\theta}{2}}{\sin^2 \alpha} \right) d\theta \\ I_2 &= \int_0^\alpha \cos^{1/2} \theta \sin \theta (1 - \cos \theta) J_2 \left(\frac{v \sin \theta}{\sin \alpha} \right) \exp \left(i2u \frac{\sin^2 \frac{\theta}{2}}{\sin^2 \alpha} \right) d\theta. \end{aligned} \quad (2.2)$$

J_l are Bessel functions of the first kind of order l . Here the normalized optical coordinates u and v are used:

$$u = \frac{2\pi n \sin^2 \alpha}{\lambda} z \qquad v = \frac{2\pi n \sin \alpha}{\lambda} r \quad (2.3)$$

with the semi-aperture α , the refractive index of the immersion fluid n , the wavelength of light in vacuum λ , the axial distance z of the dipole position from the focal plane in object space, and the lateral distance $r = \sqrt{x^2 + y^2}$ from the origin in the image plane. The numerical

aperture NA of the objective is calculated as $\text{NA} = n \sin \alpha$.

Assuming fast free rotation of the dipole and a much longer image acquisition times compared to the fluorescence lifetime, averaging over all dipole orientations is justified and allows to calculate the detected intensity distribution in the image plane [95]:

$$I_{av} = \int_0^\pi \int_0^{2\pi} I \sin \theta_{\mathbf{p}} d\phi_{\mathbf{p}} d\theta_{\mathbf{p}} = \frac{8\pi}{3} (|I_0|^2 + 2|I_1|^2 + |I_2|^2). \quad (2.4)$$

The total PSF of the system is determined by detection PSF and excitation PSF:

$$\text{PSF}_{\text{sys}} = \text{PSF}_{\text{exc}} \cdot \text{PSF}_{\text{det}}. \quad (2.5)$$

In case of ideal wide-field microscopy and isotropic excitation PSF_{exc} is a constant, and therefore PSF_{det} , as defined in Equation (2.4), determines the shape of PSF_{sys} .

The integrals of Equation (2.2) can be numerically solved taking advantage of the Hankel transform:

$$f_2(\nu) = 2\pi \int_0^\infty f_1(\rho) J_l(2\pi\nu\rho) \rho d\rho \quad (2.6)$$

$$f_1(\rho) = 2\pi \int_0^\infty f_2(\nu) J_l(2\pi\rho\nu) \nu d\nu, \quad (2.7)$$

where the substitution of $\rho = \frac{1}{2\pi} \frac{\sin \theta}{\sin \alpha}$ is used. An algorithm presented in [96] that allows for fast and stable numerical calculation of the Hankel transform was used to calculate the PSF of a fluorescent dipole with wavelength $\lambda = 520$ nm imaged by an ideal water immersion objective with $\text{NA} = 1.1$ and $n = 1.33$. The resulting normalized PSF is shown in Figure 2.6(b) with the logarithmic scaling of the intensities.

Lateral optical resolution limit

Due to the statistical nature of the fluorescence emission the image of several emitting dipoles is an incoherent linear superposition which can be described by the convolution of the PSF and the spatial distribution of the dipoles in the object space [97]. While the position of a single fluorescent particle can be determined very accurately by finding the center position of the PSF (see Section 2.4), the optical resolution limit is defined by the distance two fluorophores can have which still allows one to distinguish between the two of them.

The lateral optical resolution limit depends on the wavelength of the detected light and several definitions are common. According to Abbé, the limit is reached if two point sources are positioned at a distance of the full width at half maximum (FWHM) of the PSF and it can be approximated as $0.5\lambda/\text{NA}$ [98]. The resulting intensity profile is shown in Figure 2.7(a). Another definition of the resolution limit, being the distance that the first minimum of the PSF has to its central maximum, was introduced by Lord Rayleigh [99] and can be estimated

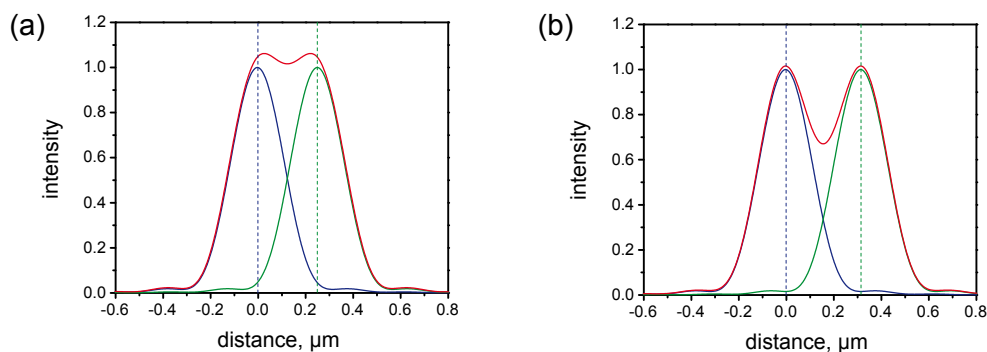


Figure 2.7: Resulting intensity of two - in focus - point sources at the lateral optical resolution limit. (a) Lateral optical resolution limit according to Abbé: intensity pattern (red) as a result of two point sources (blue and green) at a distance equal to the FWHM of the PSF. (b) Lateral optical resolution limit according to Rayleigh: resulting intensity pattern (red) if one point source (blue or green) is positioned at a distance of the first minimum in the PSF of the other.

by $0.61\lambda/\text{NA}$ (see Figure 2.7(b)).

The intensity distributions shown in Figure 2.7 are based on the assumption of an arbitrarily large number of photons emitted. In the reality of a single molecule experiment, the limited photon emission and detection, as well as noise, complicate the distinction of two particles. Sources of noise can be, for example, background fluorescence, scattered light, dark counts, and read out noise of the detector. It must be noted that by the use of modern deconvolution algorithms two or more particles especially with known and similar brightness can be resolved at much shorter distances than the above defined optical resolution. However, for simpler and faster particle tracking algorithms based on the initial identification of a local brightness maximum, the optical resolution limit is a good estimate.

2.4. Single particle tracking

The method of tracking single particle position found its first important application in the quantitative experimental analysis of Brownian motion carried out by Perrin in 1909 [42]. With the invention of digital CCD image sensors and their fast evolution in the late 20th century until the present day, single particle tracking became one of the standard methods used in the field of life sciences. Progressively more sensitive sensors allow for recording of positions and intensities of single fluorescent dye molecules. With this ability, the understanding of single molecule behavior and functionality progressed significantly over the past 25 years, due to the possibility to study the heterogeneity of individual molecules rather than the average ensemble behavior.

In the scope of this Thesis, single particle tracking is used to determine the mobility of particles as well as conformational behavior of micrometer-sized DNA molecules and *fd*-viruses

and its development with time.

On the way from the acquisition of a time series of fluorescent images to the determination of lateral and/or rotational diffusion coefficients that characterize the particle mobility, three main steps are necessary: *(i)* The high-accuracy determination of the particle positions and orientations in every image of the stack. *(ii)* Identification of particles in consecutive frames, thus retrieving their trajectories. *(iii)* Analysis of the statistics of the steps the particles made from frame to frame to obtain the diffusion coefficient.

In this Section a detailed description of the procedures used to determine diffusion coefficients of beads, DNA molecules and *fd*-viruses adsorbed to cationic lipid membranes is given. Analysis software scripts were written in MATLAB (MathWorks). In part they are based on the algorithms described by Grier, Crocker and Weeks [100] and implemented in MATLAB by Blair and Dufresne [101], to retrieve the trajectories (step *(ii)*), and for the particle position determination (step *(i)*).

2.4.1. Tracking of particle positions

In order to find sub-resolution sized particles, e.g. fluorescent beads, in an image, the first step is to apply a Gaussian kernel filter with a size of 3×3 pixels and standard deviation $\sigma = \sqrt{2}$ pixels, to remove pixel shot noise. Furthermore, a constant background is subtracted from the signal (see Figure 2.8(a) and (b)). Afterwards, positions of particles are defined to a pixel accuracy by finding local intensity maxima above a certain useful threshold in the image. Using these rough coordinates, a refined position determination in a region of interest (ROI) slightly larger than the particle size can be employed. In general, there are two possible ways to get the accurate particle position with a sub-pixel resolution.

In the centroid method, the particle position (x_0, y_0) is defined by the center of intensity (COI) and can be obtained by simple summation over the ROI:

$$\begin{aligned} x_0 &= \frac{1}{I_0} \sum_{x,y} xI(x,y) \\ y_0 &= \frac{1}{I_0} \sum_{x,y} yI(x,y) \end{aligned} \tag{2.8}$$

with

$$I_0 = \sum_{x,y} I(x,y). \tag{2.9}$$

This method is fast, but the accuracy is rather strongly affected by the residual noise [102].

Alternatively, the PSF can be approximated by a two-dimensional Gaussian, with the amplitude A and width B , and a nonlinear least-squares fit thereof to the intensity signal of the

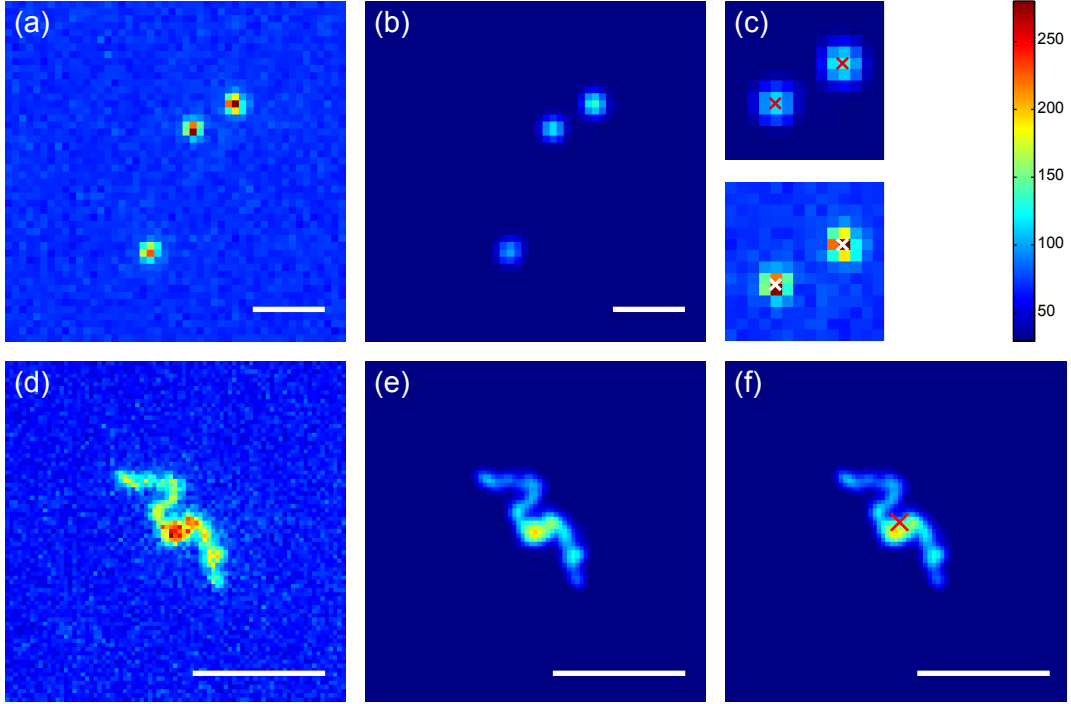


Figure 2.8: Tracking of polystyrene beads and DNA molecules adsorbed to lipid membranes using the centroid position determination method. (a) Original image of fluorescent beads with a 50 nm radius on a membrane. (b) Image (a) after filtering with a Gaussian kernel of 3×3 pixels size and $\sigma = \sqrt{2}$ pixels followed by background subtraction. (c) COI determined sub-pixel positions of the two beads in the upper half of (a) and (b), marked by red crosses in the filtered image (upper frame) and white crosses in the original image (lower frame). Similarly the COI method can be used to detect the position of extended objects. (d) Original image of λ -DNA on a membrane, (e) filtered image thereof. In (f) the COI determined position of the molecule is indicated by the red cross. Scale bars: 5 μm .

particle determines its center position.

$$I(x, y) = A \exp\left(-\frac{(x - x_0)^2 + (y - y_0)^2}{B^2}\right) \quad (2.10)$$

While this procedure is slower than the centroid method, it is less affected by the remaining photon noise [102]. It can yield an accuracy down to the nm level if the total number of detected photons originating from the particle is high, the pixel size of the detector is optimized with respect to the detected signal and the background noise, and the particle is immobilized [103, 104].

The choice of the method depends on the signal quality and the particle mobility in relation to the time resolution. The accuracy of position determination decreases due to the motion of the particle during the acquisition time of the image. As long as the centroid method yields an accuracy of the immobilized particle ξ in the range of $\sqrt{D\Delta t}$, with the diffusion coefficient D and the time between consecutive frames Δt , it is favored over the slower method of

Gaussian fitting. As discussed below (see Section 2.4.5), the inaccuracy of the particle position determination can be accounted for in the data analysis.

The centroid method also is very useful to determine the position of molecules with dimensions larger than the optical resolution. For example, an extended λ -DNA molecule on a supported lipid membrane occupies a space of several micrometers, but its local conformational details fall well below the optical resolution limit, which makes a full filament contour analysis impossible. In this case, the coarse-grained centroid method allows for accurate position tracking without the knowledge of the exact DNA contour, as shown in Figure 2.8(d-f).

2.4.2. Tracking rod-like filaments

Extended rod-like filaments which are virtually stiff at length scales of the optical resolution limit, like *fd*-virus filaments with a persistence length of about 2.2 μm , can be localized even more accurately than the much more flexible DNA molecules by a complete contour determination. Figure 2.9 illustrates the process of contour refinement and position determination of a *fd*-virus filament of 6 times the monomeric length, the $[fd]_6$ virus. The nominal contour length of such a filament is $6 \times 0.88 \mu\text{m} = 5.28 \mu\text{m}$.

The refined contour determination of *fd*-virus filaments is carried out in this work using an implementation of a filament refinement routine originally developed for actin and microtubule filaments [105]. The procedure consists of the following steps implemented in MATLAB:

(i) To find the rough position of a filament, the original image $I(x, y)$ (Figure 2.9(a)) has to be filtered to enhance the structures of interest and reduce the noise. First, the image $I(x, y)$ is filtered by convolving it with a Gaussian kernel of size w and a standard deviation of the Gaussian distribution $\sigma = \sqrt{2}$ pixels to obtain $I(x, y)_{\text{Gauss}}$. To reduce the background intensity, an average filtered image $I(x, y)_{\text{average}}$, where every pixel is the result of averaging over the surrounding $w \times w$ pixels in $I(x, y)$, is created and subtracted from $I(x, y)_{\text{Gauss}}$. The kernel size w is chosen much larger than the width across the filament. Typically the width of the filament in the original image is about 5 pixels, and a kernel size of $w = 21$ pixels is used to obtain $I(x, y)_{\text{rough}}$. The resulting image $I(x, y)_{\text{rough}} = I(x, y)_{\text{Gauss}} - I(x, y)_{\text{average}}$ is shown in Figure 2.9(b).

(ii) To obtain a mask of pixel positions belonging to the filament (Figure 2.9(c)) a proper thresholding has to be employed on $I(x, y)_{\text{rough}}$. The threshold value δ is determined by the average intensity $\langle I(x, y) \rangle$ and the standard deviation $\sigma_{I(x, y)}$ of the image $I(x, y)_{\text{rough}}$ using the relation $\delta = \langle I(x, y) \rangle + m\sigma_{I(x, y)}$, with an adjustable constant m , normally of about a value of 2. In addition, a minimum number of pixel positions in a connected area can be defined by eliminating small regions where residual noise might exceed δ .

(iii) Skeletonizing of the pixel position mask to a single line of one pixel thickness (Figure 2.9(d)) is performed with the use of the function `bwmorph` provided by the MATLAB image

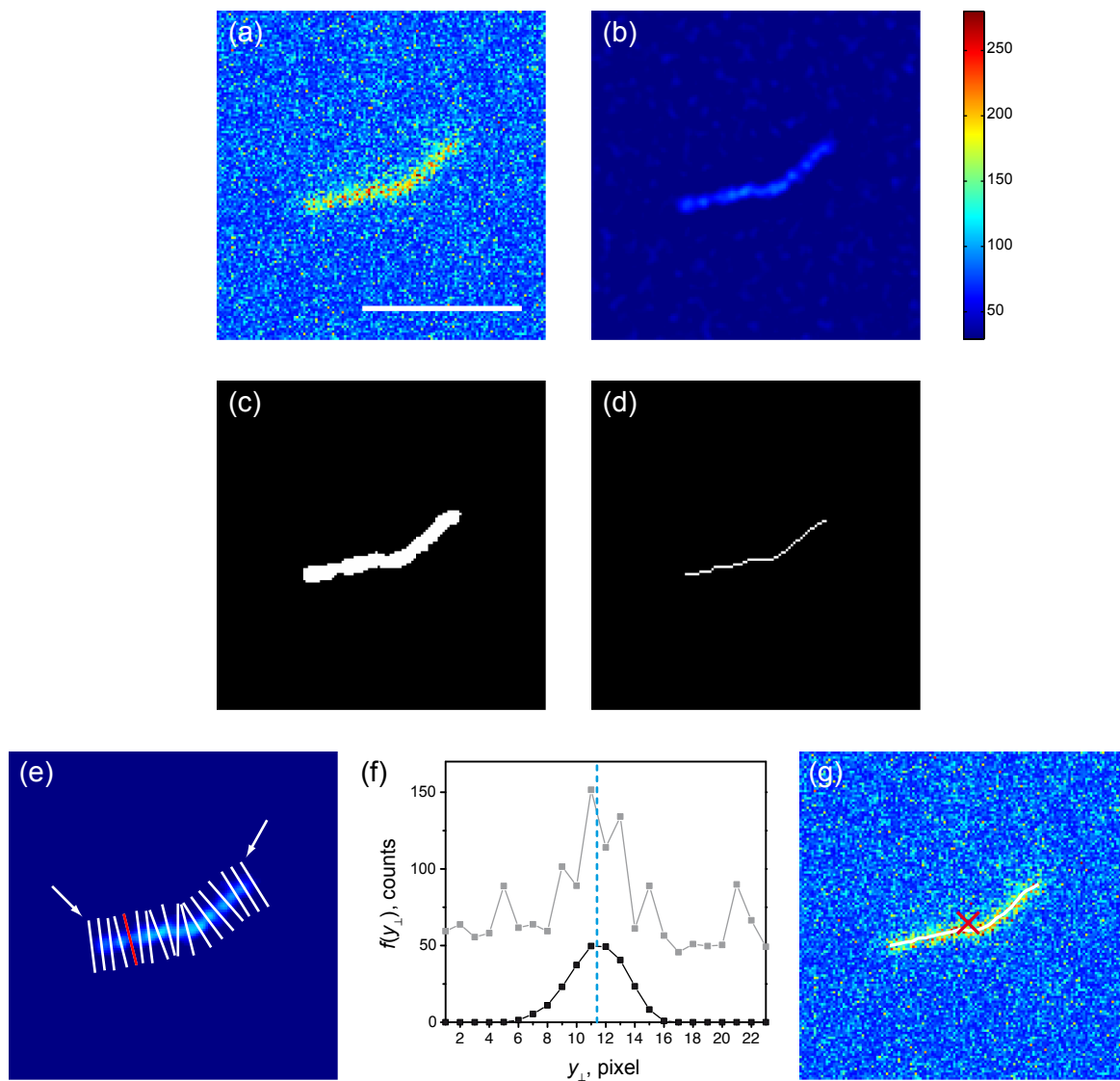


Figure 2.9: Contour and position determination of a rod-like *fd*-virus filament. (a) Fluorescence image of an $[fd]_6$ virus adsorbed to a lipid membrane. (b) Gaussian-filtered and background-reduced image of the virus filament (kernel size $w = 21$ pixels) for a rough filament position determination. (c) Mask of pixels belonging to the region where the filament is located. (d) Skeletonized mask indicating the rough position of the filament contour. (e) Gaussian-filtered background-reduced image of the virus filament ($w = 5$) for contour refinement. The white lines are drawn at every fourth pixel of the rough filament skeleton (d) perpendicular to the local filament orientation. The contour position is determined using the centroid method on the intensity distribution of image (e) along each line. (f) Intensity profile along the red line in (e) is shown in black and the respective intensity profile of in the non-filtered image (a) in gray. The COI position is indicated by the vertical dashed blue line. Profiles outside the filament range as stressed by the white arrows in (e) need to be removed by thresholding. (g) Original image overlaid with the refined equidistant contour (white line) and the center-of-mass particle position (red cross) calculated from this contour. Scale bar: $5 \mu\text{m}$.

processing toolbox. The retrieved skeleton defines the first rough set of xy position coordinates of the filament that needs further refinement.

(iv) To carry out a skeleton refinement, intensity distributions along the lines perpendicular to the local filament orientation at each position (x_i, y_i) need to be found. In [105] fitting the positions (x_i, y_i) to a polynomial is suggested, thereby allowing to obtain the polynomial's derivative and thus defining the local orientation $\Theta(x_i, y_i)$ at every skeleton position (x_i, y_i) . This approach fails if the filament is not stiff enough and two different values y can be found at the same x value. In these cases the local filament orientation can only be described in coordinates along the filament contour. The m positions (x_i, y_i) need to be continuous from $i = 1 \dots m$, with (x_1, y_1) as the starting and (x_m, y_m) as the ending position of the estimated filament contour. The two end positions have the unique characteristic that only one other position of all (x_i, y_i) is found as one of the eight neighboring pixels, whereas for all other positions along the filament two neighbors can be found. Arbitrarily, one of the two end positions is taken as the filament starting point and consecutively every position (x_{i+1}, y_{i+1}) has to be found as the one neighboring pixel remaining that was not already added to the filament contour. After all (x_i, y_i) are sorted, the local filament orientation can be calculated as $\Theta(x_i, y_i) = \arctan([y_{i+n} - y_{i-n}] / [x_{i+n} - x_{i-n}])$. Typically, $n = 2$ proved useful which leads to averaging the local filament orientation over a length of order of the optical resolution limit.¹ As a result, for a set of m positions (x_i, y_i) the orientation $\Theta(x_i, y_i)$ is only defined for $i = (n + 1), \dots, (m - n)$. Values for $\Theta(x_{1\dots n}, y_{1\dots n})$ are set to $\Theta(x_{n+1}, y_{n+1})$ and for $\Theta(x_{(m-n+1)\dots m}, y_{(m-n+1)\dots m})$ are set to $\Theta(x_{m-n}, y_{m-n})$. Furthermore, to compensate for pixels lost at the filament ends in the skeletonization process, six pixel positions are added to each end using the respective orientations. The new set of positions shall be referred to as (x_k, y_k) and includes all (x_i, y_i) .

(v) With all $\Theta(x_k, y_k)$ determined, another Gaussian-filtered and background-reduced version $I(x, y)_{\text{fine}}$ of the original image is calculated to carry out the refined contour determination. This time a smaller kernel size of $w = 5$ pixels, close to the width of the filament in the original image, is used. Figure 2.9(e) shows $I(x, y)_{\text{fine}}$ overlaid with white lines drawn perpendicular to the local filament orientation at every fourth pixel position along the filament. For every (x_k, y_k) the ROI $[x_k - \beta : x_k + \beta, y_k - \beta : y_k + \beta]$ is rotated by $\Theta(x_k, y_k)$ around the center position (x_k, y_k) , using bilinear interpolation methods available in standard image rotation functions of MATLAB. Here, β has to be larger than the used Gaussian kernel size. The intensity profile perpendicular to the filament $f(y_{\perp}, x_k)$ at position x_k is then defined along the vertical axis y_{\perp} at the center of the rotated image. The black curve in Figure 2.9(f) shows the intensity profile along the red line in Figure 2.9(e). The refined center position \bar{y}_{\perp} (indicated by the vertical dashed blue line in Figure 2.9(f)) of $f(y_{\perp}, x_k)$ is determined by the

¹At a pixel size of 75 nm/pixel the distance between (x_{i+2}, y_{i+2}) and (x_{i-2}, y_{i-2}) is 300 nm if the filament is oriented along the x - or y -axis

COI method. This position needs to be projected back into the original image coordinates for the refined contour position (\bar{x}_k, \bar{y}_k) :

$$\begin{aligned}\bar{x}_k &= x_k - (\bar{y}_\perp - y_k) \sin(\Theta(x_k, y_k)) \\ \bar{y}_k &= y_k + (\bar{y}_\perp - y_k) \cos(\Theta(x_k, y_k))\end{aligned}\tag{2.11}$$

In step (iv) the skeleton was artificially extended by six pixel positions at each end. By this procedure more positions than actually belonging to the filament are obtained. To determine the correct filament size, positions exceeding the filament need to be removed. This is accomplished by a second threshold δ_f that determines whether the intensity profile $f(y_\perp, x_k)$ belongs to the filament or not. The white arrows in Figure 2.9(e) point at intensity profile lines at each filament end that need to be neglected. The average intensity at all initial² skeleton positions in the filtered image $\langle I(x_i, y_i) \rangle_{\text{fine}}$ is compared to the average $\langle f(y_\perp^{\text{max}}, x_k) \rangle$ of the maximum of $f(y_\perp^{\text{max}}, x_k)$ and its next neighbor values $f(y_\perp^{\text{max}} - 1, x_k)$ and $f(y_\perp^{\text{max}} + 1, x_k)$. Setting δ_f to about 30 to 50 % of $\langle I(x_i, y_i) \rangle_{\text{fine}}$ provides a good condition on whether (\bar{x}_k, \bar{y}_k) belongs to the filament or not.

(vi) In a final step the refined contour positions (\bar{x}_k, \bar{y}_k) need to be arranged equidistantly to each other along the filament contour. By linear interpolation the set of m equidistant refined contour positions $(\tilde{x}_k, \tilde{y}_k)$ is obtained and the overall filament position can be recovered:

$$\begin{aligned}x_0 &= \frac{1}{m} \sum_{k=1}^m \tilde{x}_k \\ y_0 &= \frac{1}{m} \sum_{k=1}^m \tilde{y}_k\end{aligned}\tag{2.12}$$

In Figure 2.9(g) the original image is overlaid with the refined contour (white line), and the overall filament position (x_0, y_0) is indicated by the red cross. The recovered filament length of the shown $[fd]_6$ virus is $L = \sum_{k=1}^{m-1} \sqrt{(\tilde{x}_{k+1} - \tilde{x}_k)^2 + (\tilde{y}_{k+1} - \tilde{y}_k)^2} = 5.27 \mu\text{m}$, which agrees perfectly with the expected length of $6 \times 0.88 \mu\text{m} = 5.28 \mu\text{m}$.

2.4.3. Gyration radius and orientation of extended particles

In addition to the center-of-mass position (x_0, y_0) , the overall orientation θ of extended particles can be determined. If a full contour recovery, as for fd -virus filaments, is possible, the orientation of the particle in the image is easily obtained from the direction of the end-to-end vector \mathbf{d}_{ee} between the first and the last contour position (see Figure 2.10(a)):

$$\theta_{\text{ee}} = \arctan \left(\frac{\mathbf{e}_{\text{ee}} \cdot \mathbf{e}_y}{\mathbf{e}_{\text{ee}} \cdot \mathbf{e}_x} \right),\tag{2.13}$$

²before adding positions to the ends

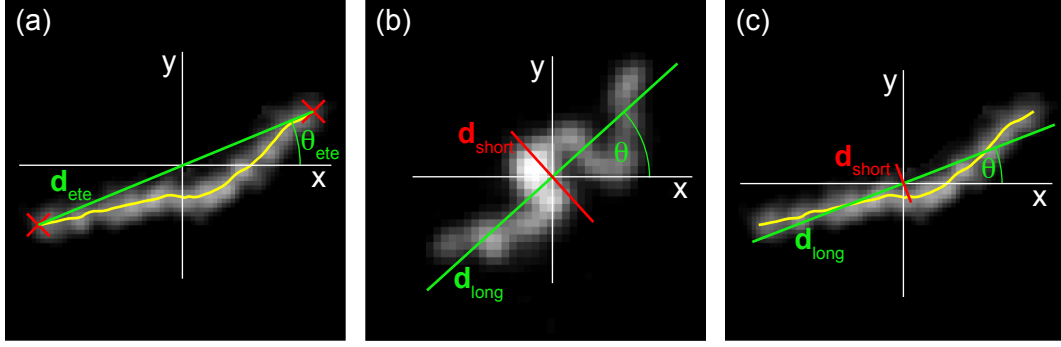


Figure 2.10: Orientation of elongated particles with known and unknown filament contour positions. (a) Orientation θ_{ee} as the angle between the end-to-end vector \mathbf{d}_{ee} (green line) and the x -axis. This method to determine the orientation is only possible if the contour positions $(\tilde{x}_k, \tilde{y}_k)$ (yellow line overlaid on the filtered image of an fd -virus filament) are known and \mathbf{d}_{ee} is connecting the first and the last position of the contour (red crosses). (b) Orientation θ as the angle between the long particle axis \mathbf{d}_{long} (green line) and the x -axis. For filaments without known contour, eigenvector \mathbf{e}_{long} to the largest eigenvalue λ_{long}^2 of the gyration tensor G_{ij} of the image intensity defines the long axis orientation of the imaged molecule. (c) Alternatively to \mathbf{d}_{ee} , the gyration tensor of the refined filament contour $(\tilde{x}_k, \tilde{y}_k)$ (yellow line) can be used, to determine the long axis \mathbf{d}_{long} and θ .

with the unit vectors \mathbf{e}_x and \mathbf{e}_y of x - and y -axis and the unit vector \mathbf{e}_{ee} along the end-to-end vector.

If no full contour analysis is possible, i.e. no end positions are known, the orientation of the long axis of the filament determines the particle orientation. This direction can be obtained from the two-dimensional gyration tensor G_{ij} that is describing the second moments of intensity of the Gaussian-filtered and background-reduced image:

$$G_{ij} = \frac{1}{\sum_{m,n} I_{mn}} \sum_{m,n} (r_{mn,i} - r_{0,i})(r_{mn,j} - r_{0,j}) I_{mn} \quad (2.14)$$

Here, I_{mn} is the intensity of the pixel $[m, n]$ of the Gaussian-filtered and background-reduced image, $r_{mn,i}$ is the cartesian coordinate (x for $i = 1$ or y for $i = 2$) of pixel $[m, n]$ and $r_{0,i}$ is the center position of the particle (x_0 for $i = 1$ or y_0 for $i = 2$).

G_{ij} has two eigenvalues λ_{long}^2 and λ_{short}^2 , with $\lambda_{long}^2 \geq \lambda_{short}^2$. The respective eigenvectors \mathbf{e}_{long} and \mathbf{e}_{short} determine the orientation of the long axis, and perpendicular to it, the short axis of the imaged particle and define its orientation which can be expressed in terms of a polar angle

$$\theta = \arctan \left(\frac{\mathbf{e}_{long} \cdot \mathbf{e}_y}{\mathbf{e}_{long} \cdot \mathbf{e}_x} \right). \quad (2.15)$$

Furthermore, the eigenvalues can be used to calculate the gyration radius R_g :

$$R_g = \sqrt{\lambda_{long}^2 + \lambda_{short}^2} \quad (2.16)$$

In Figure 2.10(b) the long axis (green) as well as the short axis (red) obtained via the gyration eigenvectors of a λ -DNA molecule are shown. The long axis defines the orientation of the filament without the necessity to determine the DNA contour.

While being the single possibility to determine the orientation of macromolecules without known contour, the gyration tensor method can also be used as an alternative to the end-to-end orientation when the contour of a semiflexible rod-shaped particle is available. In this case, the full map of image intensities is not necessary, and the gyration tensor can instead be calculated from a known set of m equidistant contour points $(\tilde{x}_k, \tilde{y}_k)$ shown as a yellow line in Figure 2.10(c):

$$G_{ij} = \frac{1}{m} \sum_{k=1}^m (\tilde{r}_{k,i} - r_{0,i})(\tilde{r}_{k,j} - r_{0,j}), \quad (2.17)$$

where $\tilde{r}_{k,i}$ is the k -th point belonging to the contour (\tilde{x}_k for $i = 1$ or \tilde{y}_k for $i = 2$) and $r_{0,i}$ is the center-of-mass position in the respective coordinate. The overall orientation θ of the filament contour determined in this way is exactly equal to θ_{ee} if the filament is a straight line; generally, however, $\theta \neq \theta_{ee}$. The eigenvalues of the gyration tensor of the filament contour (Equation (2.17)) allows one to calculate the gyration radius R_g according to Equation (2.16).

2.4.4. Constructing particle trajectories

After all particle positions are determined in every frame of an image time stack, the particles need to be identified in every consecutive frame to determine the displacements of individual

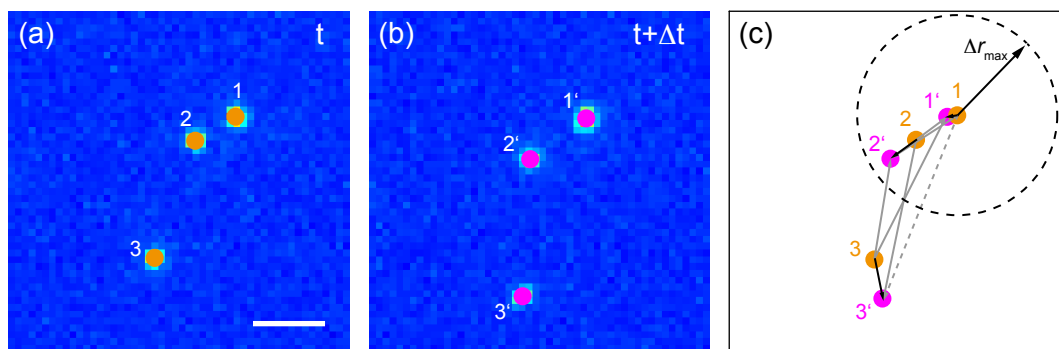


Figure 2.11: Trajectory reconstruction by identification of particles in different frames. Tracked positions 1, 2, and 3 (orange dots) of fluorescent beads with 50 nm radius diffusing on a lipid membrane at time t (a), and new positions 1', 2' and 3' (magenta dots) after a time interval between frames $\Delta t = 1.5$ s (b). Scale bar 5 μm . (c) A least cost algorithm identifies the particles of frame (a) in frame (b) by minimizing the total squared displacement between all positions. The resulting displacements are indicated by the black arrows, and particle trajectories are constructed from consecutive steps. Gray arrows show the other displacement possibilities. For example, particle 1 could have moved to positions 1', 2' or 3'. By introducing a maximum displacement between frames Δr_{max} , as visualized by the dashed black circle around position 1, the displacement to position 3' (via the dashed grey arrow) is eliminated.

particles and merge them into single particle trajectories. A least cost algorithm is used that relates all n particle positions in the previous image to all m particle positions in the current image. By finding the minimal total squared displacement the most likely particle displacements are chosen [100]. A maximum allowed displacement Δr_{\max} is introduced. This reduces the amount of possible displacements that need to be considered and thereby significantly enhances the speed of the particle identification process, especially when the number of particles is large. Furthermore, if a particle position in the current frame is not associated with a position of any other particle in the previous frame, a punitive Δr_{\max}^2 is added to the total squared displacement. It is important to set Δr_{\max} large enough in relation to the diffusion constant D and the time between consecutive frames because D will be underestimated otherwise. At $\Delta r_{\max} = 2.55\sqrt{4D\Delta t}$, the determined D will reach 99 % of its actual value [106]. For all tracking procedures used in the present Thesis Δr_{\max} was set to at least $4\sqrt{4D\Delta t}$. Figure 2.11 illustrates the above process of trajectory construction using two images of fluorescent beads separated by $\Delta t = 1.5$ s.

2.4.5. Determination of translational diffusion coefficients

The diffusion coefficient is obtained from the displacements $\Delta \mathbf{r}(t) = \Delta \mathbf{x}(t) + \Delta \mathbf{y}(t)$ retrieved from the particle trajectory. It is either possible to analyze every particle trajectory on its own and determine the overall D as a mean of the distribution of individual particle diffusion coefficients, or to merge all displacements of different particles together and analyze the collective distributions. The latter approach assumes the equality of all particle properties and a spatially homogeneous environment. In the following the diffusion analysis based on the first approach to analyze single trajectories will be described, as it allows one to investigate the behavior of individual particles.

A trajectory of N positions (x_i, y_i) and a time between frames Δt , as shown in Figure 2.12(a), is split into its $N - m$ displacements $\Delta \mathbf{r}_i(t)$, where n is an integer determining the number of time steps between frames. The $N - m$ step distances $\Delta r_i(t)$ can be calculated as:

$$\Delta r_i(t) = \sqrt{\Delta x_i^2(t) + \Delta y_i^2(t)}, \quad (2.18)$$

with $t = m\Delta t$, $\Delta x_i(m\Delta t) = x_{i+m} - x_i$ and $\Delta y_i(m\Delta t) = y_{i+m} - y_i$.

As shown in Section 1.2.1, all one-dimensional displacements $\Delta x(m\Delta t)$ and $\Delta y(m\Delta t)$ are Gaussian distributed for all time steps $m\Delta t$ in case of normal diffusion (see Equation (1.4)). The displacements can be histogrammed and analyzed using a Gaussian distribution with variance $\sigma^2 = 2Dm\Delta t$:

$$\rho(\Delta x(m\Delta t), m\Delta t)d\Delta x = \frac{N - m}{\sqrt{4\pi Dm\Delta t}} \exp\left(-\frac{\Delta x^2(m\Delta t)}{4Dm\Delta t}\right) d\Delta x \quad (2.19)$$

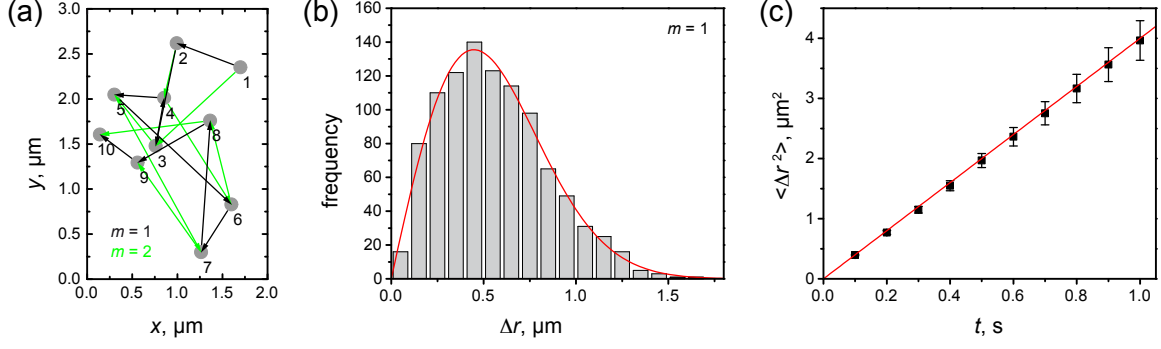


Figure 2.12: Determination of translational diffusion coefficients from trajectories. (a) The gray dots are the first ten points – labeled from 1 to 10 – of a simulated particle trajectory with $D = 1 \mu\text{m}^2/\text{s}$ and $\Delta t = 0.1 \text{ s}$. Shown in black are the nine displacements between consecutive images $\Delta \mathbf{r}_i(\Delta t)$ that constitute the trajectory. Furthermore, all eight displacements $\Delta \mathbf{r}_i(2\Delta t)$ are shown in green. (b) The distribution of all step distances $\Delta r_i(\Delta t)$ of a simulated trajectory with 1000 positions is shown by the histogram and overlaid with the theoretical Rayleigh distribution in red, calculated from Equation (2.22) with the known parameters of the simulated trajectory $D = 1 \mu\text{m}^2/\text{s}$ and $\Delta t = 0.1 \text{ s}$. (c) MSD $\langle \Delta r^2(m\Delta t) \rangle$ up to $m = 10$ calculated from the same trajectory as in (b). Error bars indicate the statistical reliability of each point according to [44] (Equation (2.24)). The red line shows the theoretically expected linear growth with time at $4Dm\Delta t$ for a two-dimensional MSD.

Here, for correct normalization, the prefactor $(N - m)$ is needed to reflect the number of displacements contributing to the distribution. For creating the displacement histogram an adequate bin size $d\Delta x$ has to be found. It is calculated according to the Freedman-Diaconis rule for using a histogram as a density estimator [107] for a normal distribution:

$$d\Delta x = 2\text{IQR}(\Delta x(m\Delta t)) (N - m)^{-\frac{1}{3}}, \quad (2.20)$$

with the interquartile range IQR as a measure of the width of the distribution.

Alternatively, the distribution of the two-dimensional step distances $\Delta r(m\Delta t)$ can be analyzed. Using Equation (1.3), the distribution of the two dimensional case is

$$\rho(\Delta r(m\Delta t), m\Delta t) d\Delta x d\Delta y = \frac{N - m}{4\pi D m \Delta t} \exp\left(-\frac{\Delta r^2(m\Delta t)}{4D m \Delta t}\right) d\Delta x d\Delta y, \quad (2.21)$$

and after substitution of $d\Delta x d\Delta y = \sin \phi \Delta r d\Delta r d\phi$ and integration over ϕ from 0 to 2π

$$\rho(\Delta r(m\Delta t), m\Delta t) d\Delta r = (N - m) \frac{\Delta r(m\Delta t)}{2D m \Delta t} \exp\left(-\frac{\Delta r^2(m\Delta t)}{4D m \Delta t}\right) d\Delta r. \quad (2.22)$$

Equation (2.22) is a Rayleigh distribution with variance $\sigma^2 = 2Dm\Delta t$. Figure 2.12 (b) shows the histogram of displacements at $m = 1$ for a simulated trajectory with $N = 1000$ which is overlaid with the theoretical expectation according to Equation (2.22).

Analysis of the distributions of displacements Δx and Δy or of the step distances Δr

is the easiest way to investigate whether the diffusion of a single particle or all particles combined is indeed normal and isotropic in a homogeneous environment, since deviations of the former situation result in changes of the distribution shape. For example, for proteins forming dynamic wave patterns upon interaction with a supported membrane, the analysis of the Rayleigh distribution revealed different mobilities of the proteins depending on their relative lateral position within the wave [108]. However, the histogramming of a finite amount of displacements can – even if done correctly – affect the determination of D , which poses a disadvantage of this method.

If a normal distribution of displacements can be assumed, the method most commonly used to determine D from a trajectory is the calculation and analysis of the mean squared displacement (MSD). Using Equation (1.5), the two-dimensional MSD calculated from the squared displacements, can be related to D as follows:

$$\langle \Delta r^2(m\Delta t) \rangle = \frac{1}{N-m} \sum_{i=1}^{N-m} \Delta x_i^2(m\Delta t) + \Delta y_i^2(m\Delta t) = 4Dm\Delta t. \quad (2.23)$$

The statistical uncertainty of each point in the MSD depends on the length of the trajectory and therefore the number of independent displacements over which the average is taken. The relative statistical error can be calculated as follows [44]:

$$\frac{\Delta \langle \Delta r^2(m\Delta t) \rangle}{\langle \Delta r^2(m\Delta t) \rangle} \cong \left[\frac{2m^2 + 1}{3m(N-m)} \right]^{\frac{1}{2}} \quad (2.24)$$

for $N - m \gg m$. Equation (2.24) accounts for the fact that while for $m = 1$ all $N - 1$ displacements are independent, correlations appear for $m > 1$; at $m = 2$, the displacements from trajectory position (x_1, y_1) to (x_3, y_3) and from (x_2, y_2) to (x_4, y_4) are not entirely independent since both 'include' the displacement from (x_2, y_2) to (x_3, y_3) , and so on. As an example, in Figure 2.12(c) the first ten points of a MSD calculated from a simulated trajectory of $N = 1000$, including the statistical errors according to Equation (2.24) are shown. The estimation of the statistical error was shown to be valid, as long as the localization accuracy ξ is at least of order of $\sqrt{D\Delta t}$ [109]. All MSDs were fitted with a weighted fit accounting for the statistical error.

Ideally the length of an analyzed trajectory should be very long to obtain the diffusion coefficient with a high accuracy. However, in the reality of an experiment, particle trajectories have a length shorter than the number of accumulated frames for many reasons: a particle leaving the ROI, a particle having a brightness below the intensity threshold in one of the frames, or just getting very close to another particle, to name a few. Generally all trajectories analyzed in this thesis consisted of at least $N = 50$ positions. For some experiments this threshold for using the trajectory to extract the information on the diffusion coefficient was

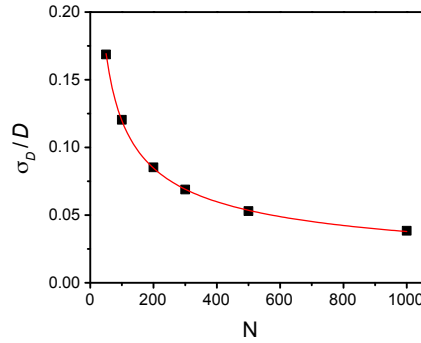


Figure 2.13: Statistical uncertainty of the diffusion coefficient determination, depending on the trajectory length N . For each N , ranging from 50 to 1000, 10^4 trajectories were simulated and analyzed using a weighted fit to the MSD with $m = 5$ points. The standard deviation σ_D of the resulting distribution of diffusion coefficients was determined and the relative error σ_D/D is plotted and can be fitted as $\sigma_D/D = (1.2 \pm 0.01)/\sqrt{N}$ (red curve).

set as high as $N = 400$ positions. Calculating the mean diffusion coefficient for an experiment from a set of diffusion coefficients obtained from individual trajectories of quite a broad length distribution, ranging from $N = 50$ to $N = 2000$, requires a sound statistical weighting of the individual D according to the trajectory length. Various works give an estimate of the standard deviation σ_D of a distribution of D [44, 109, 110]. In all of them the scaling of $\sigma_D \sim 1/\sqrt{N}$ is suggested, multiplied by a constant prefactor which depends on the number of fitted MSD points and potential offsets due to noise therein. Here, the following formula was used to calculate the weighted mean \bar{D} of a distribution of diffusion coefficients D_i extracted from trajectories of individual particles:

$$\bar{D} = \frac{\sum D_i/\sigma_{D_i}^2}{\sum 1/\sigma_{D_i}^2}. \quad (2.25)$$

A constant prefactor in σ_D does not change the result and the scaling of the error with $1/\sqrt{N}$ in principle is enough. Nonetheless, to validate the analysis method for the experimental data using weighted fitting of the MSD up to $m = 5$, a computer simulation of trajectories was carried out. The resulting standard deviations of the diffusion coefficient distributions obtained from 10^4 trajectories for every trajectory length N were investigated. An empirical dependence

$$\sigma_D \approx \frac{1.2D}{\sqrt{N}} \quad (2.26)$$

was found based on the simulations (see Figure 2.13) and used to calculate the weighted mean \bar{D} where necessary.

Influence of dynamic and static localization errors on the MSD

As mentioned above, the determined particle positions $(x(t), y(t))$ are only accurate up to a total localization error that results from two sources.

The first one is, the static localization error. In an experiment, the position of an immobile particle can only be obtained to a certain accuracy due to a finite amount of collected photons and various sources of noise [103, 111]. The measured position – for example in the x direction – is

$$x(t) = \hat{x}(t) + \chi(t), \quad (2.27)$$

with the real particle position $\hat{x}(t)$ and random error $\chi(t)$ with the zero mean $\langle \chi(t) \rangle = 0$ and nonzero variance $\langle \chi^2(t) \rangle = \xi^2$. It is also assumed that this error is not correlated in time: $\langle \chi(t)\chi(t') \rangle = \xi^2\delta(t - t')$.

Second, the dynamic localization error resulting from the motion of the particle during the time of the image acquisition t_{acq} leading to an averaged position $\bar{x}(t, t_{\text{acq}})$.

$$\bar{x}(t, t_{\text{acq}}) = \frac{1}{t_{\text{acq}}} \int_0^{t_{\text{acq}}} \hat{x}(t - t') dt' \quad (2.28)$$

The localization errors change the variance σ^2 of the displacement distributions and need to be accounted for in the analysis. In case of normal Brownian motion this amounts to adding constant terms for the dynamic and the static error [109, 111, 112, 113]:

$$\sigma^2(m\Delta t) = 2D \left(m\Delta t - \frac{t_{\text{acq}}}{3} \right) + 2\xi^2 \quad (2.29)$$

This translates to the two dimensional MSD as

$$\langle \Delta r^2(m\Delta t) \rangle = 4D \left(m\Delta t - \frac{t_{\text{acq}}}{3} \right) + 4\xi^2. \quad (2.30)$$

The term for the dynamic error $-4Dt_{\text{acq}}/3$ can easily be included in the fit of the MSD since t_{acq} is known and controlled by the experimenter. The static error $4\xi^2$ can be determined experimentally by measuring the localization precision ξ^2 of immobilized particles of the same kind as the mobile particles. The MSD – starting from $m = 1$ – can be fitted with a fixed constant offset applying this knowledge. However, ξ^2 depends on the particle brightness, e.g. the number of photons collected [103, 109, 110]. Since intensity fluctuations or brightness variations between particles cannot always be avoided, it proved useful to include a free constant term in the fit of the MSD that accounts for the static error in the position determination.

2.4.6. Determination of rotational diffusion coefficients

The rotational diffusion coefficient D_R can be determined using a similar approach as the one used in case of the lateral diffusion coefficient. Using an angular trajectory of N orientations θ_i , $N - m$ displacements $\Delta\theta_i(m\Delta t) = \theta_{i+m} - \theta_i$ can be calculated, and for rotation about a single fixed axis the MSD can be calculated as follows (see Equation (1.9)):

$$\langle \Delta\theta^2(m\Delta t) \rangle = \frac{1}{N - m} \sum_{i=1}^{N-m} \Delta\theta_i^2(m\Delta t) = 2D_R m\Delta t. \quad (2.31)$$

As in case of translational diffusion, the angular MSD obtained from experimental data can be analyzed with a constant offset term to account for static and dynamic localization errors (see Section 2.4.5).

Notably, there is an important difference in the determination of the angular trajectory compared to the translational trajectory which, if not accounted for, can yield faulty results. While the translational trajectory is directly derived from the set of unique coordinates x and y , the angle θ can only be determined within the range of $(0, 2\pi)$ at best. If Equations (2.13) and (2.15) are used, this range is reduced further to π , as the arctangent is discontinuous and gives values only from $-\pi/2$ to $\pi/2$. The arctangent-based approach is suitable for determination of the orientation of a filament which is point symmetric to its center-of-mass, because no more accurate definition of the orientation than up to π exists. With only non-unique coordinates recovered, the trajectory has to be constructed from angular displacements between consecutive frames before analysis. This additionally worsens the situation, since one cannot decide whether a center-of-mass symmetric filament rotated clockwise or counter-clockwise. The only condition where the complete trajectory can be recovered is the situation when no steps larger than $\pi/2$ can be made. This results in a limited ability to reconstruct the correct trajectories for large D_R at a specific experimental time resolution Δt , because with increasing D_R the probability of steps which are larger than $\pi/2$ grows.

Figure 2.14(a-c) shows examples of simulated angular trajectories (blue curve) for a frame time $\Delta t = 32 \text{ ms}$ ³, the values of θ as recovered by the image analysis (red curve) and the reconstructed angular trajectory (black curve) for three different values of D_R^{sim} . At $D_R^{\text{sim}} = 1 \text{ rad}^2/\text{s}$ the probability that displacements between consecutive frames $\Delta\theta$ are larger than $\pi/2$ is so low that within the $N = 1000$ simulated orientational positions virtually none occurs and the original trajectory is recovered perfectly (Figure 2.14(a)). Therefore, also the angular MSDs calculated from the original (blue open squares) and the reconstructed trajectory (black triangles) are identical (see Figure 2.14(d)), and the rotational diffusion coefficients determined using the MSD obtained for the original (simulated) trajectory D_R^{orig} and reconstructed tra-

³32 ms is the shortest sampling time possible in full chip read out mode of the EMCCD camera used in the present work.

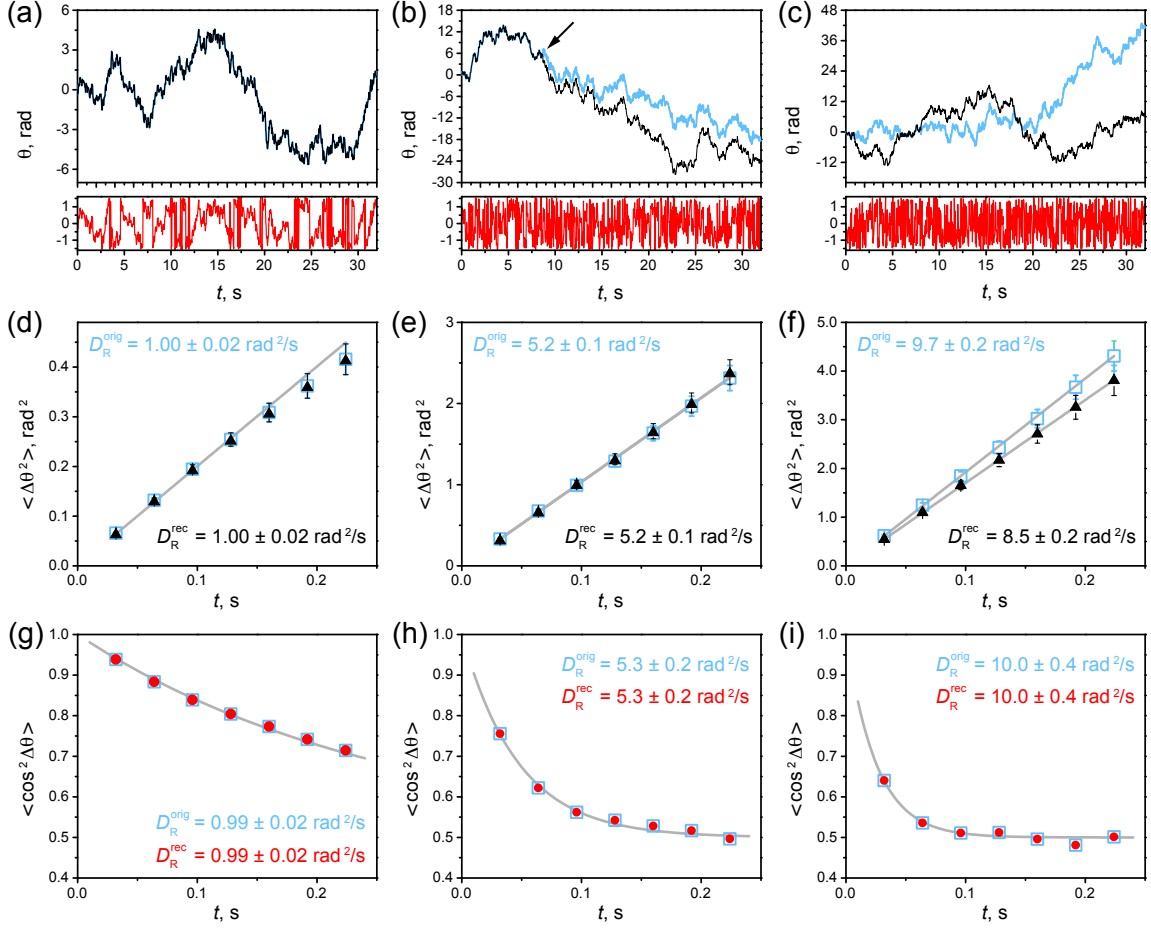


Figure 2.14: Ability to recover angular trajectories and rotational diffusion coefficients with growing D_R at constant frame time $\Delta t = 32$ ms. (a, d, g) $D_R^{\text{sim}} = 1 \text{ rad}^2/\text{s}$; (b, e, h) $D_R^{\text{sim}} = 5 \text{ rad}^2/\text{s}$; and (c, f, i) $D_R^{\text{sim}} = 10 \text{ rad}^2/\text{s}$. (a), (b) and (c) Comparison of simulated (blue curves) and reconstructed angular trajectories (black curves). Reconstructed trajectories were recovered using the angles obtained directly from the image (red curves). Displacements larger $\pi/2$ in the simulated original trajectory lead to deviations (black arrow) between original and reconstructed trajectory. (d), (e), and (f) MSDs calculated from the simulated original angular trajectory (blue open squares) and the reconstructed angular trajectories (black triangles) in (a), (b) and (c), respectively. (g), (h) and (i) Angular correlation functions computed using the simulated original angles (blue open squares) and the angles obtained from the image (red circles) in (a), (b) and (c), respectively.

jectory D_R^{rec} are the same. At a larger $D_R^{\text{sim}} = 5 \text{ rad}^2/\text{s}$ the probability of large displacements rises, and the reconstructed trajectory differs from the simulated trajectory starting from the first occurrence of $\Delta\theta > \pi/2$, as indicated by the arrow in Figure 2.14(b). Still, the overall shape of the reconstructed trajectory is similar to the original one and if only the first few points of the respective MSDs are considered, the determination of D_R is barely affected (see Figure 2.14(e)). With a further increase to $D_R^{\text{sim}} = 10 \text{ rad}^2/\text{s}$ the shape of the reconstructed trajectory differs significantly from the original trajectory (Figure 2.14(c)). Under these circumstances the determination of D_R^{rec} using the MSD is strongly affected, as shown

in Figure 2.14(f). The clear tendency towards the underestimation of $D_{\text{R}}^{\text{rec}}$ is apparent, as the MSD values calculated from the reconstructed trajectory (black triangles) are significantly smaller than those calculated from the original trajectory (blue open squares).

To avoid this problem, one can alternatively evaluate the angular correlation function of $\langle \cos^2 \Delta\theta(m\Delta t) \rangle$. Computing this function does not require reconstruction of a trajectory, and therefore, uses the full range of defined orientations of a filament with displacements as large as π instead of $\pi/2$. The angular correlation for every time step $m\Delta t$ can be easily calculated using the N eigenvectors of the orientation $\mathbf{e}_{\text{long},i}$ or the normalized end-to-end vector $\mathbf{e}_{\text{ee},i}$ respectively (see Section 2.4.3):

$$\langle \cos^2 \Delta\theta(m\Delta t) \rangle = \frac{1}{N-m} \sum_{i=1}^{N-m} (\mathbf{e}_i \cdot \mathbf{e}_{i+m})^2 \quad (2.32)$$

The theoretical expression for $\langle \cos^2 \theta(t) \rangle$ can be derived starting with the rotational diffusion equation (similar to Equation (1.2)):

$$\frac{\partial \rho(\theta, t)}{\partial t} = D_{\text{R}} \frac{\partial^2}{\partial \theta^2} \rho(\theta, t). \quad (2.33)$$

Here, $\rho(\theta, t)$ is the one-dimensional conditional probability to find the orientation of a Brownian particle at an interval $[\theta, \theta + d\theta]$ at time t , provided that at time $t = 0$, $\theta = 0$. Multiplying Equation (2.33) with $\sin^2 \theta$ and taking an integral over θ from 0 to 2π

$$\frac{\partial}{\partial t} \int_0^{2\pi} \sin^2 \theta \rho d\theta = D_{\text{R}} \int_0^{2\pi} \sin^2 \theta \frac{\partial^2 \rho}{\partial \theta^2} d\theta, \quad (2.34)$$

yields, after two consecutive partial integrations of the right hand side, to the following equations:

$$\frac{\partial}{\partial t} \langle \sin^2 \theta \rangle = 2D_{\text{R}}(1 - 2\langle \sin^2 \theta \rangle). \quad (2.35)$$

The solution of this equation is

$$\langle \sin^2 \theta \rangle = \frac{1}{2}[1 - \exp(-4D_{\text{R}}t)], \quad (2.36)$$

and therefore with the use of the identity $\langle \sin^2 \theta \rangle = \langle 1 - \cos^2 \theta \rangle = 1 - \langle \cos^2 \theta \rangle$ one obtains

$$\langle \cos^2 \theta(t) \rangle = \frac{1}{2}[1 + \exp(-4D_{\text{R}}t)]. \quad (2.37)$$

To account for dynamic and static localization errors of the orientation, an amplitude A of the exponential term can be introduced and included as a parameter in the nonlinear least

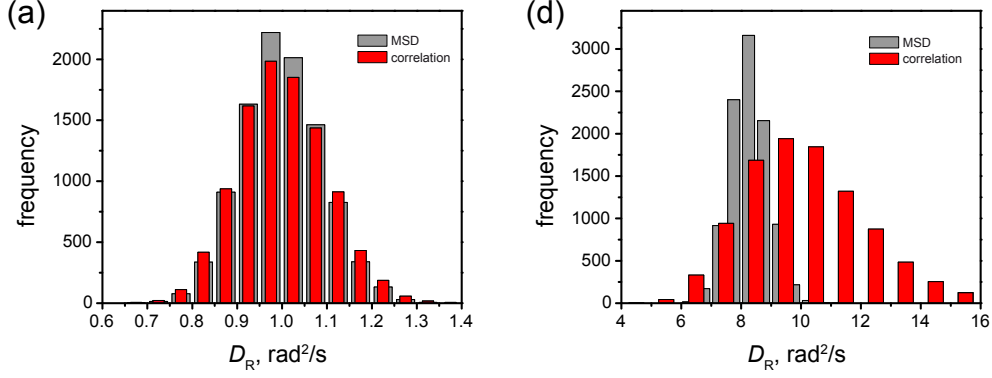


Figure 2.15: Histograms of rotational diffusion coefficients obtained from 10^4 angular trajectories to validate the D_R determination using the angular MSD (gray bars) as in Equation (2.31) fitted with a constant offset and the angular correlation (red bars) as in Equation (2.38). A static error $\xi = 0.175$ rad = 10° and the dynamic error due to motion blur over the image acquisition time $t_{\text{acq}} = 30$ ms were included in the trajectory simulation to reproduce the experimental situation. (a) Diffusion coefficient distributions for $D_R^{\text{sim}} = 1$ rad²/s. The mean values of the diffusion coefficients are $\bar{D}_R^{\text{MSD}} = 1.00 \pm 0.09$ rad²/s and $\bar{D}_R^{\text{cor}} = 1.00 \pm 0.1$ rad²/s using the MSD and the angular correlation method, respectively. (b) Diffusion coefficient distributions for $D_R^{\text{sim}} = 10$ rad²/s. The mean values of the retrieved diffusion coefficients are $\bar{D}_R^{\text{MSD}} = 8.3 \pm 0.6$ rad²/s and $\bar{D}_R^{\text{cor}} = 10.2 \pm 2.1$ rad²/s.

square fit of $\langle \cos^2 \Delta\theta(m\Delta t) \rangle$ to

$$\langle \cos^2 \Delta\theta(m\Delta t) \rangle = \frac{1}{2} [1 + A \exp(-4D_R m\Delta t)], \quad (2.38)$$

for $m \geq 1$. For high contributions of the static error $A < 1$ and if the dynamic error dominates $A > 1$. Fits were carried out up to $m = 5$ for all experiments.

The angular correlation functions $\langle \cos^2 \Delta\theta(m\Delta t) \rangle$ calculated from the original angles (blue curves in Figure 2.14(a-c)) and the angles as obtained from the image (red curves in Figure 2.14(a-c)) are displayed in Figure 2.14(g-i). As can be seen, the correlation functions (blue open squares as calculated from the original values of θ and red circles as calculated from the angles directly obtained from the image) are identical for all D_R^{sim} . This allows one to obtain the correct value of D_R even if the rotational diffusion coefficient is as high as 10 rad²/s, and the MSD analysis fails (see Figure 2.14(c,f,i)).

In order to further demonstrate the possibilities of the analysis using the angular correlation method, a set of 10^4 angular trajectories for each of the two rotational diffusion coefficients $D_R^{\text{sim}} = 1$ rad²/s and $D_R^{\text{sim}} = 10$ rad²/s was simulated and analyzed. The distributions of diffusion coefficients, as determined from the 10^4 simulated angular trajectories of 1000 orientations each, and $\Delta t = 32$ ms are shown in Figure 2.15. They have been obtained by the analysis of the angular MSD (gray bars) and the angular correlation function (red bars). A static error $\xi = 0.175$ rad = 10° and a dynamic error due to motion blur over the image acquisition time $t_{\text{acq}} = 30$ ms were included in the trajectory simulation to reproduce the

experimental situation. For an initial diffusion coefficient $D_{\text{R}}^{\text{sim}} = 1 \text{ rad}^2/\text{s}$ both methods are able to recover the correct mean, with $\bar{D}_{\text{R}}^{\text{MSD}} = 1.00 \pm 0.09 \text{ rad}^2/\text{s}$ and $\bar{D}_{\text{R}}^{\text{cor}} = 1.00 \pm 0.1 \text{ rad}^2/\text{s}$ (see Figure 2.15(a)). However, as shown in Figure 2.15(b), the MSD method clearly fails to reproduce the larger diffusion coefficient $D_{\text{R}}^{\text{sim}} = 10 \text{ rad}^2/\text{s}$, whereas the angular correlation method recovers the correct mean value of D_{R} : $\bar{D}_{\text{R}}^{\text{MSD}} = 8.3 \pm 0.6 \text{ rad}^2/\text{s}$ and $\bar{D}_{\text{R}}^{\text{cor}} = 10.2 \pm 2.1 \text{ rad}^2/\text{s}$.

Generally, the validity of all experimental analysis performed in this work was checked by simulations with the experimentally relevant parameters.

2.4.7. Anisotropy in the translational diffusion of extended particles

In this Thesis the translational diffusion of an *fd*-virus particle attached to a membrane is investigated. The *fd*-virus has a strong shape anisotropy with a ratio of about 130 between filament length and diameter for a virus monomer. As a consequence one expects that the viscous drag for motion parallel to the elongation of the virus is significantly different compared to the viscous drag normal to the elongation.

Generally, for extended particles which have a shape anisotropy, the viscous drag coefficient, and therefore the general diffusion coefficient, is not a scalar but a tensor. Consequently, the translational diffusion can be decomposed into the scalar diffusion coefficients perpendicular to the long axis of the particle D_{\perp} and parallel to the long axis of the particle D_{\parallel} which reflect the respective viscous drag experienced by the particle. The value of the two-dimensional translational diffusion coefficient is related to the decomposed diffusion coefficients as $D_{\text{T}} = (D_{\perp} + D_{\parallel})/2$ [114], where $D_{\perp} \leq D_{\parallel}$ due to smaller hydrodynamic friction for the motion parallel to the long axis of the particle.

In order to determine the anisotropy of the translational diffusion, two one-dimensional trajectories describing the motion parallel and perpendicular to the instantaneous orientation of the particle have to be found. For every particle position in the lab frame, we introduce a local coordinate system $\zeta_{\parallel}, \zeta_{\perp}$ determined by the instantaneous orientation of the particle. It is defined such that ζ_{\parallel} is oriented along the eigenvector \mathbf{e}_{long} of the long particle axis, and ζ_{\perp} is oriented along the eigenvector $\mathbf{e}_{\text{short}}$ of the short particle axis (see Figure 2.16(a) and Section 2.4.3). Starting from the first particle position of a trajectory in the lab frame, the displacement to the subsequent particle position has to be decomposed into the local coordinates $\Delta\zeta_{\parallel}$ and $\Delta\zeta_{\perp}$. $\Delta\zeta_{\parallel}$ and $\Delta\zeta_{\perp}$ are obtained using the displacement vector in the lab frame $\Delta\mathbf{r}$ and the eigenvectors defining the instantaneous local coordinate system:

$$\begin{aligned}\Delta\zeta_{\parallel} &= \mathbf{e}_{\text{long}} \cdot \Delta\mathbf{r} \\ \Delta\zeta_{\perp} &= \mathbf{e}_{\text{short}} \cdot \Delta\mathbf{r}.\end{aligned}\tag{2.39}$$

The consecutive $\Delta\zeta_{\parallel}$ and $\Delta\zeta_{\perp}$ are used to reconstruct the corresponding one-dimensional

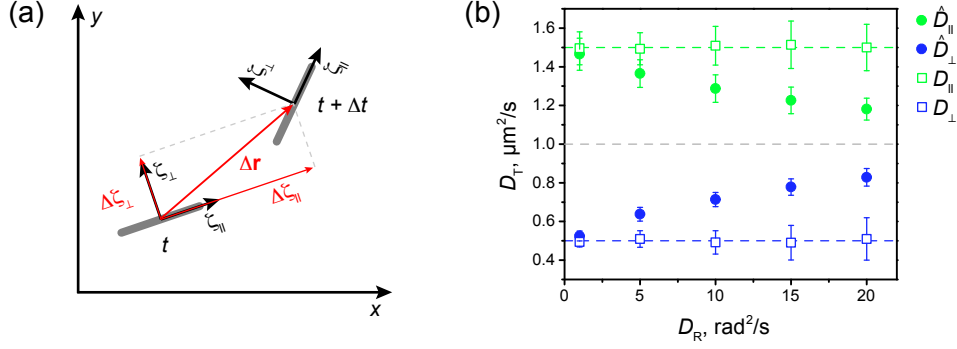


Figure 2.16: (a) Decomposing the lateral displacements of an extended Brownian particle in a local coordinate system $\zeta_{\parallel}, \zeta_{\perp}$ defined by the particle's instantaneous orientation. (b) Loss in translational diffusion anisotropy with growing rotational diffusion, and successful correction.

trajectories of the particle motion in the particle frame which are analyzed as described above (see Section 2.4.5) to obtain the translational diffusion coefficients for diffusion parallel \hat{D}_{\parallel} and perpendicular \hat{D}_{\perp} to an elongated particle.

Since Brownian particles undergo translational and rotational motion at the same time, the anisotropy in the determined translational diffusion coefficients \hat{D}_{\parallel} and \hat{D}_{\perp} , is dissipatively coupled to the rotational motion. This phenomenon was first explored theoretically by Perrin for free three-dimensional diffusion of ellipsoids [115, 116]. As a consequence, \hat{D}_{\parallel} and \hat{D}_{\perp} deviate from D_{\perp} and D_{\parallel} , and become equal when measured at timescales $\Delta t \gg \tau_R$, with the rotational relaxation time $\tau_R = 1/(2D_R)$ and the time Δt between consecutive recorded particle positions and orientations. Recently, this transition was investigated experimentally, for two-dimensional diffusion of an ellipsoid [114].

If the Δt is of order of τ_R , the experimentally determined diffusion coefficients \hat{D}_{\parallel} and \hat{D}_{\perp} are affected by the loss of memory of the initial particle orientation, leading to a reduced anisotropy of the diffusion coefficients [114]:

$$\begin{aligned} \hat{D}_{\parallel} &= D_T + \frac{D_{\parallel} - D_{\perp}}{2} \frac{1 - \exp(-4D_R\Delta t)}{4D_R\Delta t} \\ \hat{D}_{\perp} &= D_T - \frac{D_{\parallel} - D_{\perp}}{2} \frac{1 - \exp(-4D_R\Delta t)}{4D_R\Delta t}, \end{aligned} \quad (2.40)$$

where D_{\parallel} and D_{\perp} are the diffusion coefficients that would be obtained if $\Delta t \ll \tau_R$, i.e. if the rotational diffusion did not induce any loss of memory of the initial particle orientation. The above formulas are valid under the assumption that $D_{\perp} \leq D_{\parallel}$.

However, with knowledge about D_R and Δt , the corrected diffusion coefficients D_{\parallel} and D_{\perp} reflecting the anisotropy in the viscous drag experienced by the particle can be calculated

using Equation (2.40) and $D_T = (D_\perp + D_\parallel)/2 = (\hat{D}_\perp + \hat{D}_\parallel)/2$:

$$\begin{aligned} D_\parallel &= D_T + \frac{\hat{D}_\parallel - \hat{D}_\perp}{2} \frac{4D_R \Delta t}{1 - \exp(-4D_R \Delta t)} \\ D_\perp &= D_T - \frac{\hat{D}_\parallel - \hat{D}_\perp}{2} \frac{4D_R \Delta t}{1 - \exp(-4D_R \Delta t)}. \end{aligned} \quad (2.41)$$

To illustrate this possibility, particle trajectories with a translational diffusion anisotropy typical for the experiments described below, $D_\perp^{\text{sim}} = 0.5 \mu\text{m}^2/\text{s}$ perpendicular and $D_\parallel^{\text{sim}} = 1.5 \mu\text{m}^2/\text{s}$ parallel to an extended particle, were simulated. The trajectories consisted of 10^6 positions but only every 1000th position was taken into account for analysis leading to a frame time $\Delta t = 0.032$ s. 1000 trajectories were calculated for each of the different rotational diffusion coefficients $D_R^{\text{sim}} = 1, 5, 10, 15, 20 \text{ rad}^2/\text{s}$, and analyzed using the trajectory decomposition method according to the instantaneous particle orientation, as described above. The analysis yielded the translational diffusion coefficients \hat{D}_\parallel and \hat{D}_\perp that become progressively closer to each other and the mean diffusion coefficient $D_T^{\text{sim}} = 1 \mu\text{m}^2/\text{s}$ with an increase in D_R^{sim} , as shown in Figure 2.16(b). By using equation (2.41), the correct translational diffusion anisotropy represented by the diffusion coefficients D_\perp and D_\parallel are recovered.

2.4.8. Diffusion on curved surfaces of supergiant vesicles

In the present work, SGUVs are used as a model system for freestanding lipid membranes. Figure 2.17(a) shows a reconstructed 3D fluorescence image of such a vesicle with a diameter of about $200 \mu\text{m}$. As depicted in Figure 2.17(b), particles which interact with the lipid membrane can be conveniently investigated by means of fluorescence microscopy if the focal plane coincides with the pole of the vesicle. The acquired image of particles adsorbed to the curved membrane is a two-dimensional projection of the three-dimensional situation. This section is dedicated to find the maximal systematic error that occurs, when the curved vesicle membrane surface is treated as flat in the analysis of the experimental data of membrane-adsorbed particles.

First, in addition to the x, y coordinates describing the image plane in the image space Σ , a local coordinate system Σ' on the vesicle surface has to be defined, as illustrated in Figure 2.17(c). The maximal deviations from the true translational and orientational displacements and particle size, introduced by the treatment of the curved membrane surface as flat, need to be found. This problem does not depend on the azimuthal angle Φ and further considerations are based on the situation where $\Phi = 0$. Here, the planes spanned by x, z and x', z' coincide and y is parallel to y' (see Figure 2.17(c)). The area of the membrane surface at which no significant image distortions due to defocussing occur and which is thus available for experimental observations, is defined by the depth of focus h in the z direction. From the

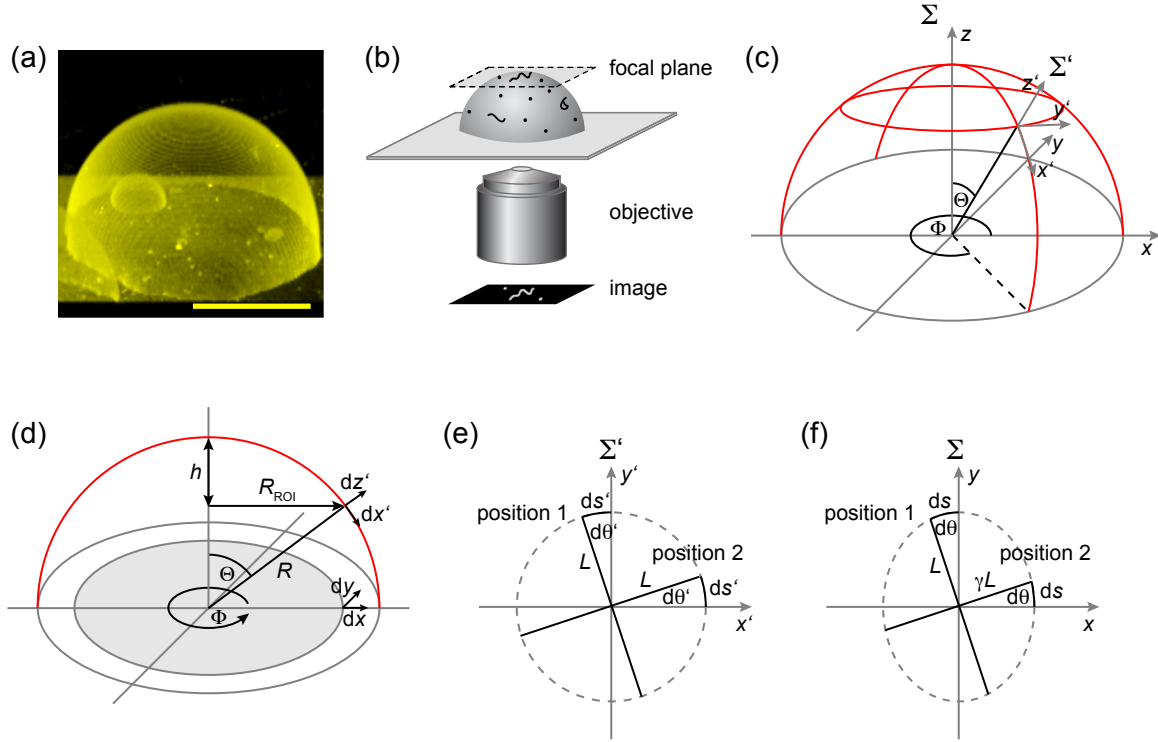


Figure 2.17: SGUVs as a model of a freestanding lipid membranes for diffusion measurements of membrane adsorbed particles. (a) Reconstructed 3D fluorescence image of a dome-like SGUV. Scale bar: 100 μm . (b) Schematic illustration of the image acquisition process in experiments addressing diffusion of membrane-bound particles by placing the focal plane of the objective at the top pole of the SGUV. (c) Sketch of the SGUV in the coordinate system Σ in which the x, y plane is the image plane and definition of the local particle coordinate system Σ' at the vesicle surface. (d) Sketch of the SGUV with the particle position at an azimuth angle $\Phi = 0$. At this angle the x, z and x', z' planes coincide and y' is parallel to y . For a depth of focus h all particles on the pole of the vesicle within a radius R_{ROI} from the center appear to be in focus. The respective ROI in the image plane is shown in gray. (e) Rotation of a rod-like particle of length $2L$ in the particles local coordinate system Σ' on the surface of the SGUV and (f) the projection of the rotation to the image plane in Σ . Position 1 marks the particle orientation $\theta = \theta' = \pi/2$ and position 2 marks the particle orientation $\theta = \theta' = 0$.

PSF shown in Figure 2.6(b) in Section 2.3.3 one can see that this is approximately the case for deviations from the focal plane $\lesssim 0.75 \mu\text{m}$ and thus $h = 1.5 \mu\text{m}$. The smallest radius of SGUVs used to investigate particle–membrane interactions was $R = 50 \mu\text{m}$. In this case the projected membrane area which can be observed in focus is defined by the radius $R_{\text{ROI}} = \sqrt{R^2 - (R - h)^2} = 12.1 \mu\text{m}$. The resulting ROI is indicated by the gray area in Figure 2.17(c). The largest deviations from the true particle trajectories, as well as particle sizes that are introduced by treating the membrane as flat, are found at the rim of this area. Here, the curvature angle of the vesicle surface in relation to the image plane is the highest. While at $\Phi = 0$ and $x = R_{\text{ROI}}$ no lateral deviations occur in the y direction, with $dy = dy'$, all lateral deviations are found along the x axis. The increment dx' is related to the inclination angle

of the sphere Θ as $dx' = Rd\Theta$. Using $\Theta = \arcsin(x/R)$ and therefore $d\Theta = 1/\sqrt{R^2 - x^2} dx$, yields at $x = R_{\text{ROI}}$

$$dx = \gamma dx'. \quad (2.42)$$

where $\gamma = \sqrt{1 - (R_{\text{ROI}}/R)^2}$. For the smallest vesicles used, with $R = 50 \mu\text{m}$ and $R_{\text{ROI}} = 12.1 \mu\text{m}$, the distortion factor $\gamma = 0.97$, i.e. the largest possible systematic error in lateral displacements and filament length is 3 %, if in the analysis of experimental data the polar vesicle surface in the ROI is simply assumed flat. The maximum systematic error this small and usually well below the statistical error is tolerable and does not justify complete remapping of determined position displacements and particle sizes with respect to the vesicle center, especially given that the center determination might be subjected to errors as well.

To access the systematic error of rotational displacements due to the curved vesicle surface, one should consider the rotation of a rod-like particle of length $2L$. At $\Phi = 0$, the particle orientations are recovered correctly at $\theta = \theta' = 0$ and $\theta = \theta' = \pi/2$. Figure 2.17(e) shows the rotation of the particle in its local coordinate system Σ' and Figure 2.17(f) the projection thereof to the image coordinate system Σ . Angular increments at the two extreme cases $\theta = \theta' = \pi/2$ (marked as position 1 in Figure 2.17(e,f)) and $\theta = \theta' = 0$ (marked as position 2 in Figure 2.17(e,f)) shall be considered. The line elements of the rotational displacement of the particle end are $ds' = \sqrt{dx'^2 + dy'^2}$ and $ds = \sqrt{dx^2 + dy^2}$.

At position 1 ($\theta = \pi/2$) the filament is oriented along the y axis, the filament length is not distorted and $ds' = dx'$ as well as $ds = dx$. Using $ds' = dx' = Ld\theta'$, $ds = dx = Ld\theta$ and $dx = \gamma dx'$ the relation between the angular increments $d\theta$ and $d\theta'$ is

$$d\theta = \gamma d\theta'. \quad (2.43)$$

At position 2 ($\theta = 0$) the filament is oriented along the x axis, leading to a filament length distortion of γL in Σ and $ds' = dy'$ as well as $ds = dy$. Using $ds' = dy' = Ld\theta'$, $ds = dy = \gamma Ld\theta$ and $dy = dy'$ the relation between the angular increments $d\theta$ and $d\theta'$ in this case is

$$d\theta = \gamma^{-1} d\theta'. \quad (2.44)$$

This results in underestimation of the angular displacement at position 1 by 3 % and overestimation of the angular displacement at position 2 by 3 % for the SGUV with $R = 50 \mu\text{m}$ and $R_{\text{ROI}} = 12.1 \mu\text{m}$. Again, the small maximum systematic error does not justify the complete remapping of all coordinates, which allows one to conclude that for all experimental purposes the slightly curved surface of the imaged SGUV pole ROI can be considered flat.

Cationic Supergiant Unilamellar Vesicles as an Experimental Model of Freestanding Lipid Membranes

Vesicles with radii of 50 μm or larger (supergiant unilamellar vesicles, SGUVs) can serve as a perfect model system mimicking a freestanding lipid bilayer. Especially useful in this respect are vesicles containing charged (anionic or cationic) lipids, which allow for investigation of charge-induced interactions between freestanding lipid membranes and colloidal particles or (bio)macromolecules. In this case, the interaction forces between the membrane and a colloidal particle or macromolecule can be reduced to electrostatics [18, 117, 118, 119, 120, 121, 122, 123], which makes it possible to study charge-related effects under the conditions of a minimum experimental system. Typically, experiments of this type are based on optical (fluorescence) microscopy with the help of which one can observe attachment/detachment of particles to the membrane, as well as Brownian motion and/or conformational dynamics of membrane-attached particles. SGUVs are particularly handy in these experiments. If microscopy observations are carried out on the upper pole of an SGUV the combination of the large vesicle size with a typical focal depth of a wide-field optical microscope ($\sim 1.5 \mu\text{m}$) allows one to image more than $450 \mu\text{m}^2$ of essentially flat freestanding membrane, as discussed in Section 2.4.8.

While GUVs and SGUVs of zwitterionic and/or anionic lipids can be easily electroformed virtually without any restrictions on the vesicle size, production of cationic vesicles with radii exceeding 10–20 μm using the standard electroformation procedure, as described in Section 2.2.2, appears to be notoriously difficult for the unknown reason, a conclusion based on previous reports [117] and personal observation in the experiments performed for this thesis. The first part of this chapter is focused on the goal to optimize the experimental procedure and to ensure the reproducible and efficient formation of cationic SGUVs.

One of the important parameters controlling the behavior of membrane-bound particles, including their mobility, is the surface viscosity of the membrane. In the second part of this chapter, the membrane surface viscosity of freestanding cationic DOPC/DOTAP membranes

used in this thesis is experimentally determined.

3.1. Efficient electroformation of cationic SGUVs

For studies of the interaction between colloidal particles/(bio)macromolecules and lipid membranes a good quality of the produced SGUV sample is essential. Apart from a significant amount of SGUVs in the sample, only very few small freely floating vesicles or tubular membrane structures are acceptable. These unwanted membrane structures would otherwise interact with the injected particles that are to bind to the SGUV membrane, before they reach their desired destination. Unfortunately, the quality of cationic SGUV samples obtained by the standard electroformation procedure (Section 2.2.2) was found to vary strongly in both respects, the maximum vesicle size obtained and smaller membrane structures present in the sample. In order to develop a procedure which would provide a consistent quality of cationic SGUVs, we carried out a systematic study on cationic SGUV electroformation using ITO-coated coverslips, which is presented in this section.

3.1.1. Experimental details

Standard vesicle electroformation

Vesicle electroformation using ITO-coated glass coverslips was carried out according to the procedure described in Section 2.2.2. The lipid composition for vesicle electroformation was 5 mol% of DOTAP and 95 mol% of DOPC for cationic SGUVs; 100 mol% of DOPC for zwitterionic SGUVs; and 5 mol% of DSPC and 95 mol% of DOPC for anionic SGUVs. The fluorescent lipid analogue DiD (0.1 mol%) was added to the lipid mixture to allow for fluorescence imaging of the obtained vesicles.

Control experiments with a different cationic lipid were carried out using 5 mol% of EDOPC and 95 mol% of DOPC.

Standard ITO coverslip cleaning procedure

ITO-coated coverslip electrodes are rather expensive, which is why a repeated use of those electrodes is a normal experimental practice. In order to reuse ITO glass electrodes after electroformation, the chamber is disassembled, and the copper tape contacts are removed from the ITO glass coverslips using acetone to dissolve the conductive glue. The ITO surface is cleaned by swabbing with 80:20 (v/v) ethanol-dd-H₂O mixture, followed by swabbing with acetone and again with ethanol; finally, it is rinsed with deionized water and dried under a flow of nitrogen.

Mild annealing of ITO coverslips in air

ITO-coated coverslips cleaned with the standard cleaning procedure were annealed immediately before starting the preparations for the electroformation procedure. For annealing, ITO-coated coverslips were placed with the ITO-coated surface facing air on a heating plate with the temperature set to 150 °C. After 20 min, the coverslips were removed from the heater and left to cool down to the room temperature, after which the lipid film was deposited on one of the coverslips, and the normal electroformation procedure was carried out as described above.

Atomic force microscopy

Atomic force microscopy (AFM) measurements were carried out using a NanoWizard I system (JPK Instruments, Germany). In all cases ITO-coated coverslips were imaged in 1 × PBS pH 7.4 at the room temperature (21 °C). PBS buffer was used to improve the spatial AFM resolution by screening long-range electrostatic forces which otherwise impede the AFM measurement if the ionic strength of the surrounding aqueous medium is too low [124]. The AFM was operated in the contact mode using non-coated silicon triangular cantilevers (CSC21, MikroMasch, Estonia) with a typical spring constant of 2 N/m. Each ITO-coated coverslip was scanned at three different spots of a size of 3 × 3 μm at a resolution of 512 × 512 pixels. To additionally characterize the image topography, surface-height histograms were computed for each of the AFM height images.

3.1.2. Aging effects of ITO coverslips with use

By relating the successful and failed attempts to produce SGUVs from cationic lipid mixtures with all experimental parameters, we managed to correlate the electroformation success rate with aging of ITO-coated coverslips. We found that the total number of times N the coverslips had previously been used to prepare vesicles is a convenient and reliable measure of their aging.

The use of a new ($N = 0$) set of ITO-coated coverslips consistently leads to efficient formation of SGUVs, as shown in Figure 3.1(a,b). The fluorescence microscopy image in Figure 3.1(a) shows GUVs which are attached to the ITO surface in a dome-like fashion, and have no small and floating membrane structures around them. SGUVs with diameters > 200 μm are frequently found within the sample. The maximum achievable size of vesicles substantially decreases already when the coverslips were used for the third time ($N = 2$) (see Figure 3.1(c,d)). Most GUVs are still attached to the coverslip but no vesicles with diameters > 200 μm can be found. Finally for $N > 3$, the vesicle quality becomes absolutely unacceptable (Figure 3.1(e,f)). Only a few GUVs with diameters mostly about 20 μm but no SGUVs are found, and in addition the sample contains many very small freely floating vesicles and tubular membrane structures.

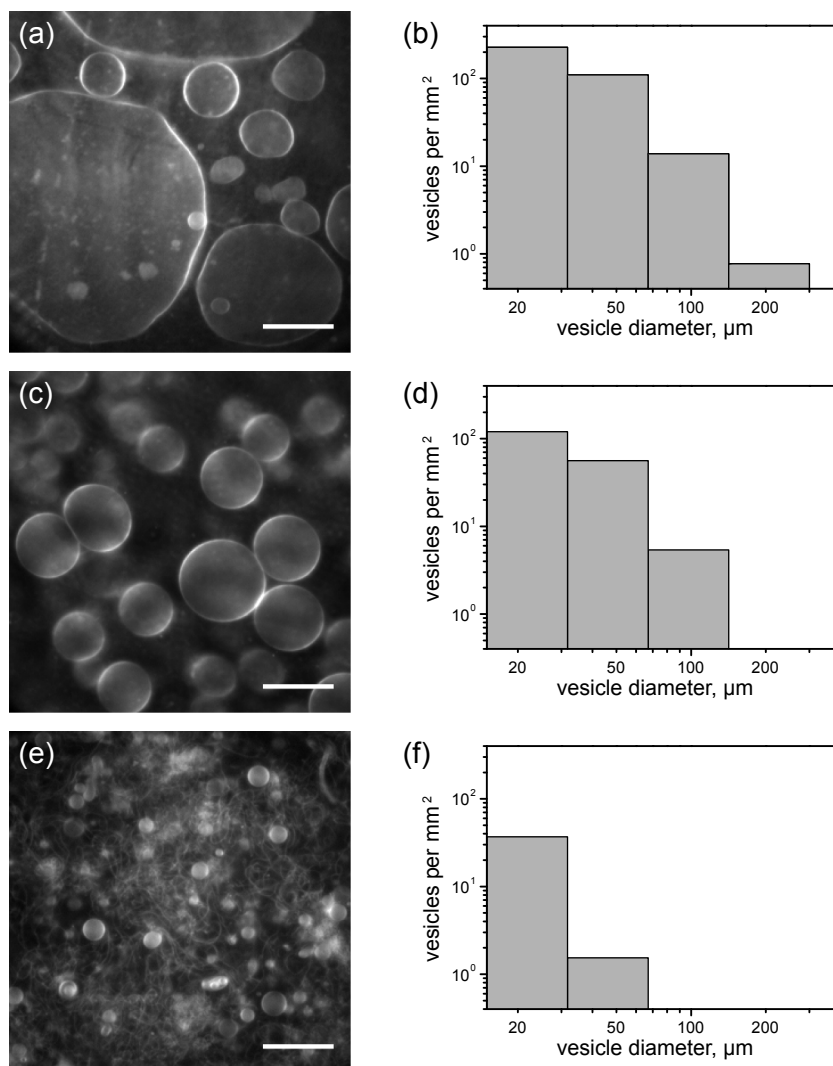


Figure 3.1: Fluorescence microscopy images of cationic GUVs (DOPC/DOTAP 95:5) grown on ITO-coated coverslips and distributions of vesicle diameters demonstrating the effects of coverslip aging expressed in the number of times N the coverslips were previously used. (a, b) for $N = 0$ (as received from the producer), (c, d) for $N = 2$, and (e, f) for $N = 4$. Membrane fluorescent labeling: 0.1 mol% DiD. Scale bars: 50 μm .

This is an unexpected and remarkable finding, especially taking into account the extreme reliability of the electroformation technique when it is used to produce GUVs and SGUVs consisting of zwitterionic or anionic lipid mixtures, irrespectively of whether new or used ITO-coated coverslips are employed.

A pair of ITO-coated coverslips was used to carry out a set of electroformation experiments demonstrating this behavior, by contrasting the successful electroformation of SGUVs from zwitterionic DOPC and anionic DOPC/DOPS lipid mixtures to the lack of success in SGUV formation using the cationic lipid mixture of DOPC/DOTAP (see Figure 3.2). The already

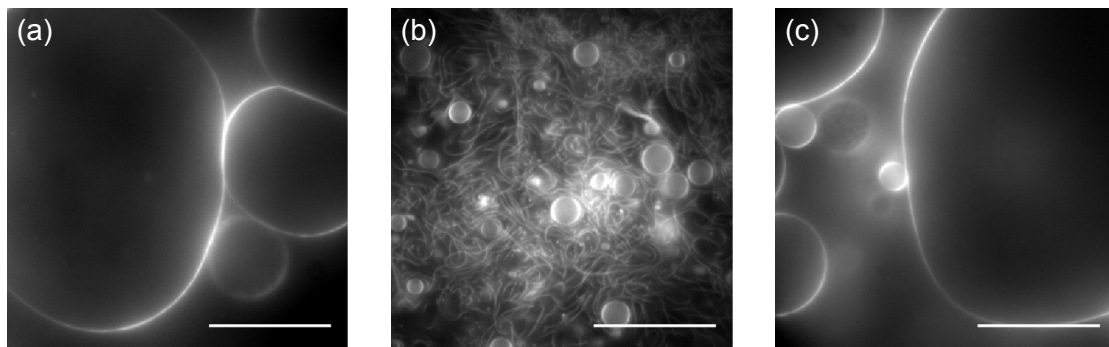


Figure 3.2: Fluorescent microscopy images of vesicles grown consecutively on the same pair of ITO-coated coverslips. (a) Zwitterionic GUVs consisting of DOPC, $N = 3$. (b) Cationic vesicles (DOPC/DOTAP 95:5), $N = 4$. (c) Anionic vesicles (DOPC/DOPS 95:5), $N = 5$. Membrane fluorescent labeling: 0.1 mol% DiD. Scale bars: 50 μm .

three times used ($N = 3$) pair of ITO-coated coverslips was employed in GUV electroformation with zwitterionic lipids (DOPC). As expected, SGUVs were effortlessly produced in this case (Figure 3.2(a)). The same pair of ITO-coated coverslips (for which now $N = 4$) was subsequently cleaned using the standard cleaning procedure and employed in electroformation with the cationic lipid mixture (DOPC/DOTAP 95:5). In this case, no SGUVs were found, and the few GUVs which could be observed were small and surrounded by tubular structures (Figure 3.2(b)). After yet another cleaning using the standard procedure, the ITO-coated coverslips were reused again ($N = 5$), this time for electroformation with an anionic lipid mixture (DOPC/DOPS 95:5), and SGUVs were again effortlessly formed in large amounts (Figure 3.2(c)).

3.1.3. Improved electroformation efficiency through mild annealing of the ITO coating

By serendipity, we found that the properties of ITO-coated coverslips previously used for production of lipid vesicles could be completely restored if, prior to electroformation, ITO-coated coverslips are annealed in air for ca. 20 min at 150 $^{\circ}\text{C}$. If this method is applied, cationic SGUVs can be reliably produced (Figure 3.3), and the amount of SGUVs with diameters $> 100 \mu\text{m}$ is even increased compared to the use of untreated new ITO-coated coverslips.

One should emphasize that the lipid ratios reported here are related to the original lipid mixture which was deposited on ITO-coated coverslips. It is presently beyond our technical capabilities to check whether the composition of electroformed vesicles is identical to that of the original lipid mixture. What is, however, clear from our previous experiments [121], is that the concentration of the cationic lipid in electroformed vesicles is at least correlated with that in the original lipid mixture.

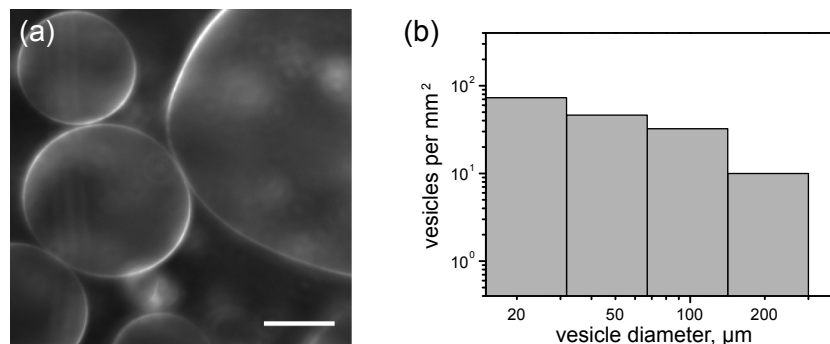


Figure 3.3: Fluorescence microscopy image (a) of cationic GUVs (DOPC/DOTAP 95:5) grown on ITO-coated coverslips and distribution of vesicle diameters (b) demonstrating the effect coverslip recovery after annealing: $N = 5$, but annealed in air for 20 min at 150 °C prior to electroformation. Membrane fluorescent labeling: 0.1 mol% DiD. Scale bar: 50 μm .

It should be emphasized that the effect is not limited to the DOPC/DOTAP 95:5 lipid mixture. The same effect is observed also for DOPC/DOTAP mixtures with the cationic DOTAP content from 2–10 mol%. At DOTAP concentrations of 1 mol% and below, SGUVs can be easily formed using the standard coverslip cleaning procedure. For DOTAP concentrations of 15 mol% and higher, we found that electroformation of GUVs with diameters larger than 20 μm is inhibited.

We also explored the behavior of a lipid mixture containing another cationic lipid, EDOPC, and found that essentially the same phenomenology is observed for DOPC/EDOPC lipid mixtures.

3.1.4. Surface properties of ITO investigated by AFM

Measurements described in this Section were performed in collaboration with Grzegorz Chwastek

Using AFM, we found that the aging effect observed in the form of the progressively deteriorating quality of electroformed cationic GUVs is accompanied by morphological changes of the surface of ITO-coated coverslips. We found that the AFM height images of new, as received from the producer, coverslips show small (50–100 nm in diameter, ca. 2 nm deep) pores with a typical surface density of 20–40 μm^{-2} (Figure 3.4(a)). Also, the pores can be clearly seen in the surface height histogram (Figure 3.4(b)) contributing to a pronounced shoulder in the range of -2.5 nm to -1 nm. Interestingly, after repeated use of the coverslip for vesicle electroformation, these pores virtually completely disappear for $N > 3$ (Figure 3.4(c,d)). Remarkably, annealing-induced recovery of the ability of ITO-coated coverslips to produce cationic SGUVs was reflected in the ITO surface topography and accompanied by reappearance of pores with the same parameters as for the new ITO-coated coverslips (Figure

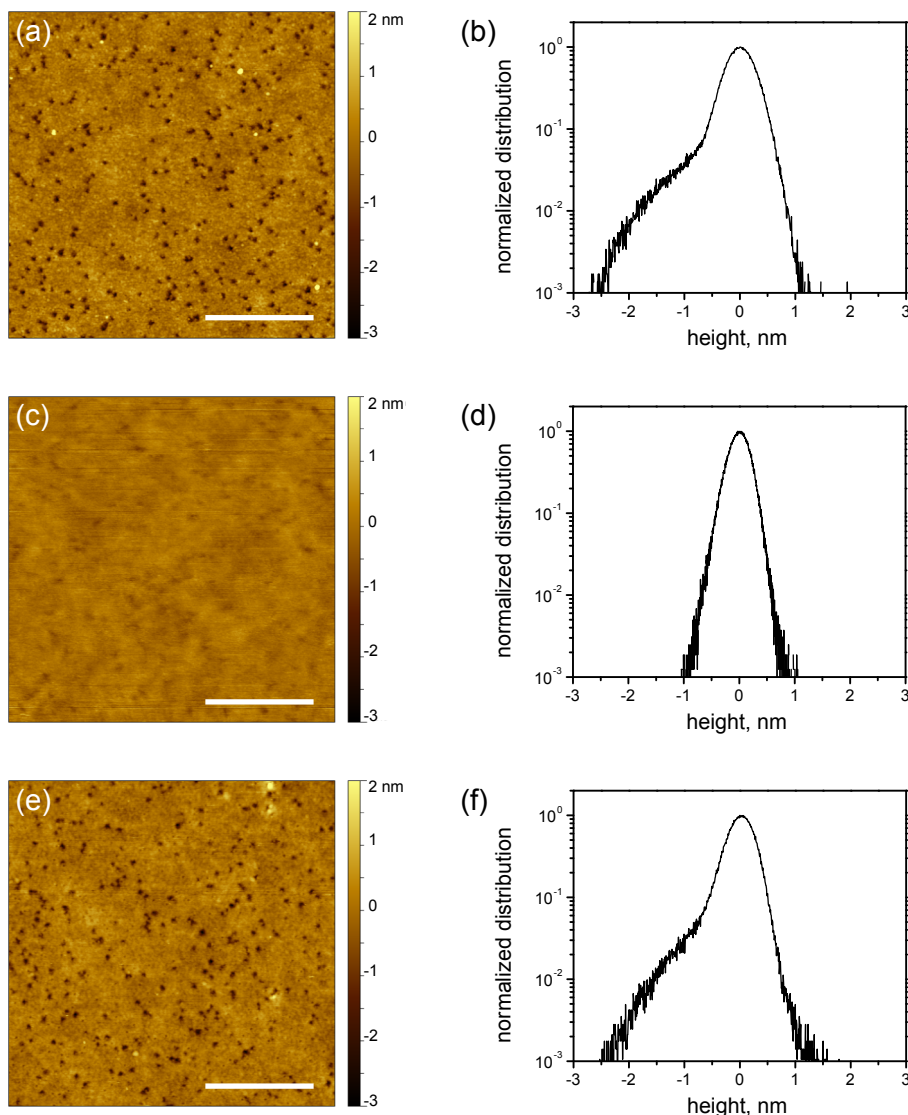


Figure 3.4: Surface topography of ITO-coated coverslips determined by atomic force microscopy (AFM height images) and the respective height histograms demonstrating the effects of ITO surface aging expressed in terms of the number of times N the coverslip was used in electroformation and recovery after annealing: $N = 0$ (as received from the producer) (a, b); $N = 4$ (c, d); $N = 5$, but annealed in air for 20 min at 150 °C prior to AFM measurements (e, f). Scale bars: 1 μm .

3.4(e,f)).

One can speculate that there might be a direct connection between the quality of electroformed cationic GUVs and the surface properties of the ITO layer reflected in its surface topography. Indeed, it has been shown previously [125, 126] that the ITO surface is prone to develop a carbon-rich contamination layer that cannot be entirely removed by organic solvents [126]. Oxidative treatment of the ITO surface removes the contamination and substantially increases the work function of the ITO surface [125, 126]. Annealing in air might play a role

of a mild oxidative surface treatment, thereby restoring the properties of the ITO layer. Nevertheless, the exact mechanisms of both the effect of aging of the ITO surface on the growth of cationic lipid vesicles and its reversal by annealing in air, still remain open questions which are outside the scope of this Thesis.

3.2. Membrane surface viscosity determination

The membrane surface viscosity is an important parameter influencing the behavior of colloids or macromolecules bound to a lipid membrane. For this reason, experimental methods to determine the membrane surface viscosity are often based on the analysis of the dynamic behavior of membrane-bound particles. With the development of the Saffman-Delbrück theory for the diffusion of small membrane inclusions in the 1970s [47, 48] (see Section 1.2.2) the possibility arose to determine the membrane surface viscosity from diffusion coefficients of membrane proteins with known size [127], and this approach is used to the present day [128]. A variety of other experimental methods exist, such as membrane tether formation from lipid vesicles [50, 129], the analysis of diffusion coefficients of lipid membrane domains [54] or their shape fluctuations [130], and the so-called falling ball viscosimetry [18][131][132].

However, in relation to the importance of the membrane surface viscosity for dynamic processes the data available in the literature are rather sparse. To the best of the author's knowledge, no value for the surface viscosity for a commonly used DOPC membrane, let alone the specific DOPC/DOTAP lipid mixture, has been published before the work on this Thesis had started. The closest composition previously studied, is an anionic DOPC/DOPG 3:1 membrane with the reported surface viscosity of 3×10^{-10} Pa s m [128].

In order to determine the membrane surface viscosity of the DOPC/DOTAP membranes used in this Thesis, an experimental approach based on the measurement of the translational diffusion of small (10–50 nm radius) anionic polystyrene beads adsorbed to a freestanding cationic lipid membrane, was developed.

In this Section this method and its application to the determination of the surface viscosity of freestanding DOPC/DOTAP bilayers is described in detail.

3.2.1. Anionic polystyrene beads as probes of the membrane surface viscosity

Carboxylated fluorescent polystyrene beads with three different radii – 10, 20, and 50 nm – in dd-H₂O at a concentration not exceeding 10^{-11} M were injected into a chamber containing electroformed DOPC/DOTAP SGUVs. 300 μ l of the bead solution was injected into this chamber using a syringe pump at an injection rate of 10 μ l/min, to ensure the integrity of the surface-attached vesicles. After injection the cationic beads attached to the lipid membrane of the vesicles, mediated by the electrostatic forces between the oppositely charged colloids and membrane. Particles were bound to the membrane at a typical surface density of 0.05

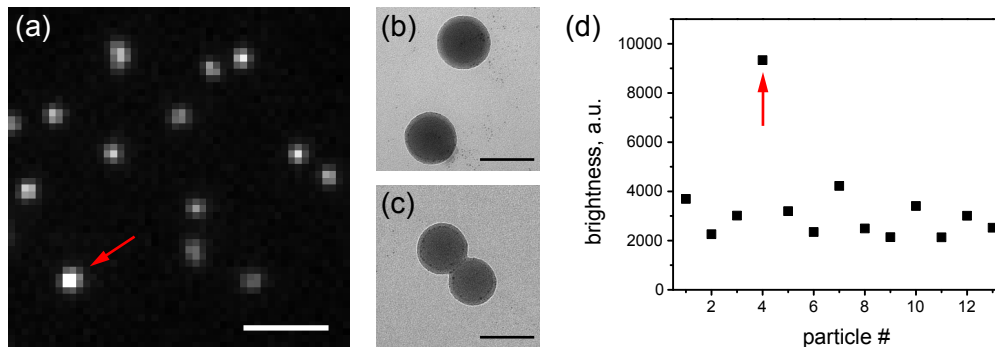


Figure 3.5: (a) Fluorescence image of anionic fluorescent polystyrene beads (50 nm radius) adsorbed to the upper pole region of an SGUV membrane (DOPC/DOTAP 99:1). Scale bar: 5 μm . (b) TEM image of polystyrene beads with 50 nm radius. (c) TEM image of clustered polystyrene beads as obtained by the producer. Scale bar: 100 nm. (d) Brightness of the tracked fluorescent beads in image (a). Particle number 4 is indicated by the red arrow in (a) and shows an elevated brightness about three fold higher than the 12 other particles. Clustered particles are removed from the data analysis if their brightness is at least 50 % higher than the average brightness of the majority of particles.

μm^{-2} and exercised two-dimensional Brownian motion, which could be recorded by observing the top pole of the surface-attached SGUVs (see Section 2.4.8). Beads on a membrane area of approximately $300 \mu\text{m}^2$ (disc-like with $\sim 20 \mu\text{m}$ diameter) could be observed in focus. The vesicles did not exhibit detectable shape undulations and observed membrane area did not change its position over the course of the experiments.

A fluorescence microscopy image of 50 nm radius beads attached to a 99:1 DOPC:DOTAP membrane is shown in Figure 3.5(a). There, all particles show a very similar brightness as expected for beads of the same kind and size, except for one particularly bright particle highlighted by the red arrow. The bright particle, however, is a result of a production defect occasionally found in every bead sample. Transmission electron microscopy (TEM) of dried bead solution reveals that most beads are single and of homogeneous size. An example of single 50 nm radius beads is shown in Figure 3.5(b). But as depicted in Figure 3.5(c), clustered beads such as a dimer that possesses a permanent neck-like link are present as well.

To remove the effect of the coagulated beads from the diffusion analysis, the particle brightness obtained as the integrated intensity I_0 over the ROI which was used to track the individual particles (see Section 2.4.1) is evaluated. If the intensity of a particle is higher by more than a factor of 1.5 compared to the average intensity of the majority of particles, the particle trajectory is discarded from further analysis. Figure 3.5(d) shows the intensities obtained from the particles of the image in Figure 3.5(a). The bright particle is clearly identified as particle # 4 and shows an intensity about three times higher than the average intensity of the 12 other beads.

The lateral displacements were calculated from all particle trajectories which passed the brightness filtering and combined to construct a time dependent MSD for every single vesicle.

The individual points of the MSD were calculated from at least 5000 displacement steps. For every bead size and membrane composition a minimum of five vesicles were investigated and the mean lateral diffusion coefficient D was calculated as described in Section 2.4.5.

One should stress that no clustering due to mutual attraction of membrane adsorbed beads was observed under the described experimental conditions. However, the formation of ordered domain-like structures due to membrane-mediated mutual attraction of membrane adsorbed beads could be observed when significantly higher – approximately 1000 fold – bead concentrations were injected into the vesicle chamber [133]. This phenomenon has also been observed in previous reports [119, 134, 135] but is still not understood in full detail. The absence of clustering effects in the present work is important, as only the mobility of single beads is of interest in determining the membrane surface viscosity.

3.2.2. Viscosity of water

Knowing the membrane inclusion size – the radius of the membrane-adsorbed beads – the last system parameter needed to determine the membrane surface viscosity, is the viscosity of the surrounding medium μ . On both sides, the freestanding lipid bilayer is surrounded by deionized water. Its viscosity is temperature-dependent and can be calculated according to an empirical formula derived in [136]:

$$\log\left(\frac{\mu(T_C)}{\mu(20\text{ }^\circ\text{C})}\right) = \frac{20 - T_C}{T_C + 96} [1.2364 - 1.37 \times 10^{-3}(20 - T_C) + 4.7 \times 10^{-6}(20 - T_C)^2], \quad (3.1)$$

with the temperature T_C in $^\circ\text{C}$ and the viscosity of water at $20\text{ }^\circ\text{C}$, $\mu(20\text{ }^\circ\text{C}) = 1.002\text{ mPa s}$. At the temperature $T_C = 24\text{ }^\circ\text{C}$ measured at the sample, Equation (3.1) yields $\mu = 0.91\text{ mPa s}$, the value used in the further analysis.

3.2.3. Membrane surface viscosity of DOPC/DOTAP membranes

SGUVs formed from a lipid mixture of DOPC with different fractions of cationic DOTAP C_{DOTAP} , ranging from 1 mol% to 7 mol% were probed using anionic polystyrene beads with the radius $a = 10\text{ nm}$. The resulting translational diffusion coefficients shown in Figure 3.6(a) are virtually independent of the DOTAP fraction in the DOPC membrane. This means that the membrane surface viscosity is constant within the range of membrane compositions investigated here and in the following parts of this Thesis. On the other hand, one finds a clear dependence of the translational diffusion coefficient of beads on their radius at a fixed DOTAP concentration, as shown in Figure 3.6(b).

The translational diffusion coefficient of a particle with the characteristic radius a bound to a membrane with surface viscosity η and surrounded by water with viscosity μ is essentially independent of the particle's three-dimensional shape and presence or absence of protrusions

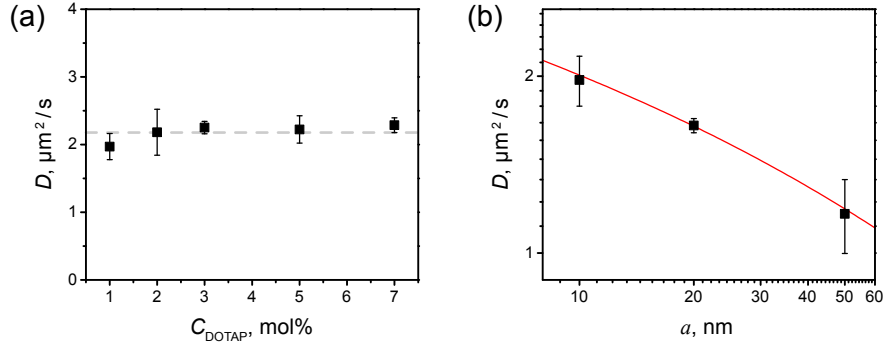


Figure 3.6: Translational diffusion of anionic polystyrene beads electrostatically bound to a cationic DOPC/DOTAP membrane. (a) Translational diffusion coefficients of 10 nm radius beads adsorbed to DOPC membranes with different cationic DOTAP content C_{DOTAP} , ranging from 1 mol% to 7 mol%. The gray dashed line represents the mean value of the obtained diffusion coefficients. (b) Translational diffusion coefficients of polystyrene beads with radii $a = 10$ nm, 20 nm and 50 nm adsorbed to a freestanding DOPC/DOTAP 99:1 membrane. The red curve represents the fit to the HPW model for the translational diffusion of membrane inclusions according to Equation (1.16), yielding a membrane surface viscosity $\eta = (5.9 \pm 0.2) \times 10^{-10}$ Pa s m. Experiments were carried out at the temperature of 24 °C.

into the bulk medium, if the membrane is viscous enough [137, 138]. The condition of a viscous enough membrane is met if the ratio $\eta/(a\mu) > 4$ [138]. This means that for membrane bound particles of a characteristic radius not exceeding 50 nm a membrane surface viscosity η larger than 1.8×10^{-10} Pa s m is sufficient to neglect the exact particle shape. Following this argument, it is possible to treat the spherical beads as cylindrical membrane inclusions and analyze their diffusion using the HPW theory [53] and the closed-form approximation thereof [54]. Making use of Equation (1.16), the HPW theory is applied to the bead size-dependent diffusion coefficients, yielding the membrane surface viscosity $\eta = (5.9 \pm 0.2) \times 10^{-10}$ Pa s m. The corresponding fit to the experimental data is plotted as a red curve in Figure 3.6(b). This result is in fair agreement with a previous study, reporting $\eta = 3 \times 10^{-10}$ Pa s m [128] for an anionic DOPC/DOPG 3:1 membrane consisting of lipids with similar hydrocarbon chains.

3.3. Conclusion

To conclude, we developed a method which allows for reliable and efficient electroformation of cationic SGUVs on ITO-coated coverslips. It consists in mild annealing of the ITO-coated surface coverslips in air at 150 °C before the standard vesicle electroformation procedure. The resulting cationic SGUVs with radii larger than 50 μm present a perfect experimental platform to study the interaction of colloidal particles and (bio)macromolecules with a freestanding bilayer using optical wide-field fluorescence microscopy. The SGUVs do not exhibit detectable thermal shape undulations and the observable membrane stays in the focus position over the course of tens of minutes. The membrane area on the top pole of the dome-like SGUVs, which

can be simultaneously observed in focus, is approximately 300–700 μm^2 large. This region of interest is situated at a distance of at least 50 μm to any surface. This distance is much larger than the Saffman–Delbrück length in this system, which allows one to consider the membrane as effectively freestanding.

The use of the SGUV as a model freestanding lipid bilayer allowed us to determine the surface viscosity of DOPC/DOTAP membranes. In particular, the analysis of the translational diffusion coefficients of small (10, 20, 50 nm) membrane-attached anionic polystyrene beads using the HPW PS expression has shown that the surface viscosity of DOPC/DOTAP membranes with $C_{\text{DOTAP}} = 1\text{--}7$ mol% is independent of the DOTAP concentration and equals $\eta = (5.9 \pm 0.2) \times 10^{-10}$ Pa s m.

Thus, our experiments with DNA macromolecules adsorbed to fluid freestanding cationic membranes show a change in DNA conformation from a 2D random coil to a compact globule depending on the fraction of cationic lipids in the bilayer and the length of the DNA. The globule state is favored for high cationic lipid concentrations and long DNA contour lengths. On the contrary, at low cationic lipid concentrations the majority of the membrane-adsorbed DNA molecules is in a random coil conformation. In the latter case, the DNA–membrane interactions are apparently too weak to facilitate a DNA coil–globule transition. At cationic lipid concentrations close to those where all adsorbed DNA molecules collapse to globules, partially collapsed DNA molecules are observed for long DNA molecules of 48.5 kbp and 20 kbp. In the observed events of membrane-mediated DNA coil–globule transition we found that the DNA collapse is a fast process with a compaction rate of 124 ± 46 kbp/s. Fluorescence microscopy experiments clearly show that the size of the membrane-bound DNA globules does not exceed 500 nm. By relating the translational diffusion coefficients of completely collapsed DNA globules to the radius of a membrane inclusion an estimate of the DNA globule size was obtained and found to be 250–350 nm at DOPC membranes containing 1 mol% DOTAP and 130–200 nm for 7 mol% DOTAP, indicating a stronger compaction for higher charge densities in the membrane.

Additional experiments with freestanding cationic membranes in the gel state and supported cationic lipid membranes with gel–fluid coexistence suggest that the DNA collapse on a freestanding fluid cationic membrane may be initiated by a local lipid segregation in the membrane and accompanied by local membrane deformations, which stabilize the compact DNA globule.

Behavior of DNA Macromolecules on Cationic Lipid Membranes: Effects of DNA–Membrane Interaction Strength and Membrane Properties

4.1. DNA on fluid freestanding cationic membranes

Understanding the interaction of polyelectrolytes with oppositely charged lipid membranes is an important issue of soft matter physics, which provides an insight into mechanisms of interactions of biological macromolecules with cell membranes. Although the question has been addressed during the past decade both experimentally and theoretically [6, 139], the understanding is far from complete, and some important unresolved questions, including the effects of the membrane local curvature and bending elasticity, remain to be addressed. A perfect model polymer to study electrostatic polyelectrolyte-membrane interactions is double-stranded DNA whose length and structure can be precisely controlled using the modern biotechnological methods.

These advantages were used in a seminal work by Maier and Rädler [8, 9] where it was demonstrated that DNA molecules adsorbed at a fluid cationic lipid bilayer on a flat support assume a 2D random coil conformation and exercise translational Brownian motion. These results have since become a textbook example of polymer coil dynamics in 2D [140].

A completely different picture is observed when double-stranded DNA interacts with small (20–100 nm) cationic liposomes: In this case DNA molecules wrap around liposomes and eventually form densely packed liquid crystalline DNA-lipid globules [141] with the typical size of 100–200 nm [142, 143]. Formation of DNA-lipid globules is an example of a more general phenomenon known as DNA condensation [144, 145]. DNA condensation by cationic liposomes has attracted particular attention in view of its potential use in gene therapy [146] and importance for understanding the prebiotic chemistry [143].

The striking contrast between the behavior of DNA at flat supported cationic lipid bilayers and at strongly curved small cationic liposomes naturally leads to the question of what kind of behavior can be expected upon interaction of DNA with freestanding cationic lipid bilayers, which, in contrast to solid-supported membranes, can locally deform in response to an external force.

Recent experiments on interaction of DNA with cationic membranes supported on structured surfaces demonstrated the importance of the local bilayer curvature in DNA-membrane interactions [147]. Obviously, freestanding bilayers, capable of bending locally in response to an external perturbation, may show new unexpected ways of interaction with charged semiflexible DNA molecules.

Surprisingly, very little is known about interaction of DNA with freestanding cationic lipid bilayers. The only study in this direction was carried out in a series of works [117, 118]. The experimental approach used in these works could not, however, provide any information on conformation and dynamics of single DNA molecules.

4.1.1. Experimental details

Freestanding fluid cationic membranes were modeled by SGUVs consisting of DOPC and different cationic DOTAP fractions ranging from 1 to 10 mol%. The membrane was fluorescently labeled with 0.1 mol% DiD. Vesicles were electroformed in dd-H₂O according to the procedure described in [148] and Sections 2.2.2 and 3.1. As mentioned above, the vesicles did not exhibit noticeable thermal shape undulations.

Double-stranded DNA was fluorescently labeled with YOYO-1 (see Section 2.3.1) and diluted in dd-H₂O to a concentration of 10^{-7} M. 300 μ l of this solution of DNA fragments with lengths of either 5 kbp, 10 kbp and 20 kbp, or full length linear λ -DNA (48.512 kbp) were injected at a rate of 10 μ l/min into the SGUV chamber. This injection of a dilute DNA solution left the DNA molecules at a considerable distance to the vesicles attached at the bottom coverslip. DNA molecules diffused freely in the solution surrounding the SGUVs and finally could reach the SGUV surface. After the injection, DNA was left to incubate with the cationic SGUVs for at least one hour.

Following the incubation period, a typical particle density of membrane-adsorbed DNA molecules of $0.01 \mu\text{m}^{-2}$ was obtained. Fluorescent images were acquired at a rate of 10 fps with the exposure time of 50 ms. Several movies, each consisting of a few thousand frames, were recorded on the top pole of a single vesicle and at least ten individual vesicles were investigated for every DNA length and membrane composition.

DNA molecules were tracked and translational diffusion coefficients were obtained by the methods described in Section 2.4.

Control experiments on mica-supported lipid membranes were carried out using the

DOPC/DOTAP 90:10 membrane composition. SLBs on mica were formed from SUVs, as described in Section 2.2.1. Fluorescently labeled λ -DNA in dd-H₂O (10^{-7} M) was added after bilayer formation and allowed to interact with the cationic supported membrane for approximately ten minutes, after which repetitive and careful washing with dd-H₂O was applied to remove unbound DNA from the solution. Afterwards, the sample was left to equilibrate for several hours.

All experiments were carried out at the room temperature of 24 °C.

4.1.2. DNA condensation on freestanding fluid cationic lipid bilayers

One of the objectives of this Thesis is to compare the behavior of DNA molecules interacting with a freestanding fluid cationic lipid membrane with the previously reported behavior of DNA molecules on a supported fluid cationic lipid membrane [8, 9]. Therefore, as a starting point the experimental situation of DNA molecules on a supported membrane was recreated with an approach similar to that described in [8, 9]. In those control experiments, after attaching to supported cationic lipid bilayers, DNA molecules assumed a 2D random coil conformation (Figure 4.1(a)) and exercised translational Brownian motion, in agreement with the previous reports [8, 9].

In experiments on DNA interaction with freestanding cationic membranes, some minutes after injection of DNA to the chamber containing cationic SGUVs, a fraction of DNA molecules attached to the vesicle surface, whereas the rest of DNA stayed in solution. Attachment of DNA to SGUVs never affected the conformation or behavior of the vesicles. This is in contrast with observations [117, 118], where vesicle destabilization was induced by local application of a highly concentrated DNA solution, which is obviously not the case in our experiments.

DNA molecules not interacting with cationic membranes and remaining in the surrounding fluid always showed random coil conformations (Figure 4.1(b)). Their translational diffusion

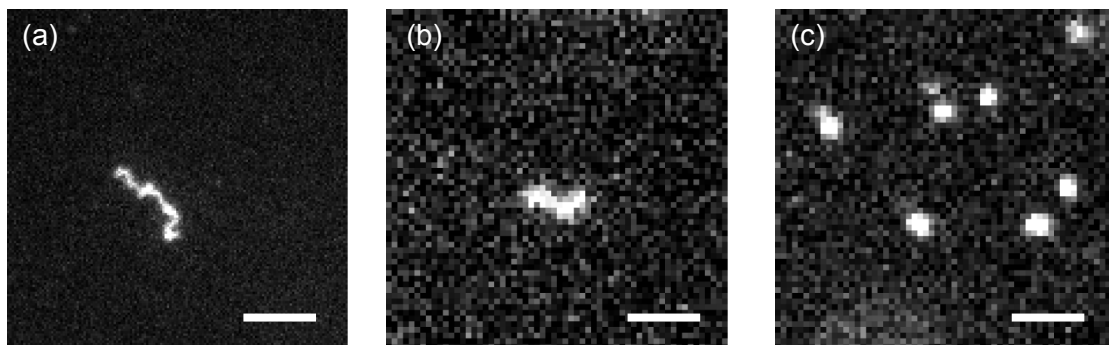


Figure 4.1: Fluorescence microscopy images of λ -DNA molecules: (a) adsorbed on a supported fluid cationic lipid bilayer, (b) free in water surrounding cationic GUVs, (c) adsorbed on a freestanding fluid cationic lipid bilayer (SGUV). Membrane composition DOPC/DOTAP 90:10. Scale bars: 5 μ m.

coefficients determined from single particle tracking were a factor of 1.6–1.9 lower than those of DNA in the presence of 100 mM NaCl [73], which is expected due to an increase in the polyelectrolyte persistence length at low ionic strengths [74] resulting in a larger hydrodynamic radius.

Compared to the adsorption of DNA molecules to a supported cationic bilayer, a strikingly different behavior is observed for DNA molecules adhering to freestanding cationic membranes. As shown in Figure 4.1(c), the membrane-attached DNA molecules are much more compact or collapsed.

In order to investigate this new and surprising phenomenon, a systematic study was carried out, using DNA molecules of different lengths in the range of 5–48.5 kbp and freestanding membrane compositions with different cationic DOTAP content in the range of 1–7 mol%. We found that for very long λ -DNA molecules (45.8 kbp) at a very low DOTAP concentration of 1 mol% the majority of DNA molecules exhibits a 2D random coil conformation and only some DNA molecules appear compacted (Figure 4.2(a)). This picture changed significantly already for membranes containing 2 mol% of DOTAP. Here, most of the λ -DNA molecules are compacted and only a few show a partially collapsed conformation, but almost none are found in a random coil conformation (Figure 4.2(b)). After attachment to membranes with a DOTAP concentration between 3 mol% and 7 mol% all membrane-bound λ -DNA molecules appear as compact globules (Figure 4.2(c)).

When investigating shorter DNA fragments of 20 kbp length, the critical DOTAP concentration at which almost all membrane-bound DNA molecules are compacted shifts to a higher value. In contrast to λ -DNA, a large amount of 20 kbp membrane-attached DNA molecules remains in the random coil or only partially collapsed conformation and only some are fully collapsed at 2 mol% of DOTAP (Figure 4.2(d)). Again, at higher DOTAP concentrations all membrane-bound 20 kbp DNA molecules are compacted to globules (Figure 4.2(e)).

This trend of a higher percentage of DOTAP required to compact membrane-bound DNA continues if the DNA length is shortened further. At 3 mol% DOTAP, still a large fraction of 10 kbp DNA molecules appear as random coils (Figure 4.2(f)), but all 10 kbp DNA molecules are collapsed at a membrane with 7 mol% DOTAP (Figure 4.2(g)). For 5 kbp DNA, some random coils are still found for the DOTAP content of 7 mol% in the membrane (Figure 4.2(h)), the particle in the the lower left corner of the image shows an elongated shape (coil), the two particles in the middle of the image do not show any shape anisotropy (globule).

The phase diagram constructed on the basis of the experimental data clearly illustrates this tendency. DNA collapse is especially favored at high concentrations of the cationic lipid *and* for long DNA fragments, whereas coexistence of globules and partially collapsed or essentially non-collapsed DNA molecules is observed at low DOTAP concentrations and/or for short DNA fragments (Figure 4.3).

Storing the samples at room temperature for 18 h did not lead to noticeable changes in

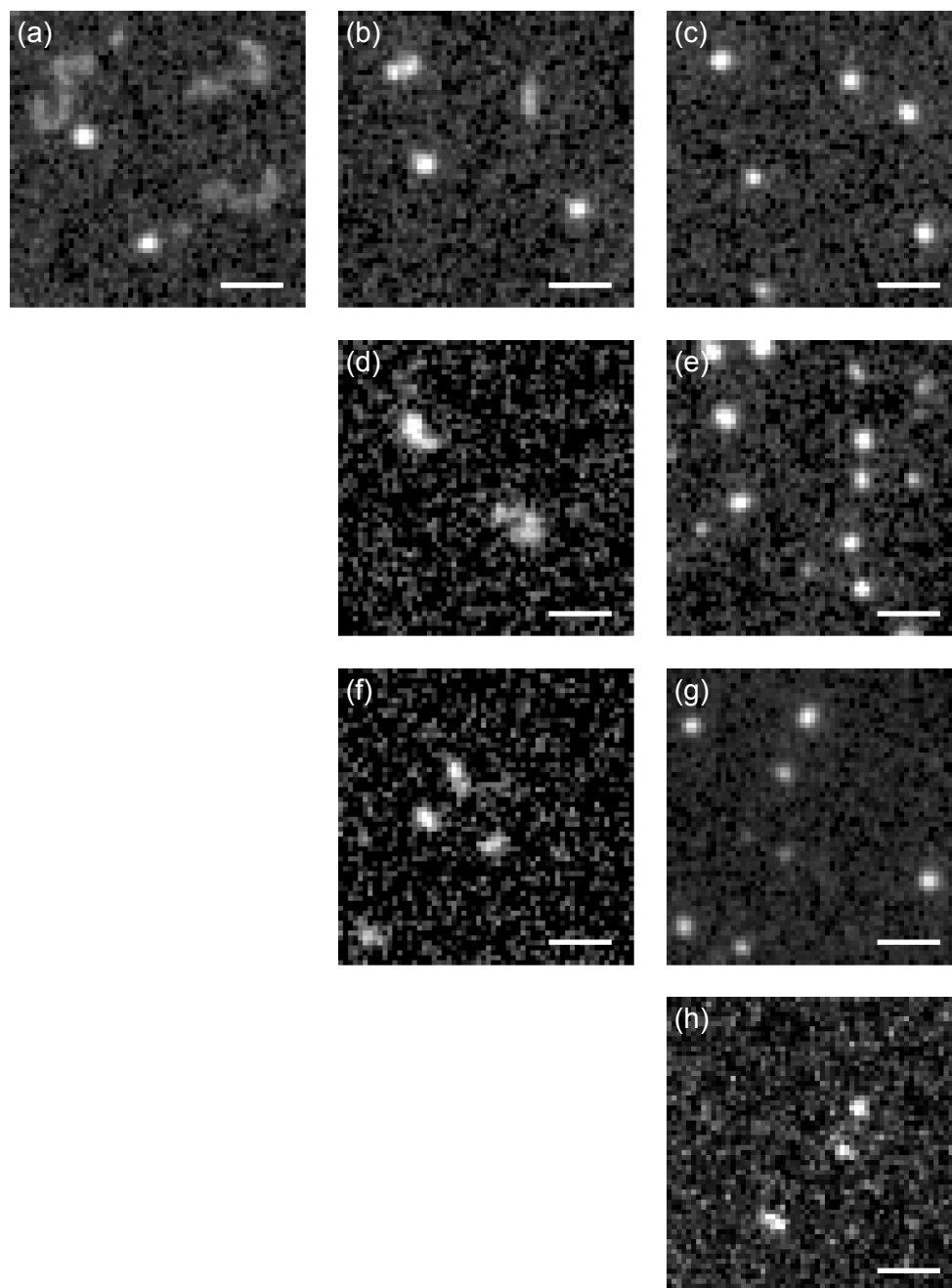


Figure 4.2: Fluorescence microscopy images of DNA molecules of different lengths adsorbed free-standing fluid cationic bilayers (SGUVs) with different cationic DOTAP content. (a)–(c) λ -DNA at DOPC membranes with: (a) 1 mol%, (b) 2 mol% and (c) 7 mol% DOTAP. (d)–(e) 20 kbp DNA at DOPC membranes with: (d) 2 mol% and (e) 7 mol% DOTAP. (f)–(g) 10 kbp DNA at DOPC membranes with: (f) 3 mol% and (g) 7 mol% DOTAP. (h) 5 kbp DNA at a DOPC membranes with 7 mol% DOTAP. Scale bars: 5 μ m.

both the distribution of conformations and area density of membrane-bound DNA molecules, which means that the phase diagram reflects the equilibrium situation. Also, control ex-

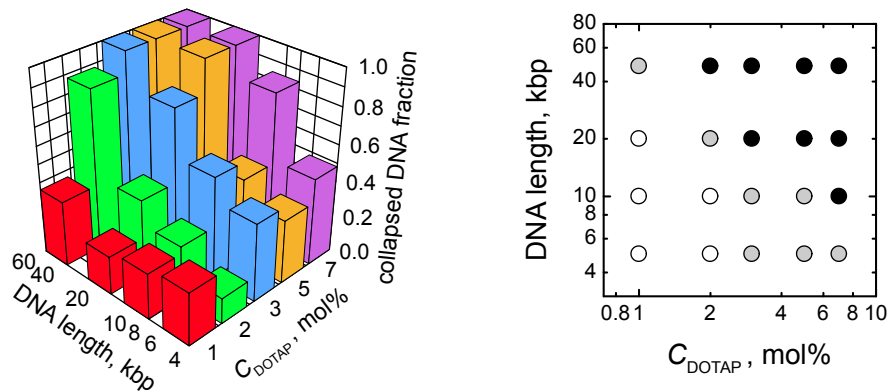


Figure 4.3: Phase diagram of coil–globule transition of DNA molecules at freestanding cationic lipid (DOPC/DOTAP) bilayers. In the right-hand panel, the fraction of condensed DNA is encoded by the shading of symbols: 0–0.35 (white), 0.35–0.65 (gray), and 0.65–1.0 (black)

periments with a reduced DNA labeling density of 0.02 dye/bp did not affect the observed phenomenology.

Several observations of DNA globules attached to cationic GUVs have been reported previously [119, 149, 150]. In these studies, in contrast to our investigation, DNA condensation in the bulk media surrounding the GUVs was possible, and therefore these results were interpreted by their authors in terms of attachment of a preformed DNA globule to the membrane surface.

The fact that in our experiments no DNA globules are observed in the fluid surrounding GUVs suggests that the DNA collapse takes place after a DNA molecule attaches to the membrane. The proof of this scenario can, of course, only be provided by a direct observation of the collapse event. Indeed, a number of collapse events of single DNA molecules initially attached in a random coil conformation to the vesicle surface were observed and documented, as exemplified in Figure 4.4 for a full length λ -DNA molecule and Figure 4.5 for a 20 kbp DNA molecule. There, a single λ -DNA molecule attached to a GUV in an extended conformation and radius of gyration $R_g \approx 2.3 \mu\text{m}$ suddenly collapses into a subresolution-sized globule with $R_g \approx 0.3 \mu\text{m}$, the collapse event taking less than 0.5 s (Figure 4.4(e)). In case of a 20 kbp DNA molecule the collapse from a random coil with $R_g \approx 1.1 \mu\text{m}$ to the subresolution-sized globule takes less than 0.1 s (Figure 4.5(e)). The collapsed DNA globules stay attached to the vesicle membrane. The mobility of the membrane adsorbed DNA molecules increases significantly after the collapse, as is evident from the molecule’s trajectory (Figure 4.4(f) and Figure 4.5(f) before and after the collapse event.

In all experiments, immediately upon attachment to the membrane, DNA molecules first assumed a 2D random coil conformation. In this extended conformation, the size of DNA molecules is characterized by the radius of gyration R_g which can be determined from the fluorescent images. For the shortest DNA fragments of 5 kbp one finds $R_g = 0.48 \pm 0.04 \mu\text{m}$

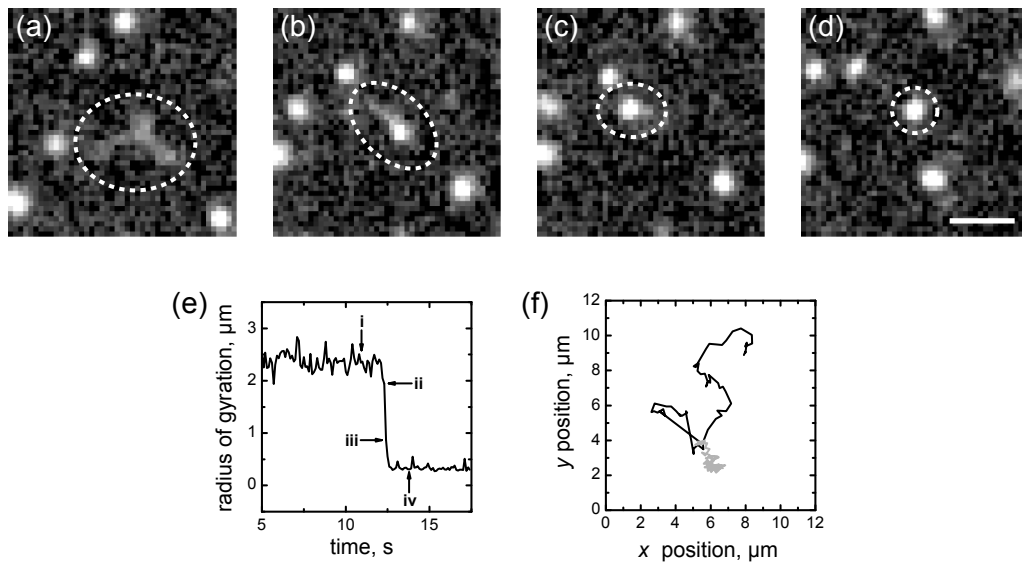


Figure 4.4: (a)–(d) Fluorescence microscopy images showing the collapse of a λ -DNA molecule bound to a freestanding cationic lipid membrane. (a) $t = 10.9$ s, (b) $t = 12.3$ s, (c) $t = 12.4$ s, (d) $t = 13.8$ s. (e) Time dependence of the two-dimensional radius of gyration of the DNA molecule; arrows i, ii, iii, and iv correspond to images (a)–(d). (f) Brownian motion trajectory of the DNA molecule before (gray) and after (black) the collapse. Bilayer composition: DOPC/DOTAP 90:10. Scale bar: $5 \mu\text{m}$.

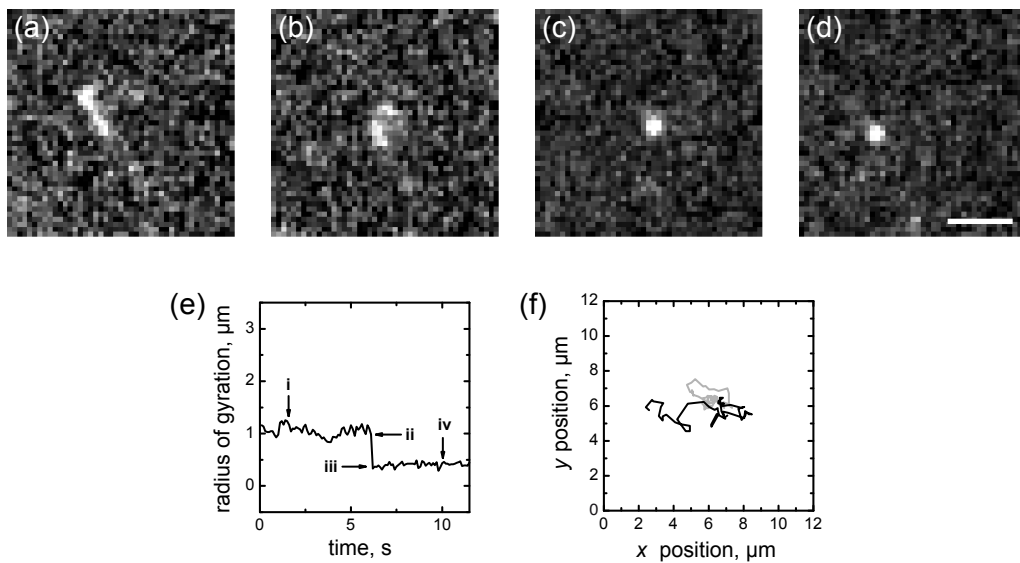


Figure 4.5: (a)–(d) Fluorescence microscopy images showing the collapse of a 20 kbp DNA molecule bound to a freestanding cationic lipid membrane. (a) $t = 1.5$ s, (b) $t = 6.2$ s, (c) $t = 6.3$ s, (d) $t = 10$ s. (e) Time dependence of the two-dimensional radius of gyration of the DNA molecule; arrows i, ii, iii, and iv correspond to images (a)–(d). (f) Brownian motion trajectory of the DNA molecule before (gray) and after (black) the collapse. Bilayer composition: DOPC/DOTAP 97:3. Scale bar: $5 \mu\text{m}$.

and for the longest DNA, λ -DNA, $R_g = 1.84 \pm 0.22 \mu\text{m}$. Only after staying for some time as a 2D random coil, DNA molecules could collapse into a tightly packed globule. All observed collapse events took place typically within ≤ 100 s after a DNA molecule attached to the membrane.

The compaction rate in the observed membrane-mediated DNA coil–globule transitions was found to be 124 ± 46 kbp/s (8 events). Interestingly, when resolvable, the collapse was always initiated by the compaction in the region of the ends of the DNA chain. An initial compaction in the center region of the DNA chain was never observed. The same is true for the observed partially collapsed DNA molecules, which exhibited a compaction at one or both ends of the DNA molecule, but not in the center.

Interestingly, the membrane-mediated DNA coil–globule transition agrees with observations of DNA condensation under different conditions, where DNA molecules in solution were compacted by multivalent cations, basic proteins, cationic surfactants, small cationic liposomes, alcohol, and neutral crowding polymers [144, 145]. This DNA condensation in solution results in highly compact and regular structures such as toroids or rods. These structures are formed to minimize the free energy of the system with contributions from the DNA elasticity, the electrostatic interactions of the charged DNA phosphate groups and the hydration of the DNA molecule in the solvent medium.

More to that, the membrane-mediated DNA coil–globule transition in our experiments is in qualitative agreement with the mean-field theory for conformational transitions of flexible polyelectrolytes in bulk media [151]. This theory also predicts existence of stable, partially collapsed DNA molecules due to intrachain segregation [145, 152]. Furthermore, the DNA compaction rate observed in our experiments is in good agreement with the compaction rate of 55 kbp/s reported for DNA molecules in solution which were compacted by cationic surfactants [153].

The DNA coil–globule transition is observed on freestanding fluid cationic membranes but never observed for DNA molecules on a fluid supported bilayer with the identical lipid composition. At the same time, theoretical studies of polyelectrolyte interaction with an inflexible flat charged membrane (see, e.g., [154, 155, 156]) do not predict formation of a polymer globule. This allows us to make a conclusion that the local membrane deformation due to interaction with the polyelectrolyte macromolecule [157] and/or local lipid segregation [158] is essential for DNA condensation at freestanding lipid bilayers.

4.1.3. Diffusion of DNA globules

The observed membrane-mediated DNA coil–globule transition poses the question of the degree of compaction of the globule. Clearly, the DNA globules have a size smaller or equal to the resolution of optical fluorescence wide-field microscopy. Unfortunately, it appeared to

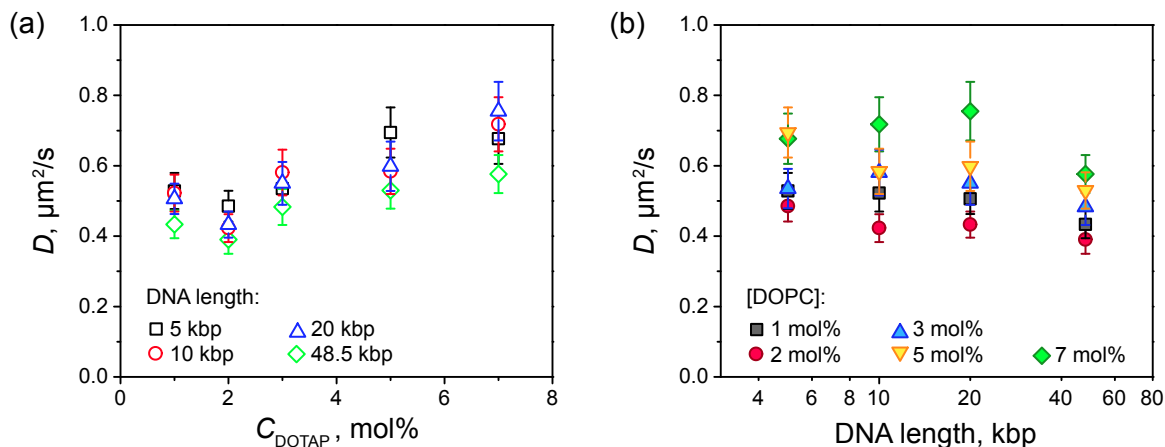


Figure 4.6: Translational diffusion coefficients of DNA globules bound to DOPC/DOTAP SGUVs as a function of concentration of the cationic lipid for different DNA lengths: 5 kbp, 10 kbp, 20 kbp, 48.5 kbp (a) and DNA length for different DOTAP concentrations: 1 mol%, 2 mol%, 3 mol%, 5 mol%, 7 mol% (b).

be impractical to use high resolution techniques such as atomic force microscopy (AFM) or transmission electron microscopy (TEM) on the SGUV samples, as for both techniques the bursting of SGUVs with previously adsorbed DNA molecules and adhering the membrane to a substrate is necessary. In a combined fluorescence microscopy and AFM setup, DNA globules can be localized using the fluorescent labeling, but the AFM investigation failed because the DNA globules were dragged along by the cantilever even in the tapping mode. TEM experiments, on the other hand, were difficult to interpret, most likely because after bursting the vesicle with adsorbed collapsed DNA, the DNA globules were efficiently shielded by a membrane layer from the environment, so that negative staining with uranyl acetate appeared to be inefficient.

An alternative to estimate the DNA globule sizes presents itself by the indirect method of relating the size of the DNA globules to their mobility manifested in their translational Brownian motion on the membrane.

In the experiments with membrane-adsorbed polystyrene beads described in Section 3.2 the membrane viscosity $\eta = (5.9 \pm 0.2) \times 10^{-10}$ Pa s m was found for freestanding cationic DOPC/DOTAP membranes independent of the DOTAP fraction C_{DOTAP} in the range of 1–7 mol%. In contrast to the behavior of the beads, the translational diffusion coefficient of membrane-bound DNA globules shows quite a pronounced dependence on the cationic lipid content C_{DOTAP} (Figure 4.6(a)), whereas it varies only weakly with the DNA contour length (Figure 4.6(b)). Assuming that the diffusion of membrane-bound DNA globules is related to their size according to the HPW theory (see Section 1.2.2), the very weak dependence of the globule diffusion on the DNA contour length suggests that for DNA with the contour length of 5–48.5 kbp, the resulting globules are compacted at a given DOTAP concentration to similar

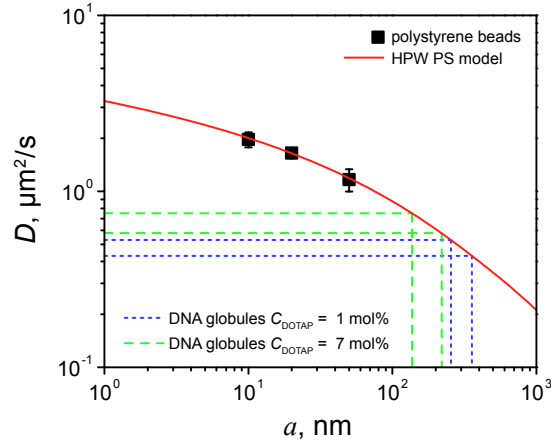


Figure 4.7: Relation of DNA globule diffusion and DNA globule size. Diffusion coefficients of polystyrene beads (black squares) adsorbed to a freestanding DOPC/DOTAP 99:1 membrane and HPW PS model (red curve, Equation (1.16)) for a membrane surface viscosity $\eta = 5.9 \times 10^{-10}$ Pa s m (see also Section 3.2.3). Estimates for the DNA globule sizes at freestanding DOPC/DOTAP membranes with $C_{\text{DOTAP}} = 1$ mol% (blue dotted lines) and $C_{\text{DOTAP}} = 7$ mol% (green dashed lines).

sizes independent of the DA contour length.

The growth of D with C_{DOTAP} clearly reflects the expected better compaction of DNA globules at higher cationic lipid content due to more efficient screening of the DNA charges. At the same time, the presence of the reproducible minimum at $C_{\text{DOTAP}} = 2$ mol% followed by a growth at 1 mol% is quite puzzling, and no clear explanation of this unexpected behavior can be offered at the moment.

Using the closed-form approximation of the HPW theory [54] (Equation (1.16)) and the membrane viscosity of 5.9×10^{-10} Pa s m, the hydrodynamic radius a of DNA globules can be estimated based on their diffusion coefficient. At $C_{\text{DOTAP}} = 1$ mol%, $a = 250\text{--}350$ nm, whereas at $C_{\text{DOTAP}} = 7$ mol%, $a = 130\text{--}200$ nm (Figure 4.7). These obtained DNA globule sizes are generally in agreement with predictions for interhelix distances in DNA-lipid complexes [159].

The exact conformation of a DNA molecule in the globule remains open to speculation. As the membrane is flexible and able to bend, it is not even clear whether the DNA would be compacted in a two- or rather three-dimensional arrangement.

To check whether a two-dimensional pancake conformation would be possible, one can estimate the area of a disc with the radius equal to the above-determined hydrodynamic radius a and compare it to the 2D area which can possibly be occupied by a single DNA molecule. A 2D λ -DNA globule of radius 200 nm at its strongest compaction leads to a disc area of $0.126 \mu\text{m}^2$ that shall be related to a single λ -DNA in the conformation of a densely packed two-dimensional pancake. Dense packing in this scenario would mean that the DNA molecule is arranged in a spiral, most probably with a hole in the middle whose radius should be of

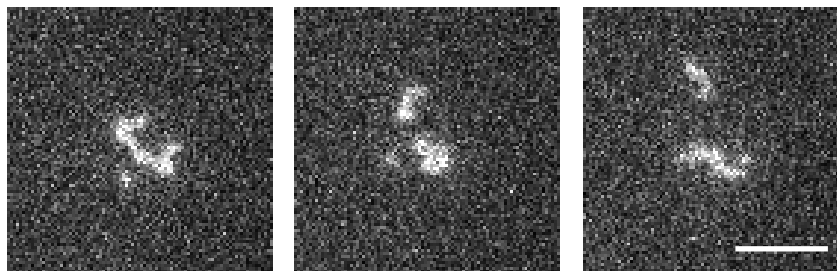


Figure 4.8: Fluorescent images of a 20 kbp DNA adsorbed to a freestanding membrane, DOPC/DOTAP 99:1, in a random coil conformation. At high excitation powers, photochemical effects lead to cleavage of the DNA molecule. Excitation power density: $\sim 10 \text{ W/cm}^2$. Scale bar: $5 \mu\text{m}$.

order of the DNA persistence length, to avoid overly strong local bending of the DNA. With a DNA molecule diameter of approximately 2 nm and a contour length of $21.4 \mu\text{m}$ (including a 30 % extension in length due to YOYO-1 labeling) one obtains an area of $0.043 \mu\text{m}^2$. However, one would expect that the cationic lipids serve as counterions and dress the DNA upon compaction. This increases the thickness by about 3.6 nm , the thickness of a DOPC bilayer [160]. The area occupied by the λ -DNA in this situation would be $0.12 \mu\text{m}^2$, leaving enough space for a hole of $40\text{--}50 \text{ nm}$ radius in the middle of the pancake. This estimate suggests a highly ordered chain conformation in the DNA globule that can only become more random if the globule has a three-dimensional structure.

Another observation indicates high ordering and possible wrapping of DNA with the cationic membrane in the globule conformation. Non-collapsed membrane-adsorbed DNA is easily photocleaved if the intensity of the laser used to excite YOYO-1 is substantially higher than 1 W/cm^2 . An example of such a photocleavage event is shown in Figure 4.8. This essentially means that the DNA is still exposed to oxygen in the surrounding medium and not enwrapped by the cationic membrane. DNA globules, on the other hand, are stable and inert to such photochemical effects, since no detachment of DNA parts from a globule was ever observed. This means that the chain organization of the DNA molecule in the globule is either very tight and regular, not allowing photocleaved fragments to leave the globule, or the DNA is shielded from oxygen by complete dressing with – and possibly incorporation into – the cationic membrane, or both. A further indication of complete membrane dressing of the DNA molecule in the globule conformation is the fact that fluorescence of YOYO-1 labeled DNA globules is virtually impossible to photobleach.

4.1.4. Implications of the coil–globule transition of membrane-bound DNA macromolecules for cell biology

The compaction of long DNA molecules interacting with fluid lipid membranes is an interesting observation that might explain parts of the mechanism of naked DNA uptake by cells which

is considered a “black box” [161] to the present day. The uptake of naked DNA is the simplest non-viral transfection method for cells in culture and in organisms. It was observed for a large variety of different cells and organisms, DNA types, and circumstances of administering (see [161, 162] and references therein).

Despite this large variety, some recurrent similarities are observed. Naked DNA binds to the cellular membrane and is believed to be incorporated via an endocytic pathway [161, 162, 163, 164, 165]. The gene expression indicating uptake of DNA by cells is a competitive process which is inhibited by adding excess amounts of non-expressing DNA or simply other polyanionic macromolecules [161, 162, 166, 165]. In light of these observations, and the striking absence of an identified specific receptor, one can suggest that the uptake of naked DNA is initiated by nonspecific electrostatic interactions of the DNA with positive charges at the cellular membrane, originating from cationic lipids such as sphingosine or cationic domains of membrane proteins.

The size of long DNA molecules, such as λ -DNA, in a coil conformation in solution is easily $\gtrsim 1 \mu\text{m}$ and an additional spreading due to assumption of a 2D conformation upon attachment to the membrane can be expected. At this size the long DNA would be far too large to be incorporated directly into an endosome. Therefore, the ability of the DNA molecule to undergo a transition to a 100–200 nm sized globule on a fluid deformable membrane would be a crucial prerequisite for the endocytic pathway of DNA internalization.

4.2. DNA on freestanding and supported cationic gel-phase membranes

The membrane-mediated coil-globule transition of DNA molecules is only observed upon adsorption to a fluid *freestanding* cationic lipid bilayer, but not at a fluid *supported* cationic lipid bilayer. The reason for the ability of DNA molecules to collapse when adsorbed to the freestanding membrane may be found in local lipid segregation and/or local membrane deformation.

In order to confirm that the effects of membrane deformation and lipid segregation are responsible for the condensation of membrane-adsorbed DNA molecules, in this Section a freestanding cationic membrane with a DMPC/DMTAP 90:10 lipid composition, which is in the gel state at the room temperature of 23 °C [81], is used. For a gel-phase membrane the lipid mobility and thus the possibility of lipid segregation in response to adsorbed DNA molecules is strongly reduced. In addition, the membrane flexibility of a freestanding gel-phase bilayer is strongly suppressed. Therefore, if the assumptions above are correct, no condensation of membrane-adsorbed DNA molecules should be expected. Furthermore, the strength of the interaction between DNA molecules and the lipid bilayer can be tested, to answer the question, whether DNA molecules are able to glide on the surface of the cationic

membrane or their mobility is strongly coupled to the mobility of the membrane lipids.

In an additional experiment with supported cationic gel-phase membrane bilayers, the influence of lipid segregation on the conformation of membrane-bound DNA molecules can be investigated. The binary lipid mixture of DMPC/DMTAP 90:10 exhibits a gel-fluid phase coexistence in the range of approximately 27–29 °C [81]. The gel–fluid membrane transition temperature is increased by the addition of DMTAP to a DMPC membrane [81], which means that for a gel-fluid phase coexistence, the cationic DMTAP is enriched in the gel-phase membrane domains. In case where a supported membrane with such a composition is cooled down from the temperature corresponding to the fluid state to a temperature corresponding to coexistence of the gel and fluid state, micrometer-sized domains of the cationic lipid-enriched gel phase will appear whose further growth and mobility will be arrested due to pinning to defects on the substrate. Using this membrane property, an artificial charge segregation can be created, and the conformational behavior of membrane-adsorbed DNA molecules in such a system can be investigated.

4.2.1. Experimental details

For experiments with gel-phase membranes, a cationic lipid composition of DMPC/DMTAP 90:10 was used. The membrane was fluorescently labeled with 0.1 mol% DiD.

SGUVs were produced by electroformation (see Sections 2.2.2 and 3.1), with a minor but important change in the spreading of the lipid-chloroform solution on the ITO coverslip. Instead of a lipid concentration in chloroform of 10 mg/ml, a tenfold lower concentration of 1 mg/ml was used. At the same time the volume of the lipid solution that was spread was increased by the same factor of ten. Ultimately, the same amount of lipids was spread, but instead of applying a single snake-like pattern, the lipid solution was spread repeatedly over the same area. This adjustment was necessary, as for the unknown reason the normal procedure did yield vesicles, most of which, however, had smaller sizes and were detached from the coverslip surface. Using the low concentration and repeated spreading of the lipid solution, on the other hand, ensured formation of SGUVs sitting in a dome-like fashion on the ITO-coated coverslip similar to the DOPC/DOTAP vesicles. The electroformation was carried out at 50 °C, above the gel–fluid phase transition temperature.

Differential scanning calorimetry experiments [81] showed that the phase transition temperature of the DMPC:DMTAP 90:10 membrane is found approximately at 27–29 °C for a sample of multilamellar vesicles. A similar transition temperature is expected for the SGUV membrane. To qualitatively confirm the SGUV membrane phase-state, fluorescence bleaching and recovery experiments were carried out at temperatures above and below the expected transition temperature. At 23 °C indeed no recovery of fluorescence in the bleached area of the vesicle membrane was observed, indicating that the membrane is in the gel-phase, while at

30 °C fluorescence did recover, indicating that the membrane is in the fluid-phase. Therefore, at these temperatures fluorescently labeled DNA was injected into the SGUV chamber in the same fashion as described above in Section 4.1.1, to investigate the difference in the behavior of DNA molecules adsorbed to a freestanding fluid-phase and a freestanding gel-phase membrane.

Therefore, in experiments with DMPC/DMTAP vesicles with a fluid-phase membrane the sample was kept at 30 °C by temperature-feedback controlled heating of the microscope objective and the sample chamber. For experiments with DMPC/DMTAP vesicles with a gel-phase membrane the sample was kept at the room temperature of 23 °C.

Supported lipid bilayers (SLBs) of DMPC/DMTAP 90:10 lipid composition were formed on mica using the spin coating method as described in Section 2.2.1. The rehydration of the dried lipid film was carried out in dd-H₂O at 50 °C.

The temperature range of gel–fluid phase coexistence of 27–29 °C for a DMPC/DMTAP 90:10 membrane is expected to be broadened and shifted to higher temperatures if the membrane is placed on a solid support (see discussion in Section 1.1.3). This was verified by fluorescence photobleaching and recovery experiments of the fluorescent membrane label DiD. Only at a temperatures above 42 °C the membrane appears to be in the fluid phase, which is indicated by a homogenous distribution of the fluorescence of DiD and its fast recovery after photobleaching. If the temperature is decreased by about one degree, small, immobile, dark domains appear, while the bright part of the surrounding membrane is still in the fluid state. It was found that the membrane label DiD is squeezed out of gel domains [167] and that for the closely related membrane dye DiI, the fluorescence intensity is reduced in the gel phase of a DMPC membrane compared to the fluid phase [168]. This indicates that the appearing dark regions are membrane domains in the gel state. The immobility of the gel domains most likely caused by pinning to defects on the substrate is a typical observation for SLBs. At about 38 °C the entire membrane including the brighter regions around the dark domains goes into the gel phase, as no recovery after photobleaching is observed.

Fluorescently labeled DNA in dd-H₂O at a concentration of 10⁻⁷ M was added to the SLB sample, incubated for about ten minutes, and afterwards thoroughly washed with dd-H₂O to remove the DNA molecules remaining in solution, all at a temperature of about 50 °C.

To sample containing the SLB and membrane-adsorbed DNA molecules was placed on the microscope and kept at the desired temperature using temperature-feedback controlled heating of the microscope objective and the sample chamber.

4.2.2. Behavior of DNA molecules adsorbed to freestanding cationic gel-phase membranes

For experiments with cationic gel-phase membranes, λ -DNA molecules were injected into the DMPC/DMTAP 90:10 SGUV sample at 23 °C. Shortly after the injection, DNA molecules adsorb to the freestanding cationic gel-phase membrane and are arrested at the position of adsorption in a shape that does not change over the course of time (Figure 4.9(a)). The observed DNA shape is more extended than that of a DNA globule resulting from membrane-mediated DNA condensation on a freestanding cationic fluid membrane of the same DMPC/DMTAP 90:10 lipid composition at 30 °C (Figure 4.9(b)) or a DOPC/DOTAP lipid composition at a similar temperature of 24 °C (Figures 4.1(c) and 4.2). On the other hand, the conformation of the λ -DNA adsorbed to the gel-phase membrane (Figure 4.9(a)) is much less extended than the random coil conformation of non-collapsed λ -DNA molecules on a fluid freestanding bilayer (Figure 4.2(a)) but agrees well with the 2D projection of the shape the DNA molecules diffusing freely in the surrounding medium (Figure 4.1(b)).

These observations allow one to draw two conclusions. First, DNA molecules are tightly bound to the membrane, they cannot glide on the surface of a gel-state cationic membrane and their extremely low mobility matches the lipid mobility in the gel-state membrane. Second, as shown by the experiments with freestanding cationic gel-phase membranes, membrane-attached DNA molecules indeed cannot undergo a coil-globule transition without local lipid segregation in the membrane and/or dynamic local membrane deformations.

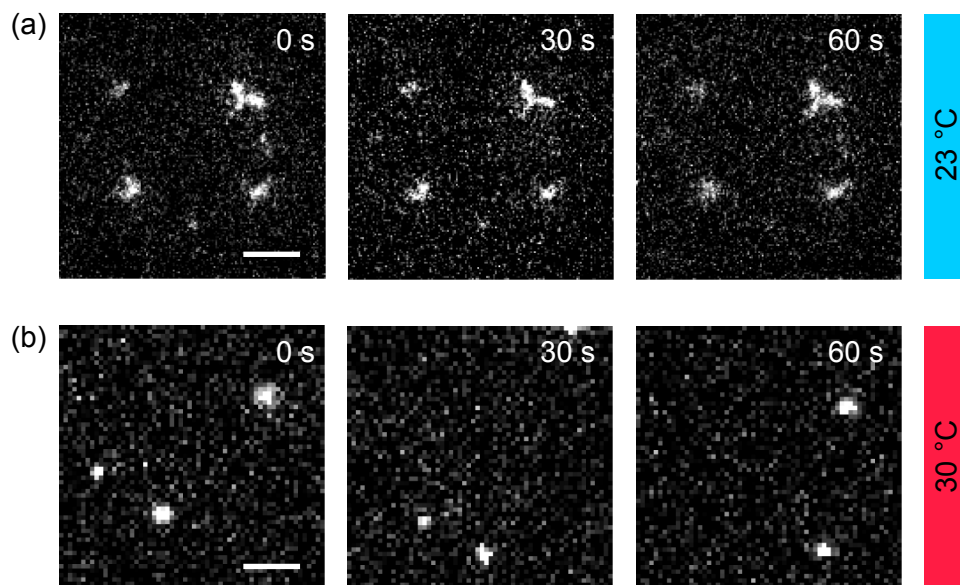


Figure 4.9: Fluorescent images of λ -DNA adsorbed to SGUVs with the lipid composition of DMPC/DMTAP 90:10. (a) λ -DNA on a freestanding gel-phase membrane at 23 °C. (b) λ -DNA on a freestanding fluid-phase membrane at 30 °C. Scale bars: 5 μm .

4.2.3. Conformational behavior of DNA molecules at the fluid–gel transition of SLBs

When DNA molecules adsorb to the fluid cationic SLB with a lipid composition of DMPC/DMTAP 90:10, which is heated to a temperature of 44 °C, the phenomenology of their behavior is similar to what is observed for DNA on a fluid DOPC/DOTAP SLB [8, 9] (see also Figure 4.1(a)). Namely, they assume a 2D random coil conformation and exercise Brownian motion (Figure 4.10(a)).

If the temperature of the sample is reduced below 42 °C, small, immobile, dark gel-membrane domains appear (Figure 4.10(b, middle)). If the diffusing random coil DNA molecules adsorbed at the fluid membrane regions meet the gel-phase domains an interesting effect is observed. The DNA molecules bind to the gel-phase domains and get strongly compacted. Figure 4.10(b) shows that one of the three 20 kbp DNA molecules is compacted completely at the position of a gel-membrane domain (the rightmost DNA molecule in the image), the second one diffuses at a distance to the gel domains and still remains in the coil conformation (the leftmost DNA molecule in the image), and the third one is partially compacted, with the DNA compaction located at the position where the macromolecule has met the gel-phase domain (the DNA molecule in the middle of the image).

In the course of the experiment, while the membrane is slowly further cooled down to 38 °C, all these membrane-bound DNA molecules finally reach the gel-phase domains and get compacted (Figure 4.10(c)). Note that membrane domain pattern is kept when the final transition to the gel state is reached, although at this temperature the bright membrane regions in Figure 4.10(c, middle) are in the gel state as well. (This was confirmed by fluorescence photobleaching)

Generally, not necessarily every membrane-adsorbed DNA molecule gets compacted in the fluid–gel transition process. In case the DNA does not reach a previously formed gel domain, it can get arrested in a coil conformation when the whole membrane finally converts into the gel state.

Interestingly, the compaction of DNA molecules adsorbed to a SLB upon interaction with a gel-phase domain is reversible. If the sample is heated back above the membrane gel–fluid coexistence temperature, the dark gel domains disappear, and the previously compacted DNA molecules decompact, assume a random coil conformation again (Figure 4.10(d)), and resume their Brownian motion on the membrane.

As previously discussed in the introduction to this Section, the gel domains of a DMPC/DMTAP membrane are expected to be enriched with cationic DMTAP lipids compared to the surrounding fluid membrane regions. This leads to a higher charge density in the gel domains which is further enhanced by a tighter lipid packing expected in the gel state [14, 15]. This, phase separation-induced lipid (and charge) segregation in the membrane is

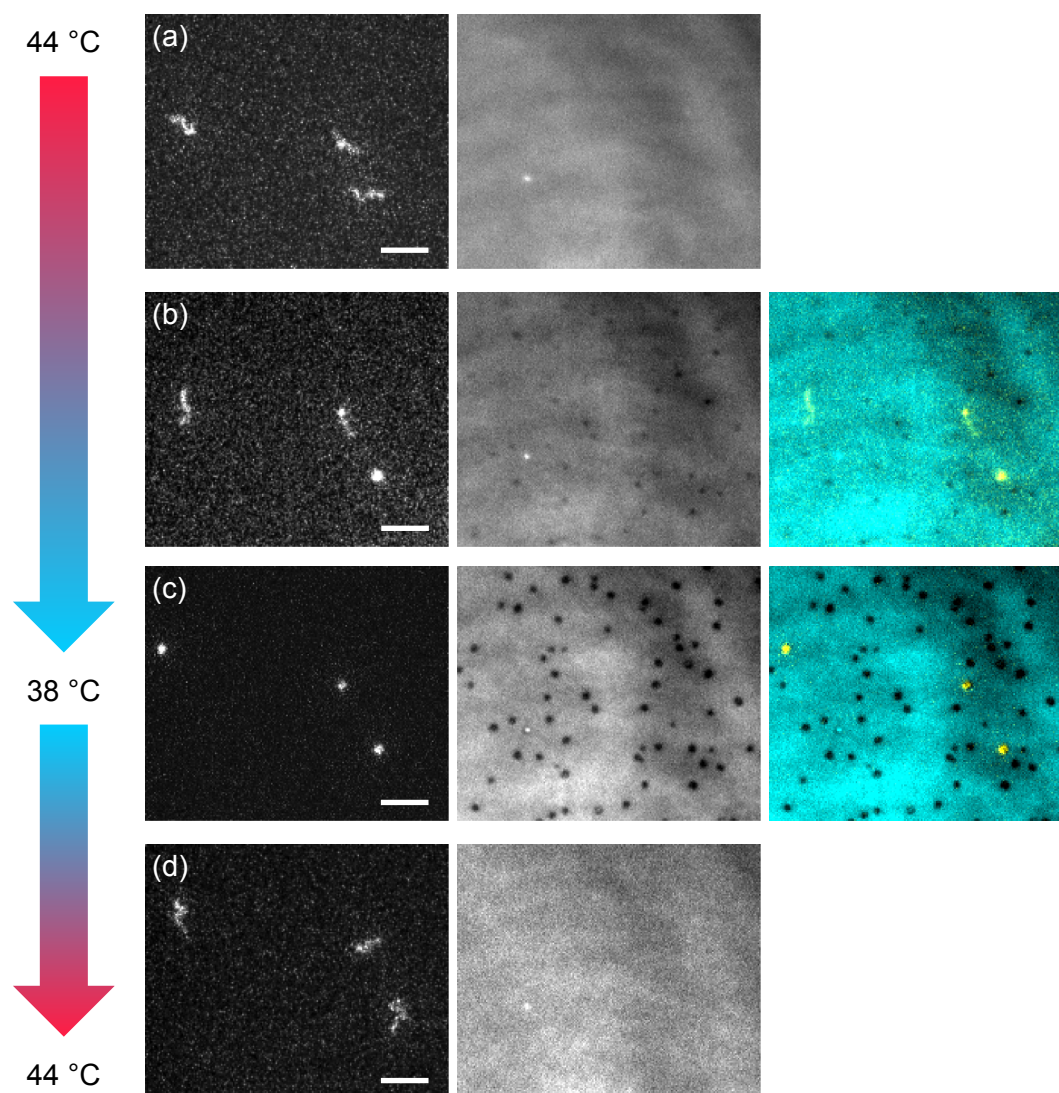


Figure 4.10: Fluorescent images of 20 kbp DNA adsorbed to a supported lipid bilayer passing through the fluid-gel and gel-fluid phase transition. Lipid bilayer composition: DMPC/DMTAP 90:10. (a) 44 °C. Two-dimensional DNA coils (left hand side) adsorbed to a homogeneous fluid bilayer (right hand side). (b) Approximately 40 °C. DNA molecules in random coil, and compacted and partially compacted conformation (left hand side). Appearance of small dark gel-membrane domains in the fluid lipid bilayer (middle) and merged image of the two channels (right hand side). (c) 38 °C. DNA molecules in compacted conformation (left hand side). Lipid bilayer in gel phase with dark domains (middle) and merged image of the two channels (right hand side). (d) 44 °C. Decompacted DNA coils (left hand side) at a homogeneous fluid bilayer (right hand side). Scale bars: 5 μm .

able to cause the compaction of SLB-adsorbed DNA molecules. The DNA compaction can be fully reversed if membrane is heated above the gel-fluid phase transition temperature. As a consequence, the membrane-gel domains, and along with them the artificial lipid segregation, disappear.

The observed compaction and decompaction of DNA molecules on supported membranes

that pass the fluid–gel phase transition can be repeated many times by repetitive cooling and heating of the sample. This indicates that the compacted membrane-bound DNA are not completely dressed with lipids and or enwrapped by the membrane. This assumption is further strengthened by the observation that the fluorescence excitation with laser powers of about 10 W/cm^2 *does* cause photo-destruction of the compacted DNA chains that are attached to a gel-phase domain of a supported lipid membrane. If the membrane is heated above the phase transition after such a treatment one observes very short photocleaved DNA fragments which diffuse away on the membrane from the location where the initially large DNA molecule was compacted.

This behavior is entirely different compared to the observations of the DNA globules formed on a fluid freestanding lipid membrane as discussed in Section 4.1.3. There, once the DNA molecule assumes a globule conformation a reverse decompaction was never observed and the DNA globules are not affected by photobleaching and photocleaving. Therefore, one may suggest that on freestanding fluid membranes the DNA coil–globule transition is initiated by a local lipid segregation and is accompanied by local membrane deformations, which stabilize the compact DNA globule.

4.3. Conclusion

Thus, our experiments with DNA macromolecules adsorbed to fluid freestanding cationic membranes show a change in DNA conformation from a 2D random coil to a compact globule depending on the fraction of cationic lipids in the bilayer and the length of the DNA. The globule state is favored at high cationic lipid concentrations and long DNA contour lengths. On the contrary, at low cationic lipid concentrations the majority of the membrane-adsorbed DNA molecules is in a random coil conformation. In the latter case, the DNA–membrane interactions are apparently too weak to facilitate a DNA coil–globule transition. At cationic lipid concentrations close to those where all adsorbed DNA molecules collapse to globules, partially collapsed DNA molecules are observed for long DNA molecules of 48.5 kbp and 20 kbp. In the observed events of membrane-mediated DNA coil–globule transition we found that the DNA collapse is a fast process with a compaction rate of $124 \pm 46 \text{ kbp/s}$. Fluorescence microscopy experiments clearly show that the size of the membrane-bound DNA globules does not exceed 500 nm. By relating the translational diffusion coefficients of completely collapsed DNA globules to the radius of a membrane inclusion an estimate of the DNA globule size was obtained and found to be 250–350 nm at DOPC membranes containing 1 mol% DOTAP and 130–200 nm for 7 mol% DOTAP, indicating a stronger compaction for higher charge densities in the membrane.

Additional experiments with freestanding cationic membranes in the gel state and supported cationic lipid membranes with gel–fluid coexistence suggest that the DNA collapse on

a freestanding fluid cationic membrane may be initiated by a local lipid segregation in the membrane and accompanied by local membrane deformations, which stabilize the compact DNA globule.

Brownian Motion and Conformational Dynamics of DNA and *fd*-Virus on Freestanding Membranes with Low Cationic Lipid Concentration

Many biological macromolecules and supramolecular assemblies can be described as semiflexible polymers and filaments (see Section 1.3), and a large number of them “interact” with biological membranes. Surprisingly though, very little is known about the diffusion and conformation of individual semiflexible particles bound to lipid membranes.

Semiflexible filamentous particles which are adsorbed to a freestanding lipid membrane should exhibit an interesting diffusion behavior. In particular, a double crossover in the behavior of their diffusion coefficients as a function of their size can be expected. One crossover should be found when the particle size a goes from the regime $a \ll l_{SD}$ to the regime $a \gg l_{SD}$, where l_{SD} is the hydrodynamic length scale (Saffman-Delbrück length) which characterizes the influence of the viscous membrane on the diffusion of the adsorbed particle. The other crossover in diffusion behavior can be expected due to the conformation of the particle in case where the particle size large enough ($a \gtrsim l_{SD}$), and its contour length L goes from the regime $L \ll l_p$ (stiff rod) via the regime $L \approx l_p$ (semiflexible filament) to the random coil regime $L \gg l_p$, where l_p is the persistence length of the filament.

To address experimentally the diffusion and conformation of semiflexible particles adsorbed to a membrane, we use long (> 5 kbp) DNA molecules that assume a random coil conformation on a freestanding membrane with a low cationic lipid content (see Section 4.1.2, [121]) and semiflexible *fd*-virus particles. The sizes of the above filamentous semiflexible particles can be easily controlled using biotechnology methods, and their conformations are resolvable by fluorescence wide-field microscopy. Additionally, their sizes can be tuned to sample a range of scales above and below the SD length of the membrane.

The DNA molecules are comparatively soft with a persistence length of few hundreds of

nanometers under low salt conditions [74, 169]. At a contour length of about 21.4 μm for YOYO-1 labeled λ -DNA the ratio of contour length L and persistence length l_p , L/l_p , is large and the conformation of the molecule is expected to be a random coil. On the other hand, the *fd*-virus is rather stiff with a persistence length of about 2 μm to 3 μm [76, 80]. As a result, the ratio of L/l_p ranges from $L/l_p \approx 0.5$ for the virus monomer to about $L/l_p \approx 4$ for the longest virus particles observed in this study. Therefore, *fd*-virus particles and long DNA molecules complement each other in covering a broad range of the filament flexibility from the stiff rod to the random coil regime. At the same time, both DNA and *fd*-virus particles can be assumed as infinitely thin because their thickness (2 nm for DNA [67] and 6.6 nm for *fd*-virus [75]) is very small compared to their contour lengths.

At the moment, hydrodynamics-based theories exist which describe the Brownian motion of polymers and filaments on freestanding membranes only in the limiting regimes of a stiff rod [63, 64, 65, 66] and a 2D Gaussian chain [62]. In this Chapter we experimentally test these theories and their applicability limits for the quantitative description of the rotational and translational diffusion coefficients of membrane-bound semiflexible particles.

5.1. Experimental details

The experimental procedure for YOYO-1 labeled DNA molecules of 5 kbp, 10 kbp, 20 kbp and 48.5 kbp was exactly the same as described in Section 4.1.1 in the previous Chapter. In contrast to the previous Chapter, experiments described in this Chapter were carried out only with SGUVs electroformed from lipid mixtures of 99 mol% DOPC and 1 mol% DOTAP.

For the *fd*-virus experiments, SGUVs of the same membrane composition were used. An aqueous suspension of virus particles fluorescently labeled with Alexa488 was diluted in dd-H₂O to a concentration of approximately 10^{-9} M estimated from the particle density in solution via fluorescent imaging. The *fd*-virus solution contained monomeric viruses, as well as but multimeric virus particles with longer contour lengths. The dilution included a three times repetition of ultracentrifugation at 100,000 g for 30 minutes. After every centrifugation step 1.45 ml out of the 1.5 ml of supernatant were replaced with dd-H₂O. The centrifugation led to a higher fraction of the longer multimeric virus particles as almost exclusively monomeric viruses were removed from the sample with the supernatant. The final *fd*-virus solution was injected into the sample chamber containing the cationic SGUVs at a rate of 10 $\mu\text{l}/\text{min}$ with the help of a syringe pump and left to incubate for about 1h.

All experiments were carried out at the room temperature of 24 $^{\circ}\text{C}$.

Movies consisting of several thousand frames were taken for DNA molecules adsorbed to at least ten different SGUVs per DNA length at a frame rate of 10 Hz and exposure time of 50 ms, at a resolution of 389 nm/pixel for 48.5 kbp and 20 kbp and 158 nm/pixel for 10 kbp and 5 kbp.

For the *fd*-virus, a higher lateral resolution of 75 nm/pixel was used, and images were acquired at the maximum full-frame readout rate of the camera with a frame time of 32 ms and exposure time of 30 ms. Trajectories consisting of 200 to 2000 steps were obtained and analyzed and the respective diffusion coefficients were averaged for the virus multimers: 49 trajectories for $[fd]_1$, 26 for $[fd]_2$, 16 for $[fd]_3$, 4 for $[fd]_4$, 15 for $[fd]_5$, 4 for $[fd]_6$, 3 for $[fd]_7$, 9 for $[fd]_{10}$, and 1 for $[fd]_{11}$.

Positions and orientations, as well as radii of gyration of individual DNA molecules were obtained using the first and second moments of the image intensity distribution, respectively. The same parameters and additionally the filament contour length of the *fd*-virus particles were obtained by the particle contour analysis. For detailed description of the methods see Sections 2.4.1, 2.4.2 and 2.4.3.

Rotational and translational diffusion coefficients of DNA molecules and *fd*-virus particles adsorbed at freestanding lipid membranes were obtained using the methods described in Sections 2.4.5, 2.4.6, and Appendix A.1.

5.2. Conformation of membrane-adsorbed *fd*-virus particles and random-coil DNA molecules

5.2.1. Radius of gyration and persistence length of random-coil DNA molecules on a freestanding membrane

We have found that under the conditions of our experiments DNA molecules attach to the SGUVs membrane with low cationic lipid content and immediately after adsorption assume a two-dimensional random coil conformation and exercise rotational and translational Brownian motion. Figure 5.1 shows typical snapshots of the fluorescently labeled DNA molecules of various lengths which are adsorbed to a freestanding fluid membrane.

DNA molecules equilibrate very fast upon binding to a freestanding membrane: No detectable difference in the conformation and radius of gyration of membrane-bound DNA molecules is found when they are observed at different times after the adsorption, ranging from minutes to several hours.

The dependence of the radius of gyration R_g of DNA macromolecules on their contour lengths L can provide the important information on the conformational state of the membrane-adsorbed macromolecules. For example, in their study of DNA adsorbed at supported lipid bilayers, Maier and Rädler found that the radius of gyration scales as $R_g \sim L^\nu$ with $\nu = 0.79 \pm 0.04$ [8, 9]. This observation was interpreted in [8, 9] in terms of strong excluded-volume interactions within the DNA chain for which the theory predicts $\nu = 3/4$ in 2D [170]. [70, 71]

Remarkably, for DNA molecules adsorbed at a freestanding cationic lipid bilayer we find

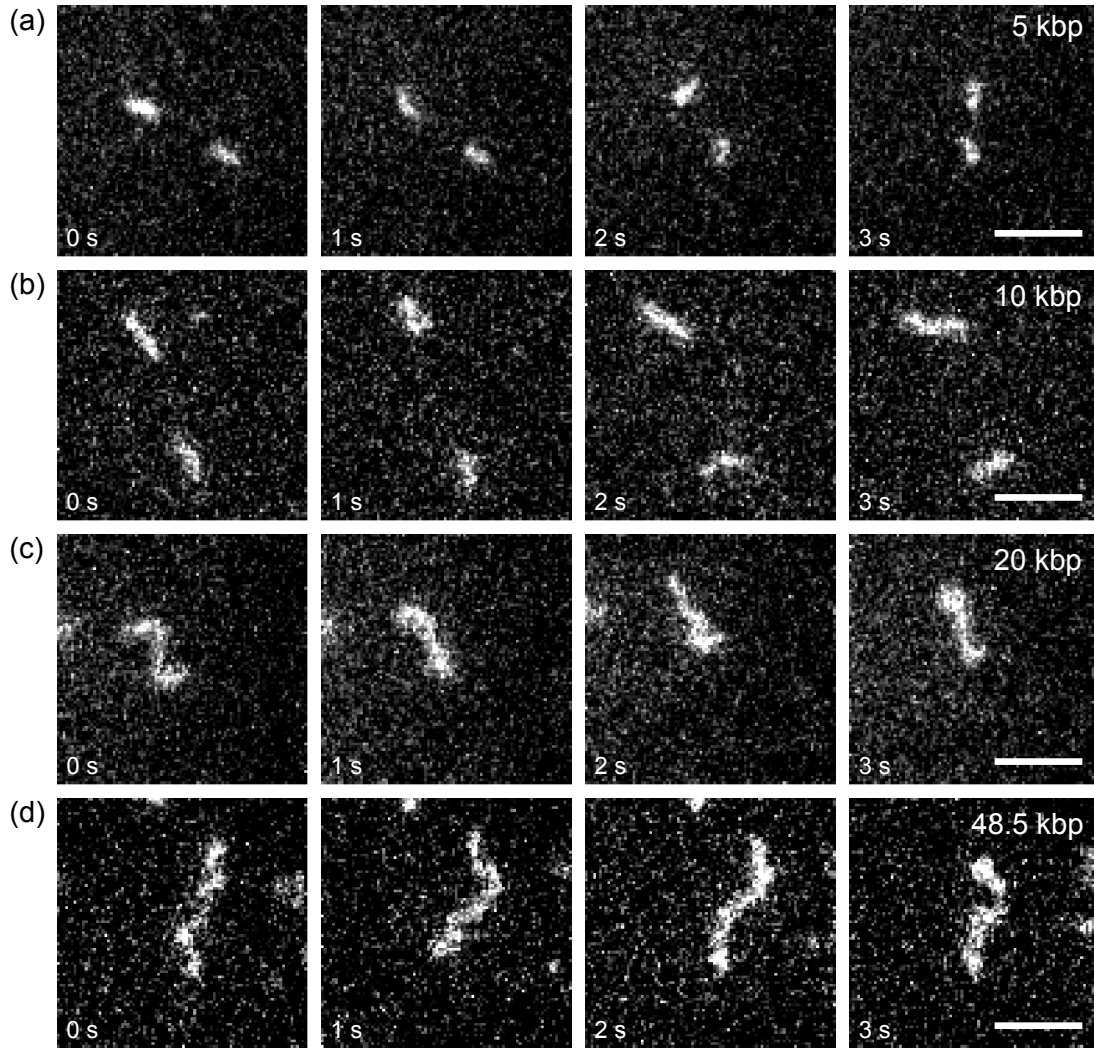


Figure 5.1: Snapshots of fluorescently labeled DNA adsorbed to a freestanding cationic DOPC/DOTAP 99:1 membrane, illustrating the motion, size and shape fluctuations of DNA molecules of different length. (a) 5 kbp, (b) 10 kbp, (c) 20 kbp, (d) 48.5 kbp. Fluorescent label: YOYO-1. Scale bars: 5 μm .

a strikingly different dependence (Figure 5.2). We clearly see that the $R_g(L)$ dependence does not follow the power law expected for the 2D swollen chain. Even more interestingly, the dependence is well described by the expression expected for a semiflexible chain in 2D (Equation (1.32)). Fitting the data with this expression gives the persistence length $l_p = 260 \pm 40$ nm. It should be noted that the persistence length of a polyelectrolyte depends on the ionic strength of its environment: $l_p = l_{p,0} + l_{p,e}$. Here, $l_{p,0}$ is the intrinsic persistence length of the polyelectrolyte and $l_{p,e}$ is the electrostatic contribution [70, 71]. The persistence length of ~ 260 nm we found for DNA on freestanding membranes is considerably larger than the intrinsic persistence length of DNA $l_{p,0} \approx 30\text{--}50$ nm [72, 74, 171]. This may reflect the

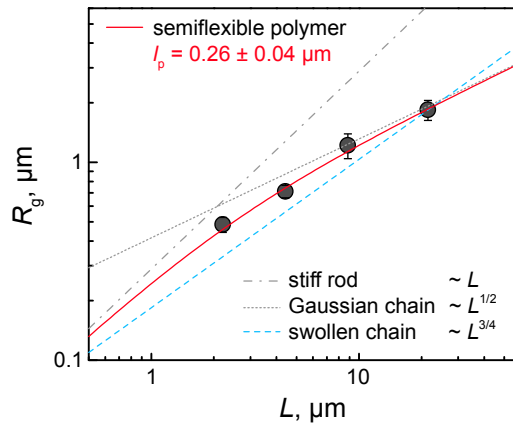


Figure 5.2: Radius of gyration R_g of 2D random coil DNA molecules adsorbed to a freestanding fluid cationic membrane versus the DNA contour length L . A fit to the WLC model (red curve) yields a persistence length $l_p = 0.26 \pm 0.04 \mu\text{m}$. Also shown are the asymptotics of the WLC model, the stiff rod (gray dash dotted line) and a Gaussian chain random coil (gray dotted line). The blue dashed line indicates a scaling with $L^{3/4}$ which is expected for strong influence of volume exclusion effects between polymer chain segments. The contour length L of YOYO-1 labeled DNA fragments with the known nominal length in bp was determined as described in Section 2.3.1.

electrostatic stiffening of the DNA chain under our experimental conditions. Moreover, the value of $l_{p,e} \approx 210\text{--}230 \text{ nm}$ corresponds to what is found for DNA in a bulk solution at a monovalent salt concentration of about $1.5 \times 10^{-4} \text{ M}$ [74, 169]. This explanation seems to be reasonable, since the membrane charge density is low (1 mol% cationic lipids), and no salt was added to the surrounding medium (dd-H₂O).¹

It is possible to reconcile the seemingly contradictory pictures observed in the previous experiments by Maier and Rädler [8, 9] and in the present work using the results of the study by Yoshinaga *et al.* [172]. In this study it was found that a DNA molecule adsorbed at a 2D substrate shows three distinct scaling regimes in the dependence of the end-to-end distance on the contour length $d_{ee} \sim L^\nu$: (i) $\nu \approx 1$ for $L < 4l_p$ (stiff rod), (ii) $\nu \approx 0.5$ for $4l_p < L < L_c$ (2D ideal chain), and (iii) $\nu \approx 0.75$ for $L > L_c$ (2D self-avoiding walk, which corresponds to a polymer with strong excluded-volume interactions, or swollen polymer chain in two dimensions). L_c is the critical length separating regimes (ii) and (iii). This critical length can be expressed via the corresponding critical number N_c of Kuhn segments: $L_c = 4l_p N_c$ (for a chain in 2D). The theoretical estimates by Yoshinaga *et al.* show that $N_c \gg 16l_p^2/B$, where B is the second virial coefficient of the polymer chain. Obviously, all these three regimes will also be observed in the scaling behavior of the radius of gyration R_g . The only difference will be that the crossover between the regimes will take place at contour lengths larger by a factor

¹At the same time one cannot exclude an additional DNA stiffening due to interaction with the freestanding membrane which might lead to local deformations of the latter on the scale of a few nanometers. This issue deserves further experimental and theoretical investigation.

of two compared to the behavior of the end-to-end distance.

If one adopts this picture, then our experimental results correspond to the crossover between regimes (i) and (ii) (from the stiff rod to the ideal chain), while the results of Maier and Rädler belong to regime (iii) (self-avoiding walk). The question remains, why the DNA molecules with contour lengths in the same range studied in these two experiments show behavior which belongs to different scaling regimes. The answer in our opinion lies in the different strength of the electrostatic interaction between the DNA chain segments in our work and the study by Maier and Rädler. Indeed, according to their estimates, at the experimental conditions of their work (10 mol% cationic lipids, 10 mM NaCl in buffer) electrostatic interactions along the DNA chain are insignificant, so that the persistence length of DNA is virtually unaffected by electrostatics: $l_p \approx 50$ nm [8, 9]. In this case, according to experimental observations and theoretical estimates of Yoshinaga *et al.* [172], the radius of gyration of DNA molecules longer than 6 kbp should indeed show the scaling characteristic of the 2D self-avoiding walk regime (iii). On the other hand, considerable electrostatic stiffening of the DNA chain in case of our experiments ($l_p \approx 260$ nm) should bring the DNA molecules with the lengths from 5 kbp to 48.5 kbp to the crossover region between regimes (i) and (ii), while the crossover to regime (iii) is expected to take place only for DNA molecules with the contour length $L \gtrsim 100$ kbp, and therefore should not be observed in our experiments.

Based on this observation and results of the work of Yoshinaga *et al.* [172] it is possible to obtain the lower estimate of the second virial coefficient of the DNA in our experiments, $B \gtrsim 64l_p^3/L\lambda_{\text{DNA}} \approx 0.05 \mu\text{m}^2$. This is considerably larger than the corresponding estimate of $0.013 \mu\text{m}^2$ obtained by Maier and Rädler based on their experimental data, which is again in agreement with our assumption of the stronger effect of electrostatic interactions in our experiments. Using these results we can also obtain an estimate of the interaction width of the DNA chain. Taking B as the excluded area of a polymer segment on the 2D surface, $B \simeq 4l_p w$, where w is the interaction width of the polymer segment, we obtain $w \gtrsim 50$ nm. If we attribute the segment-segment interaction to electrostatic repulsion, this interaction width would correspond to the Debye length $\lambda_D \simeq w/2 = 25$ nm of an aqueous solution with the ionic strength $I \lesssim 1.5 \times 10^{-4}$ M, which is in surprisingly good agreement with the value of the ionic strength at which the persistence length of DNA is $l_p \approx 260$ nm [74, 169] (see above).

Thus we conclude that upon adsorption to a freestanding cationic lipid bilayer with a low charged lipid fraction, which is surrounded by solvent with a very low ionic strength, DNA with the contour lengths of up to 48.5 kbp behaves as a 2D semiflexible polymer.

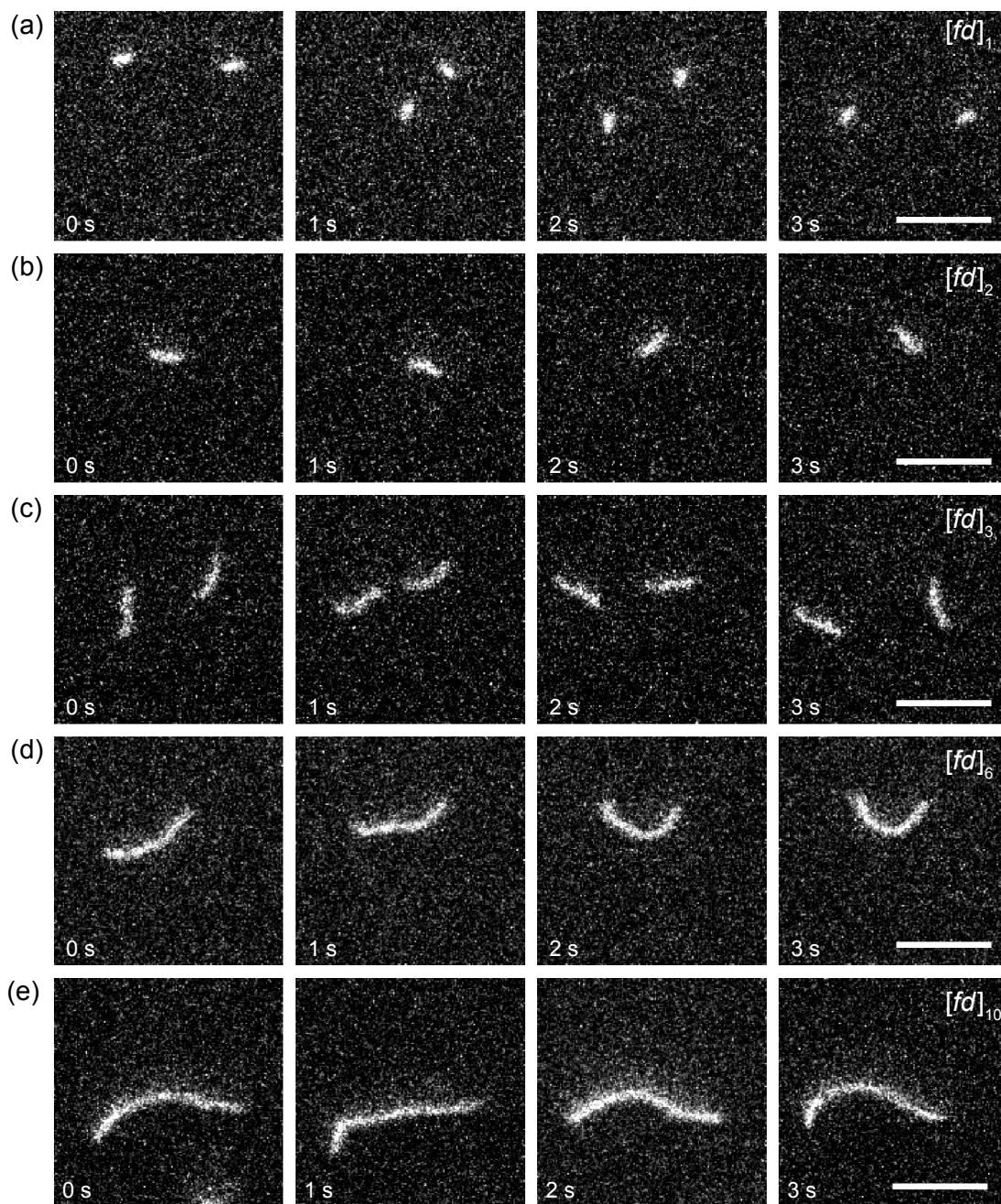


Figure 5.3: Snapshots of fluorescently labeled *fd*-virus particles adsorbed to a freestanding cationic DOPC/DOTAP 99:1 membrane, illustrating translational and rotational motion and thermal shape fluctuations of *fd*-virus multimers. (a) Monomers, $[fd]_1$. (b) Dimer, $[fd]_2$. (c) Trimers, $[fd]_3$. (d) Hexamer, $[fd]_6$. (e) Decamer, $[fd]_{10}$. Fluorescent label: Alexa488. Scale bars: 5 μm .

5.2.2. Radius of gyration and persistence length of membrane-adsorbed *fd*-virus particles

Several fluorescent image time series of *fd*-virus particles of various lengths adsorbed to a freestanding fluid cationic lipid bilayer are shown in Figure 5.3 to illustrate translational and

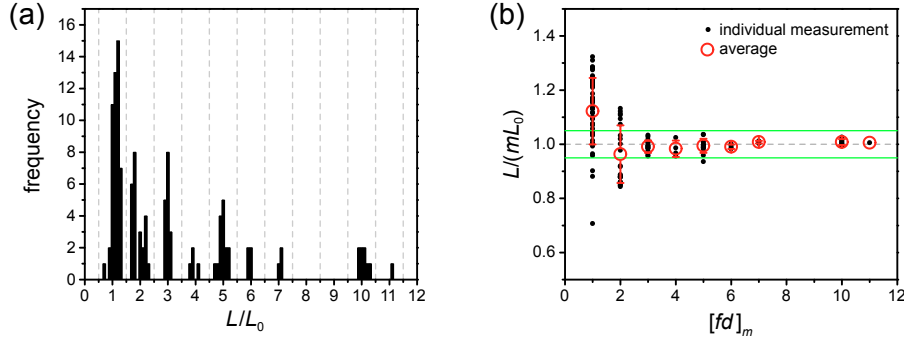


Figure 5.4: Length of membrane adsorbed *fd*-virus particles determined by full contour analysis. (a) Histogram of determined virus lengths normalized by the expected *fd* monomer length $L_0 = 0.88 \mu\text{m}$. (b) Determined virus length normalized by the quantized virus length mL_0 depending on the degree of multimerization m . The green lines indicate a relative error of $\pm 5 \%$.

rotational motion and thermally induced shape fluctuations as a function the filament length.

As it has been discussed earlier (Sections 1.3.4 and 2.1), in our experiments we used *fd*-viruses grown in a JM101 *E. coli* host strain, which leads to occasional appearance of multimeric virus particles. As a result, the virus sample represents a mixture of the monomeric and multimeric *fd*-virus particles. Since the m -mer virus particle is produced by a linear unidirectional growth process starting from a monomer, one can speculate that the relative fraction of an m -mer f_m scales as $f_m/f_1 \sim p^{m-1}$, where p is the probability of forming a dimer virus particle. This means that the number of higher multimers in the sample is exponentially small, which indeed qualitatively agrees with our experimental observations. The development of a size separation procedure, which would allow one to obtain monodisperse samples of *fd*-virus particles was outside the scope of the present thesis, and experiments were carried out with a mixture of virus particles with different lengths.

This experimental situation requires the determination of the lengths of the individual virus particles and thus identification of the degree of multimerization m , based on the analysis of experimental images.

The length obtained by the contour analysis allows for a clear identification of the degree of multimerization m (Figure 5.4(a)). Moreover, the length determination of individual virus particles agrees to the expected length of mL_0 within better than $0.4/m \times 100 \%$ (Figure 5.4(b)).

After carrying out the full contour analysis, the filament end-to-end distance d_{ee} is known, and the radius of gyration R_g can be calculated for the individual *fd*-virus multimers. In the WLC model for semiflexible polymers d_{ee} and R_g are related to the persistence length of the filament l_p and the filament length L according to Equations (1.35) and (1.32), respectively. A least squares fit to the data yields $l_p = 2.2 \pm 0.1 \mu\text{m}$ for both d_{ee} and R_g (see Figure 5.5). This result is in perfect agreement with the value of $2.2 \mu\text{m}$ found in the literature [76].

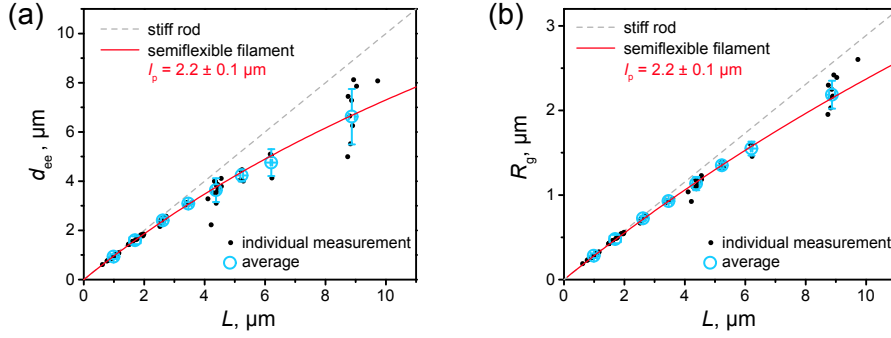


Figure 5.5: Stiffness of membrane adsorbed *fd*-virus particles. (a) End-to-end distance d_{ee} versus the determined virus length L . A fit to the WLC expression (red curve, Equation (1.35)) yields a persistence length $l_p = 2.2 \pm 0.1 \mu\text{m}$. (b) Radius of gyration R_g versus L . Fitting the data with the WLC expression (red curve, Equation (1.32)) gives a persistence length $l_p = 2.2 \pm 0.1 \mu\text{m}$. In both cases the stiff rod limit is indicated by a gray dashed line.

It is apparent from Figure 5.5 that virus monomers and dimers $[fd]_1$ and $[fd]_2$ can be considered as stiff rods, because their end-to-end distance and radius of gyration only deviate from the corresponding asymptotic dependences by less than 2 %. As a result, in the further analysis these virus particles will be considered as rod-like with the contour lengths $L_0 = 0.88 \mu\text{m}$ and $2L_0 = 1.56 \mu\text{m}$ and radii of gyration of $L_0/\sqrt{12} = 0.25 \mu\text{m}$ and $2L_0/\sqrt{12} = 0.51 \mu\text{m}$.

On the other hand, trimers $[fd]_3$ and higher order multimers exhibit considerable shape undulations. Therefore, the gyration radii of $[fd]_m$, $m \geq 3$, were determined from the contour analysis as described in Section 2.4.3.

5.3. Brownian motion of membrane-bound semiflexible DNA molecules in the random coil conformation

Random-coil DNA molecules, which are adsorbed to a freestanding fluid membrane with low cationic lipid fractions (DOPC/DOTAP 99:1), can be described as a 2D semiflexible polymer with the persistence length $l_p = 0.26 \pm 0.04 \mu\text{m}$ (see Section 5.2.1). Therefore, the shortest DNA fragment (5 kbp) has a ratio of the contour length and the persistence length $L/l_p \approx 8.5$, and for the longer λ -DNA $L/l_p \approx 82$. This means that the membrane-adsorbed DNA molecules are comparatively flexible.

The rotational and translational diffusion coefficients D_R and D_T of these random-coil DNA molecules with lengths of 5, 10, 20, and 48.5 kbp, which are adsorbed to a freestanding lipid membrane, show a size dependence on the radius of gyration that is expected in the transition regime from the bulk-viscosity-dominated diffusion, with a dependence on the molecule size similar to that for free diffusion in bulk solution, to a membrane-viscosity-dominated diffusion, with a weaker size dependence (Figure 5.6).

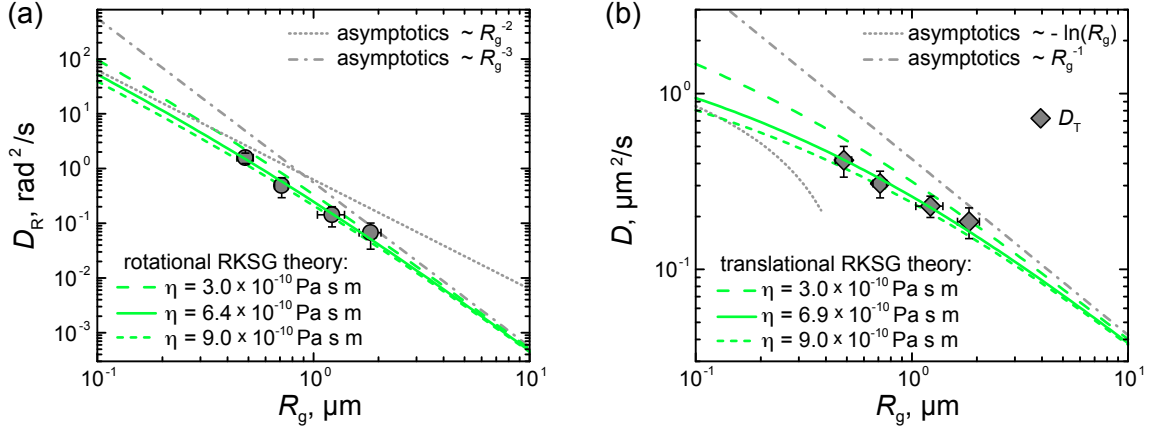


Figure 5.6: Translational and rotational diffusion of DNA random coils adsorbed to a freestanding cationic DOPC/DOTAP 99:1 membrane. (a) Rotational diffusion coefficient D_R versus radius of gyration R_g of the DNA coil. A fit to the RKSG theory yields a membrane surface viscosity $\eta = (6.4 \pm 1.9) \times 10^{-10}$ Pa s m. (b) Translational diffusion coefficient D_T versus radius of gyration R_g . A fit to the RKSG theory yields a membrane surface viscosity $\eta = (6.9 \pm 1.2) \times 10^{-10}$ Pa s m. Temperature: 24 °C.

The freestanding DOPC/DOTAP 99:1 membrane, to which the DNA is attached, was already well characterized in Section 3.2.3, and its membrane surface viscosity was found to be $\eta = (5.9 \pm 0.2) \times 10^{-10}$ Pa s m. The bulk viscosity of the surrounding water is also known, $\mu = 0.91 \times 10^{-3}$ Pa s at 24 °C (see Section 3.2.2, [136]). The resulting Saffman–Delbrück length for a freestanding DOPC/DOTAP 99:1 membrane is therefore $l_{SD} = 324$ nm. With radii of gyration of order of l_{SD} and larger, the effects of the transition from membrane-dominated diffusion to bulk-dominated diffusion are indeed expected to be observed in this case (see Section 1.4).

Recently, Ramachandran, Komura, Seki and Gompper (RKSG) developed a hydrodynamic-based theory for translational diffusion and conformational dynamics of a Gaussian polymer chain in a viscous membrane [62]. One can obtain the rotational diffusion coefficients using their expression for the longest conformational relaxation time (see Section 1.3.2). Therefore, it is interesting to compare rotational and translational diffusion coefficients for the relatively flexible membrane-bound DNA molecules with the expectations of the RKSG theory.

Indeed, our experimental data are well described by the RKSG theory: a least squares fitting of the data using the RKSG theory for rotational diffusion (Equation (1.39)) and translational diffusion (Equation (1.38)) yields the membrane surface viscosities $\eta = (6.4 \pm 1.9) \times 10^{-10}$ Pa s m and $\eta = (6.9 \pm 1.2) \times 10^{-10}$ Pa s m, respectively. These membrane viscosities are in a very good agreement with the previously determined value of $\eta = (5.9 \pm 0.2) \times 10^{-10}$ Pa s m. To illustrate the influence of the membrane viscosity on the diffusion coefficients of membrane-adsorbed polymers in the RKSG theory, additional curves for $\eta = 3 \times 10^{-10}$ Pa s m and $\eta = 9 \times 10^{-10}$ Pa s m are shown in Figure 5.6.

This allows us to conclude that the RKSG theory can be successfully applied to quantitatively describe the translational and rotational diffusion coefficients of semiflexible polymers which are adsorbed to a freestanding fluid lipid membrane for L/l_p ratios down to 8.5. This is a remarkable finding, as the RKSG theory is originally designed to describe flexible Gaussian-chain polymers.

A comparison of our results for the rotational and translational diffusion coefficients of random-coil DNA molecules on a freestanding lipid membrane (Figure 5.6) to the values for the diffusion coefficients reported for DNA molecules of similar length but adsorbed to a supported lipid bilayer [8, 9] shows a striking difference: λ -DNA molecules on a freestanding lipid membrane show a ~ 100 times faster translational diffusion and a ~ 400 times faster rotational diffusion than λ -DNA molecules adsorbed to a supported lipid membrane [8, 9]. This shows once again the significant differences between experiments with freestanding and supported lipid membranes.

5.4. Brownian motion of membrane-bound semiflexible *fd*-virus particles – Transition from semiflexible filament to stiff rod

We found that *fd*-virus particles which are adsorbed to a freestanding fluid cationic lipid membrane with a DOPC/DOTAP 99:1 composition behave as semiflexible filaments in 2D with the persistence of $l_p = 2.2 \pm 0.1 \mu\text{m}$ (see Section 5.2.2). The contour length of membrane-bound *fd*-virus particles lies in the range of 0.88–9.68 μm . Therefore, L/l_p ranges from 0.4 for $[fd]_1$ to 4.4 for the longest observed filament $[fd]_{11}$ and covers the transition from a straight stiff rod to a thermally fluctuating semiflexible filament. At the same time, the reduced radius of gyration $\epsilon = R_g/l_{SD}$ ranges from 0.8 to 8, if one assumes the membrane surface viscosity of $5.9 \times 10^{-10} \text{ Pa s m}$ and $l_{SD} = 324 \text{ nm}$. Therefore, the contour length dependence of the diffusion coefficients of *fd*-virus particles should exhibit two crossovers. On the one hand, the crossover from the membrane-dominated drag for the short filaments ($L < l_{SD}$) to bulk-controlled drag for the long filaments ($L > l_{SD}$) is expected. On the other hand, the crossover in the conformation from the stiff rod ($L < l_p$) to semiflexible filament ($L > l_p$) in case $L \gtrsim l_{SD}$ should affect the size dependence of the diffusion coefficients as well.

For membrane-adsorbed *fd*-virus particles we obtain the rotational diffusion coefficient D_R and the two-dimensional translational diffusion coefficient D_T , and in addition the translational diffusion coefficients D_{\parallel} and D_{\perp} for motion parallel and perpendicular to the particle orientation, whose difference reflects the significant anisotropy in the hydrodynamic drag caused by the highly anisotropic shape of the *fd*-virus particles (Figure 5.7). The rotational diffusion coefficient and the translational diffusion coefficients depend on the particle size expressed by its radius of gyration in a similar fashion as it was observed for membrane-bound DNA in Section 5.3.

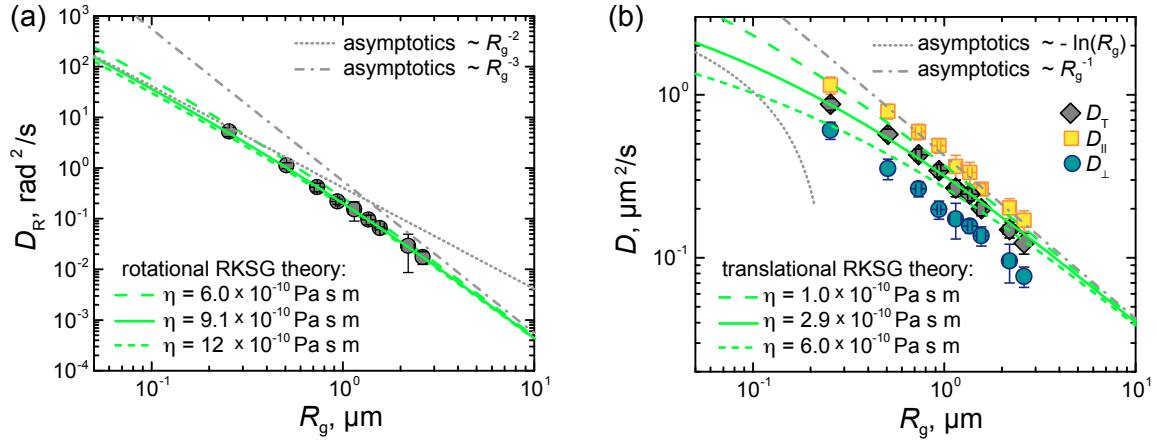


Figure 5.7: Rotational and translational diffusion *fd*-virus particles adsorbed to a freestanding DOPC/DOTAP 99:1 bilayer analyzed using the RKSG theory. (a) Rotational diffusion coefficient D_R versus radius of gyration R_g . Using the RKSG theory the data are best fit if the membrane surface viscosity is $\eta = 9.1 \times 10^{-10}$ Pa s m. (b) Translational diffusion coefficient $D_{||}$ and D_{\perp} and their arithmetic mean D_T versus radius of gyration R_g . Using the RKSG theory D_T is best described if the membrane surface viscosity is $\eta = 2.9 \times 10^{-10}$ Pa s m.

Given the success of the RKSG theory (see Section 1.3.2) in describing the translational and rotational diffusion coefficients of membrane-adsorbed semiflexible random coil DNA molecules even down to $L/l_p = 8.5$ (Section 5.3), one can try to apply the RKSG theory to the diffusion coefficients D_R and D_T obtained for the stiffer *fd*-virus particles as well, keeping in mind it might not be fully applicable in this case.

The size dependence of translational and rotational diffusion coefficients of membrane-bound *fd*-virus particles can be described surprisingly well using the RKSG theory. However, the membrane surface viscosities required for the RKSG theory to quantitatively describe the experimental data deviate from the expected value of $\eta = 5.9 \times 10^{-10}$ Pa s m (see Section 3.2.3). For rotational diffusion the quantitative description by the RKSG theory (Expression (1.39)) requires a membrane surface viscosity $\eta = 9.1 \times 10^{-10}$ Pa s m (Figure 5.7(a)), which is by a factor of about 1.5 higher than the expected value. For translational diffusion the quantitative description by the RKSG theory (Expression (1.39)) requires a membrane surface viscosity $\eta = 2.9 \times 10^{-10}$ Pa s m (Figure 5.7(b)), which is by a factor of about 2 lower than the expected value. These deviations from the expected membrane surface viscosity show that, as expected, the RKSG theory designed for a flexible Gaussian chain does not allow for an entirely correct quantitative description of the diffusion coefficients of stiff membrane-adsorbed particles. However, the deviations by only a factor not exceeding 2 between the RKSG predictions and the expectations are surprisingly small, taking into account that *fd*-virus particles are by far not a flexible Gaussian polymer.

In order to test the limits of the ability of the RKSG theory to describe the behavior of semiflexible particles adsorbed to a lipid membrane, the experimentally obtained diffusion

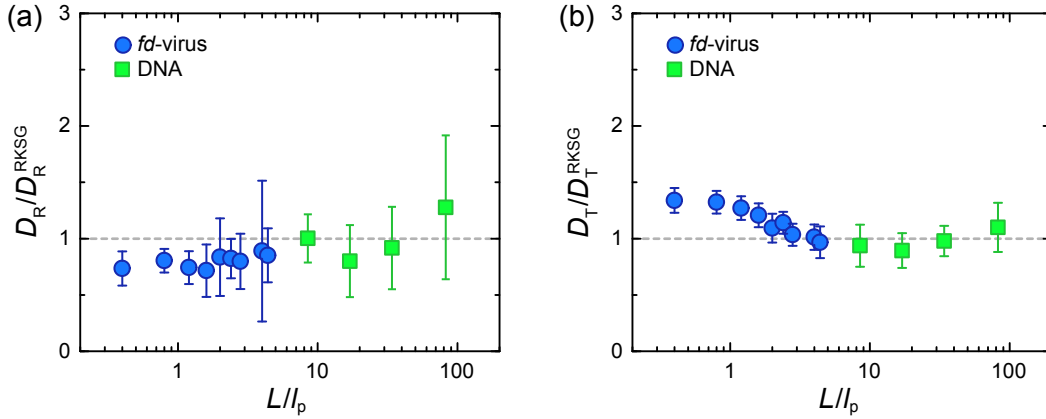


Figure 5.8: Limits of the RKSG theory. (a) Rotational diffusion coefficient D_R of membrane-adsorbed *fd*-virus particles (blue circles) and DNA random coils (green squares) normalized by the expectations according to RKSG for $\eta = 5.9 \times 10^{-10}$ Pa s m and plotted against the ratio of filament length L and filament persistence length l_p . (b) Translational diffusion coefficient D_T of membrane-adsorbed *fd*-virus particles (blue circles) and DNA random coils (green squares) normalized by the expectations according to RKSG for $\eta = 5.9 \times 10^{-10}$ Pa s m and plotted against L/l_p .

coefficients D_R and D_T of both membrane adsorbed *fd*-virus particles and DNA random coils were normalized by the predictions of RKSG for a membrane with the expected viscosity $\eta = 5.9 \times 10^{-10}$ Pa s m and plotted versus the ratio L/l_p in Figure 5.8. For the rotational diffusion the experimental data agree with the predictions by the RKSG theory down to $L/l_p \approx 7$ (Figure 5.8(a)). The translational diffusion is apparently even less sensitive to the influence of the more rod-like conformation of the shorter filaments, and in this case the predictions by RKSG are met down to surprisingly low ratios of $L/l_p \approx 3$ (Figure 5.8(b)).

In the very stiff regime, where the RKSG theory is not applicable anymore, the theories by Levine, Liverpool and MacKintosh [63, 64] and Fischer [65, 66] for needle-like objects which exhibit 2D Brownian motion in a thin viscous film are expected to predict the rotational diffusion coefficients D_R and the rotational diffusion coefficients parallel and perpendicular to the particle orientation (D_{\parallel} and D_{\perp}) for the membrane-bound *fd*-virus particles (see Section 1.3.2). Especially this should be the case for the two shortest *fd*-virus particles $[fd]_1$ and $[fd]_2$, which behave as stiff rods. Both these virus particles have a contour length L considerably shorter than the *fd*-virus persistence length $l_p = 2.2 \pm 0.1$ μm . With the ratios of the filament length to its diameter of 133 for $[fd]_1$ and 167 for $[fd]_2$, they match the conditions of a thin needle-like object, assumed by the LLM and Fischer theories.

Much to our surprise, the rotational diffusion coefficient D_R , as well as the translational diffusion coefficients D_{\parallel} and D_{\perp} of the membrane-bound *fd*-virus particles can only be quantitatively described by the LLM and Fischer theories if their predictions for D_R , D_{\parallel} and D_{\perp} are multiplied by a constant prefactor of about 1.5 in all cases. At the moment the reason for

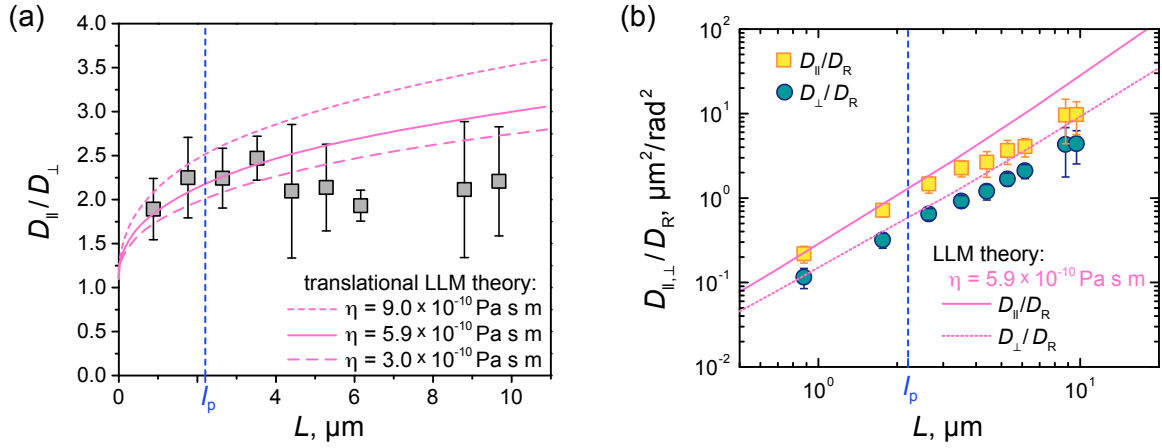


Figure 5.9: Diffusion of *fd*-virus particles adsorbed to a freestanding DOPC/DOTAP 99:1 bilayer surrounded by water. (a) Ratio of translational diffusion coefficients D_{\parallel}/D_{\perp} versus the contour length L and theoretical expectations for different membrane surface viscosities in the stiff rod limit. (b) Ratio of translational and rotational diffusion coefficients D_{\parallel}/D_R and D_{\perp}/D_R versus L and theoretical expectations for a membrane surface viscosity $\eta = 5.9 \times 10^{-10} \text{ Pa s m}$ in the stiff rod limit. Because no closed-form theoretical expression for the diffusion coefficients of stiff rods of arbitrary length is given, the curves according to LLM were digitized from figures in reference [64].

this is unclear.

Therefore, the ratios D_{\parallel}/D_{\perp} as well as D_{\parallel}/D_R and D_{\perp}/D_R are investigated in the following, as a constant prefactor is canceled out in these ratios.

The LLM and Fischer theories predict a progressively growing difference between D_{\parallel} and D_{\perp} with growing filament length (see Section 1.3.2).

Indeed, a growing difference between D_{\parallel} and D_{\perp} with growing virus length and thus the growth of the ratio D_{\parallel}/D_{\perp} is observed for membrane-bound virus particles $[fd]_1$ up to $[fd]_4$ (Figure 5.9(a)). The value of the ratio perfectly matches the theoretical predictions by LLM up to $L/l_p \lesssim 2$, if a membrane with the surface viscosity of $5.9 \times 10^{-10} \text{ Pa s m}$ is assumed, as indicated by the solid curve in Figure 5.9(a). To illustrate how a different membrane viscosity is expected to change the values of the ratio D_{\parallel}/D_{\perp} , the corresponding curves for $\eta = 3 \times 10^{-10} \text{ Pa s m}$ and $\eta = 9 \times 10^{-10} \text{ Pa s m}$ are shown in Figure 5.9(a) as well. With stronger deviations from the stiff-rod conformation for longer filaments, the ratio deviates from the expectations for a stiff rod and stays around a constant value of approximately two.

When the ratios of the lateral diffusion coefficients and the rotational diffusion coefficient, D_{\parallel}/D_R and D_{\perp}/D_R , are investigated (Figure 5.9(b)) one observes that at $\eta = 5.9 \times 10^{-10} \text{ Pa s m}$ the behavior of the shortest virus $[fd]_1$ is well described by the LLM theory, but the experimental data start to deviate from the theoretical expectations already for $[fd]_2$, i. e. earlier than for the translational diffusion coefficients. This again points to a higher sensitivity of the rotational diffusion to the conformation of a particle compared to the translational diffusion. This also means that the LLM theory as applied to the rotational

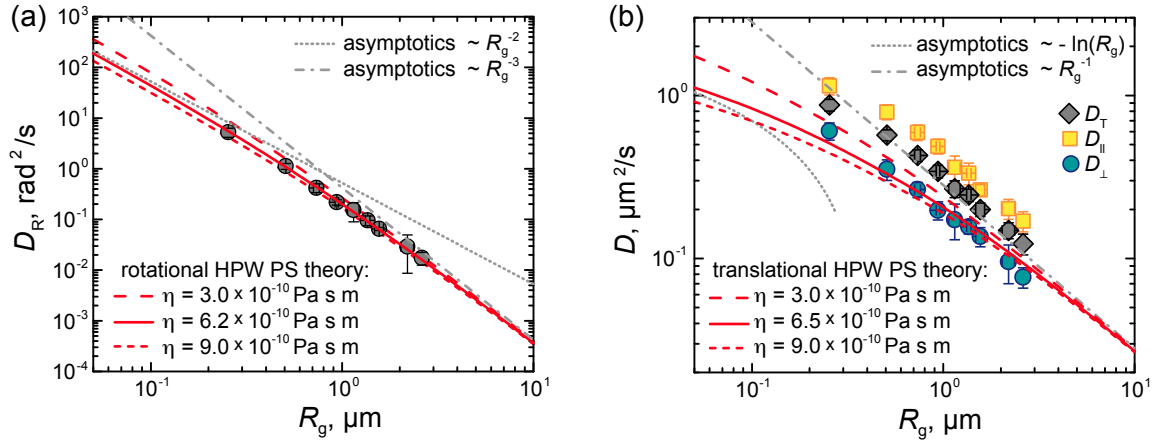


Figure 5.10: Rotational and translational diffusion *fd*-virus particles adsorbed to a freestanding DOPC/DOTAP 99:1 bilayer analyzed using the HPW PS theory. (a) Rotational diffusion coefficient D_R versus radius of gyration R_g . Using the HPW PS theory the data are best fit if the membrane surface viscosity is $\eta = (6.3 \pm 0.7) \times 10^{-10}$ Pa s m. (b) Translational diffusion coefficient $D_{||}$ and D_{\perp} and their arithmetic mean D_T versus radius of gyration R_g . Using the HPW theory D_{\perp} is best described if the membrane surface viscosity is $\eta = (6.5 \pm 1.1) \times 10^{-10}$ Pa s m.

diffusion is only applicable for $L/l_p \lesssim 0.4$.

The rotational and translational diffusion coefficients of *fd*-virus particles adsorbed to a freestanding cationic membrane, cannot be quantitatively described over the complete range of particle sizes by either the theories by LLM and Fischer for a stiff rod or by the RKSG theory for a flexible 2D Gaussian chain. However, a transition from the membrane-dominated diffusion to bulk-dominated diffusion with growing *fd*-virus lengths is clearly observed.

In Section 1.3.2 it was discussed that for both asymptotics $\epsilon \gg 1$ and $\epsilon \ll 1$ the rotational diffusion of stiff straight rods and Gaussian chain polymers can be described by the Hughes, Pailthorpe and White theory [53] for a cylindrical membrane inclusion of radius a , which deviate only by about 20 % from the radius of gyration of the respective filaments: in the rigid rod limit $a \approx 1.2R_g$, and in the Gaussian chain limit $a \approx 0.9R_g$. For this reason the transition region from a stiff rod to a Gaussian chain may be well described by the HPW theory for a rigid disk-like particle with the characteristic size $0.9R_g < a < 1.2R_g$. Therefore, for simplicity we can choose $a = R_g$. Making use of the closed-form approximation for the rotational HPW theory [55] (Expression (1.18), HPW PS) one finds that the rotational diffusion of *fd*-virus filaments adsorbed to a freestanding cationic membrane is indeed well described by this theory (Figure 5.10(a)). A least squares fit yields $\eta = (6.2 \pm 0.7) \times 10^{-10}$ Pa s m, which is in perfect agreement with the expected value of $(5.9 \pm 0.2) \times 10^{-10}$ Pa s m.

A similar argument can be made for the translational diffusion coefficient D_{\perp} for motion perpendicular to the long axis of the filament. According to the results of the LLM and Fischer theories, it can be described by rescaling the expressions of the HPW theory (see

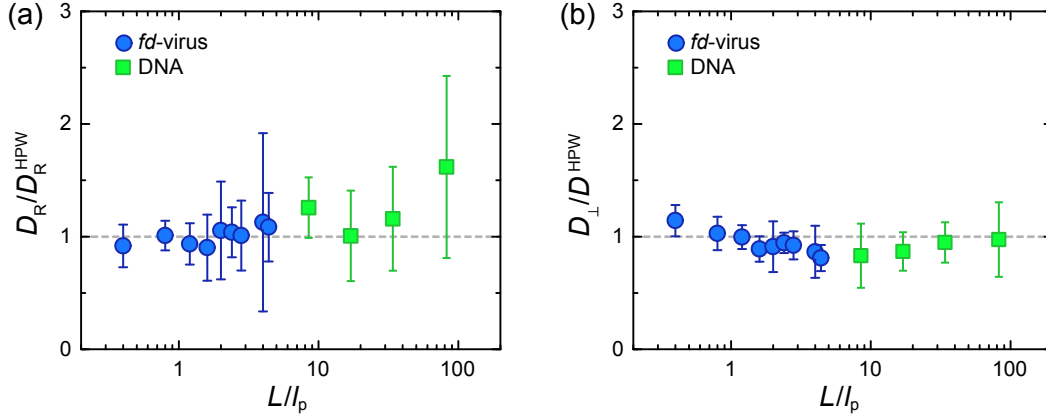


Figure 5.11: Limits of the HPW theory. (a) Rotational diffusion coefficient D_R of membrane-adsorbed *fd*-virus particles (blue circles) and DNA random coils (green squares) normalized by the expectations according to HPW PS for $\eta = 5.9 \times 10^{-10}$ Pa s m and plotted against the ratio of contour length L and filament persistence length l_p . (b) Translational diffusion coefficient perpendicular to the long axis of the filament D_{\perp} of membrane-adsorbed *fd*-virus particles (blue circles) and DNA random coils (green squares) normalized by the expectations according to HPW PS for $\eta = 5.9 \times 10^{-10}$ Pa s m and plotted against L/l_p .

Section 1.3.2).² Indeed, D_{\perp} of membrane-adsorbed *fd*-virus is reasonably well described by the closed-form approximation of the translational HPW theory [54] (Expression (1.16), HPW PS) and the fit yields $\eta = (6.5 \pm 1.1) \times 10^{-10}$ Pa s m. However, it appears that the diffusion coefficients of the shortest *fd* filaments are slightly underestimated and for the longest *fd* filaments are slightly overestimated by the HPW theory.

In order to test the limits of the ability of the HPW theory with $a = R_g$ to describe the diffusion of semiflexible particles adsorbed to a lipid membrane, the experimentally obtained diffusion coefficients D_R and D_{\perp} of both membrane adsorbed *fd*-virus particles and DNA random coils were normalized by the predictions of HPW PS for a membrane with the expected viscosity $\eta = 5.9 \times 10^{-10}$ Pa s m and plotted versus the ratio L/l_p in Figure 5.11.

The rotational diffusion coefficients of membrane-adsorbed semiflexible particles are well described by the HPW PS theory within a broad range of L/l_p , which includes the rotational diffusion coefficients of all observed *fd*-virus particles. Only at $L/l_p \gtrsim 8$ the rotational diffusion coefficients obtained for membrane-adsorbed DNA molecules deviate systematically from the theoretical predictions according to HPW PS (Figure 5.11(a)).

For the translational diffusion coefficients D_{\perp} of membrane-adsorbed semiflexible particles we find that the HPW PS theory is able to describe well the translational diffusion for $0.8 \lesssim L/l_p \lesssim 3$ and for $L/l_p \gtrsim 30$, but shows considerable deviations outside these ranges (Figure 5.11(b)).

In essence, our results for diffusion of membrane-attached semiflexible particles and the

²This is not the case for the translational diffusion coefficient D_{\parallel} for motion parallel to the particle orientation, which scales differently than the HPW theory in case $\epsilon \gg 1$ (see Section 1.3.2).

discussion of the hydrodynamics-based theories in Section 1.3.2 show that rotational diffusion coefficient and the translational diffusion coefficient for motion perpendicular to the particle orientation can be successfully predicted by the HPW theory for cylindrical membrane inclusions with a characteristic size that is approximately equal to the radius of gyration of the particle.

5.5. Conclusion

To conclude, we find that DNA macromolecules and *fd*-virus particles adsorbed to a free-standing cationic membrane with low cationic lipid content (DOPC/DOTAP 99:1) behave as semiflexible filaments in 2D with a persistence length of 260 nm in case of DNA, and 2.2 μm in case of *fd*-virus particles. The results obtained for DNA are successfully explained by strong electrostatic interactions which significantly stiffen DNA molecules adsorbed to the freestanding membrane with low charge density.

We find that membrane-adsorbed DNA molecules and *fd*-virus particles show a diffusion behavior which is influenced by the viscous membrane in agreement with the hydrodynamics-based theories which describe the diffusion of membrane inclusions. For a quantitative description of the rotational and translational diffusion coefficients of the semiflexible DNA molecules and *fd*-virus particles, which are electrostatically adsorbed to a freestanding cationic DOPC/DOTAP 99:1 bilayer, we test the applicability of hydrodynamics-based theories.

The RKSG theory [62], which was developed for a 2D Gaussian polymer chain in a membrane, can correctly predict the translational diffusion coefficients of filamentous semiflexible particles adsorbed to a membrane for $L/l_p \gtrsim 3$. Rotational diffusion was found to be more sensitive to the particle conformation, and in this case the applicability range of the RKSG theory shifts to longer contour lengths $L/l_p \gtrsim 7$.

The LLM [63, 64] and Fischer [65, 66] theories, which were developed for stiff rods in a thin viscous membrane, can predict the ratio of the translational diffusion coefficients for motion parallel and perpendicular to the membrane-adsorbed semiflexible particle for $L/l_p \lesssim 1.5$ and the ratios of the translational diffusion coefficients and the rotational diffusion coefficient for $L/l_p \lesssim 0.4$. However, these theories fail to predict the absolute values of the diffusion coefficients unless their predictions for the diffusion coefficients are multiplied by a constant prefactor of about 1.5.

Remarkably, the HPW PS theory for a disk-shaped solid membrane inclusion with the characteristic size equal to the radius of gyration of the particle is able to predict the rotational diffusion coefficients of semiflexible particles in the range of $L/l_p \approx 0.4\text{--}4.4$ and the translational diffusion coefficients for motion perpendicular to the filament in the range of $L/l_p \approx 0.8\text{--}3$ and $L/l_p \gtrsim 30$.

Appendix

A.1. Simulation of image acquisition for diffusion of *fd*-virus particles

When evaluating the translational diffusion coefficients obtained in the experiment of membrane-adsorbed *fd*-virus particles, a problematic deviation of nearly five percent from the expectations in the ratio $(\hat{D}_{\parallel} + \hat{D}_{\perp})/(2D_{\text{T}}) = 1$ was found for the shortest and thus fastest moving $[fd]_1$ virus (Figure A.1(a)). By definition, the translational diffusion coefficient D_{T} obtained from the analysis of the MSD of two-dimensional diffusion of the center of mass must be equal to the arithmetic mean of the diffusion coefficients \hat{D}_{\parallel} and \hat{D}_{\perp} obtained from the analysis of the diffusion parallel and perpendicular to the long axis of the elongated particle in its own system of coordinates (for details see Section 2.4.7). A systematic deviation from this relation points to a problem in the determination of at least one of the translational diffusion coefficients mentioned above.

At this point the reader shall be reminded of the fact that a deviation of the experimentally determined values of \hat{D}_{\parallel} and \hat{D}_{\perp} from the diffusion coefficients D_{\parallel} and D_{\perp} , which reflect the correct anisotropy in the drag for translational motion parallel and perpendicular to the elongated particle, is expected if the time interval between the consecutive images Δt is of order of or larger than $1/D_{\text{R}}$. The reason for that is found in a change of orientation for fast rotating particles between consecutive recorded images. This is discussed in detail in Section 2.4.7 and can be accounted for by a suitable correction, if D_{T} , D_{R} and the frame time Δt are known. However, the arithmetic mean of D_{\parallel} and D_{\perp} , as well as \hat{D}_{\parallel} and \hat{D}_{\perp} must always be equal to D_{T} irrespectively of whether the correction is introduced or not.

Notice that all the above reasoning is developed for the situation corresponding to the infinitely short image acquisition time, when the motion blur of the object does not play any role. It was concluded that most likely, the problem resided in a combination of a finite exposure time and fast motion of the $[fd]_1$ particles. To verify this, a series of simulations was carried out. Movies of *fd*-virus monomers, dimers and trimers with the respective filament

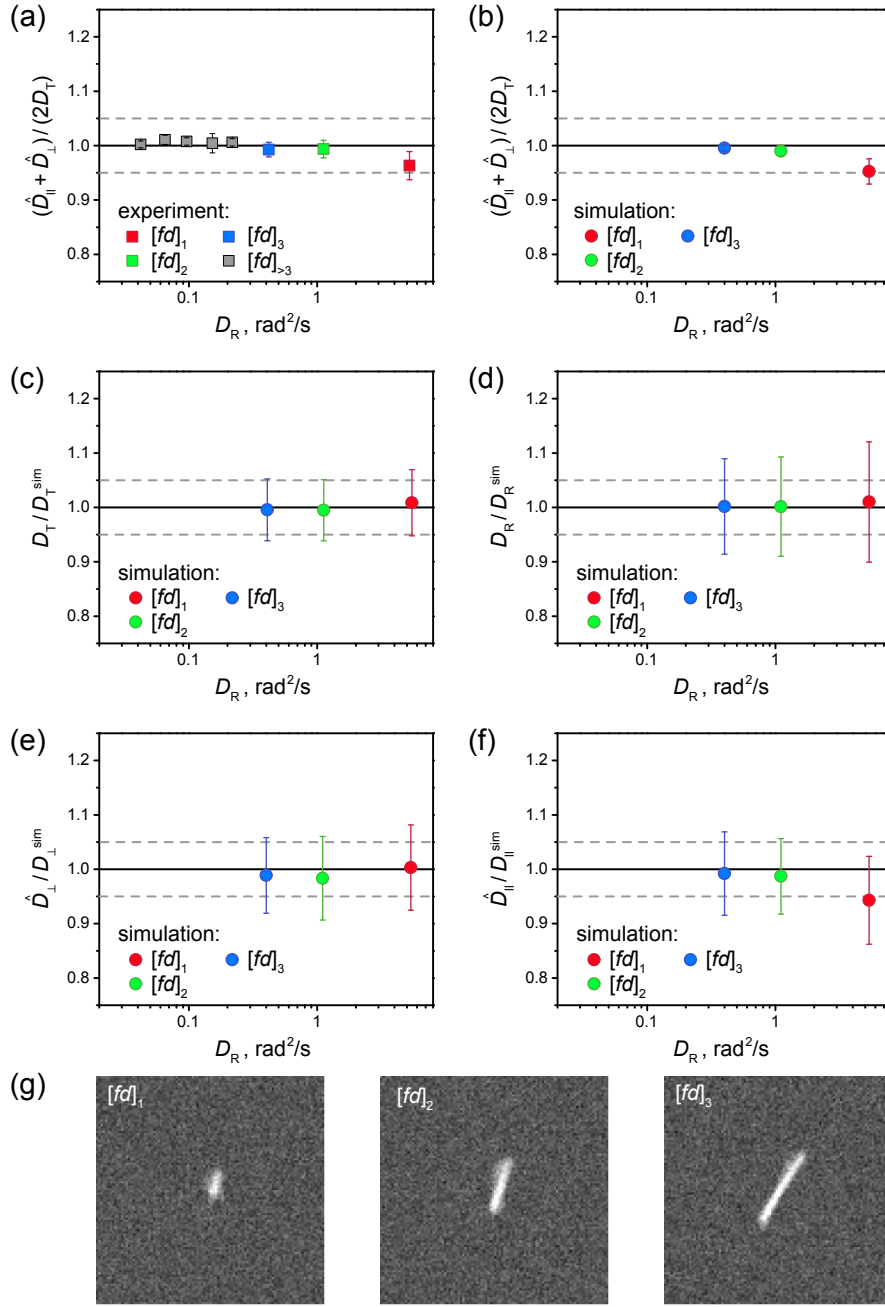


Figure A.1: Simulation of the diffusion of membrane-adsorbed fd -viruses and comparison to experiment in order to investigate potential systematic errors in the determination of diffusion coefficients. (a) Ratio $(\hat{D}_{\parallel} + \hat{D}_{\perp}) / (2D_T)$ plotted versus D_R for diffusion coefficients obtained from experiments. (b)–(f) Ratio of diffusion coefficients from the analysis of simulated movies of $[fd]_1$, $[fd]_2$ and $[fd]_3$ with diffusion coefficients and properties similar to those obtained in the experiment. Frame time $\Delta t = 32$ ms. Simulated image acquisition time 30 ms. (g) Typical simulated images of $[fd]_1$, $[fd]_2$ and $[fd]_3$.

length, diffusion coefficients, lateral resolution and time resolution as in the experiment were created. For every particle length 100 movies each consisting of 1000 images were simulated

and analyzed.

If the image acquisition time was not accounted for in the simulations, which means no motion blur was introduced, the relationship $(\hat{D}_{\parallel} + \hat{D}_{\perp})/(2D_{\text{T}}) = 1$ was recovered correctly, with the expected deviations of \hat{D}_{\parallel} and \hat{D}_{\perp} from $D_{\parallel}^{\text{sim}}$ and D_{\perp}^{sim} (similar to Figure 2.16(b) in Section 2.4.7).

A different picture was obtained if a finite image acquisition time of 30 ms, similar to the one used in our experiments, was included in the simulations. Illustrative examples of simulated images for $[fd]_1$, $[fd]_2$ and $[fd]_3$ with motion blur due to the image acquisition time are shown in Figure A.1(g). In this case, the ratio of the obtained translational diffusion coefficients $(\hat{D}_{\parallel} + \hat{D}_{\perp})/(2D_{\text{T}})$ shows the same systematic deviation for the fast rotating monomer as in the experiment (see Figure A.1(b)).

A more detailed investigation of the analyzed simulation data reveals that the two-dimensional translational diffusion coefficient $D_{\text{T}}^{\text{sim}}$ and the rotational diffusion coefficient $D_{\text{R}}^{\text{sim}}$ are recovered correctly for all considered virus lengths (Figure A.1(c,d)).

Surprisingly, also the obtained perpendicular diffusion coefficient \hat{D}_{\perp} matches the value of the simulated diffusion coefficient D_{\perp}^{sim} (Figure A.1(e)). In fact, a 13 % larger value of \hat{D}_{\perp} compared to D_{\perp}^{sim} is expected according to Equation (2.40) for $[fd]_1$ with the given diffusion coefficients $D_{\perp}^{\text{sim}} = 0.6 \mu\text{m}^2/\text{s}$, $D_{\parallel}^{\text{sim}} = 1.15 \mu\text{m}^2/\text{s}$, $D_{\text{R}}^{\text{sim}} = 5.3 \text{ rad}^2/\text{s}$ and a frame time $\Delta t = 32 \text{ ms}$. This means that \hat{D}_{\perp} is underestimated as a result of the presence of the motion blur. In this case, applying the correction according to Equation (2.41), which assumes infinitely short image acquisition times, would result in a large systematic error of about 10 % for D_{\perp} .

The determined values of \hat{D}_{\parallel} , on the other hand, agree well with the expected deviations from $D_{\parallel}^{\text{sim}}$ due to rotation and limited time resolution (Figure A.1(e)).

An ad-hoc solution to the problem with the diffusion data of the $[fd]_1$ particles is to assume $D_{\perp} = \hat{D}_{\perp}$ without any correction. This assumption is backed by the simulation of *fd*-virus diffusion and holds within a less than 2 % error, when employing the relevant experimental conditions (Figure A.1(e)). With the known D_{\perp} and D_{T} , one can calculate D_{\parallel} using the relation $D_{\parallel} = 2D_{\text{T}} - D_{\perp}$.

List of Abbreviations

A	adenine
AFM	atomic force microscopy
AOTF	acousto-optic tunable filter
ATP	adenosine-5'-triphosphate
BLB	black lipid bilayer
C	cytosine
CCD	charge-coupled device
COI	center of intensity
dd-H ₂ O	double distilled water
DiD	1,1-dioctadecyl-3,3,3,3-tetramethylindodicarbocyanine
DMPC	1,2-dimyristoyl-sn-glycero-3-phosphocholine
DMTAP	1,2-dimyristoyl-3-trime-thylammonium-propane
DNA	deoxyribonucleic acid
DOPC	1,2-dioleoyl-sn-glycero-3-phosphocholine
DOTAP	1,2-dioleoyl-3-trimethylammonium-propane
ds-DNA	double-stranded DNA
DSPC	1,2-Distearoyl-sn-glycero-3-phosphocholine
EDOPC	1,2-dioleoyl-sn-glycero-3-ethylphosphocholine
EMCCD	electron-multiplying charge-coupled device
FWHM	full width at half maximum

G	guanine
GUV	giant unilamellar vesicles
HPW	Hughes, Pailthorpe and White; hydrodynamic theory for cylindrical membrane inclusions
HPW PS	Petrov and Schwille; closed-form approximation of HPW theory
IQR	interquartile range
ITO	indium-tin oxide
LLM	Levine, Liverpool and MacKintosh; hydrodynamic theory for needle-like membrane inclusions
LUV	large unilamellar vesicles
MSD	mean squared displacement
PBS	phosphate buffered saline
PS	phosphatidylserine
PSF	point spread function
RKSG	Ramachandran, Komura, Seki and Gompper; hydrodynamic theory for Gaussian chain membrane inclusions
ROI	region of interest
SD	Saffman and Delbrück
SGUV	supergiant unilamellar vesicles
SLB	supported lipid bilayer
SUV	small unilamellar vesicles
T	thymine
TAP	cationic trimethylammoniumpropane
TEM	transmission electron microscopy
TIRF	total internal reflection fluorescence
WLC	worm like chain

Bibliography

- [1] J. Käs, H. Strey, and E. Sackmann. Direct imaging of reptation for semiflexible actin filaments. *Nature*, 368:226–229, 1994.
- [2] J. Käs, H. Strey, J. X. Tang, D. Finger, R. Ezzell, E. Sackmann, and P. A. Janmey. F-actin, a model polymer for semiflexible chains in dilute, semidilute, and liquid crystalline solutions. *Biophys. J.*, 70:609–625, 1996.
- [3] F. Gittes, B. Mickey, J. Nettleton, and J. Howard. Flexural rigidity of microtubules and actin-filaments measured from thermal fluctuations in shape. *J. Cell Biol.*, 120:923–934, 1993.
- [4] D. Valdman, P. J. Atzberger, D. Yu, S. Kuei, and M. T. Valentine. Spectral analysis methods for the robust measurement of the flexural rigidity of biopolymers. *Biophys. J.*, 102:1144–1153, 2012.
- [5] C. Bustamante, J. F. Marko, E. D. Siggia, and S. Smith. Entropic elasticity of lambda-DNA. *Science*, 265:1599–1600, 1994.
- [6] S. C. Bae and S. Granick. Molecular motion at soft and hard interfaces: from phospholipid bilayers to polymers and lubricants. *Annu. Rev. Phys. Chem.*, 58:353–374, 2007.
- [7] M. Tanaka and E. Sackmann. Polymer-supported membranes as models of the cell surface. *Nature*, 437:656–663, 2005.
- [8] B. Maier and J. O. Rädler. Conformation and self-diffusion of single DNA molecules confined to two dimensions. *Phys. Rev. Lett.*, 82:1911–1914, 1999.
- [9] B. Maier and J. O. Rädler. DNA on fluid membranes: A model polymer in two dimensions. *Macromolecules*, 33:7185–7194, 2000.

- [10] C. Scomparin, S. Lecuyer, M. Ferreira, T. Charitat, and B. Tinland. Diffusion in supported lipid bilayers: influence of substrate and preparation technique on the internal dynamics. *Eur. Phys. J. E*, 28:211–220, 2009.
- [11] P. Walde, K. Cosentino, H. Engel, and P. Stano. Giant vesicles: preparations and applications. *ChemBioChem*, 11:848–865, 2010.
- [12] R. Lipowsky. The conformation of membranes. *Nature*, 349:475–481, 1991.
- [13] T. Heimburg. *Thermal Biophysics of Membranes*. Wiley-VCH, 2007.
- [14] S. Tristram-Nagle, Y. Liu, J. Legleiter, and J. F. Nagle. Structure of gel phase DMPC determined by X-ray diffraction. *Biophys. J.*, 83:3324–3335, 2002.
- [15] J. F. Nagle and S. Tristram-Nagle. Structure of lipid bilayers. *Biochim. Biophys. Acta*, 1469:159–195, 2000.
- [16] P. F. F. Almeida and W. L. C. Vaz. Lateral diffusion in membranes. In R. Lipowsky and E. Sackmann, editors, *Handbook of Biological Physics, Vol. I*. Elsevier Science B.V., 1995.
- [17] N. Kahya, D. Scherfeld, K. Bacia, B. Poolman, and P. Schwille. Probing lipid mobility of raft-exhibiting model membranes by fluorescence correlation spectroscopy. *J. Biol. Chem.*, 278:28109–28115, 2003.
- [18] R. Dimova, B. Pouligny, and C. Dietrich. Pretransitional effects in dimyristoylphosphatidylcholine vesicle membranes: optical dynamometry study. *Biophys. J.*, 79:340–356, 2000.
- [19] R. Lipowsky. Generic interactions of flexible membranes. In *Handbook of Biological Physics, Vol. 1*, pages 521–602. Elsevier Science B.V., 1995.
- [20] E. Evans and D. Needham. Physical properties of surfactant bilayer membranes: thermal transitions, elasticity, rigidity, cohesion and colloidal interactions. *J. Phys. Chem.*, 91:4219–4228, 1987.
- [21] P. B. Canham. The minimum energy of bending as a possible explanation of the biconcave shape of the human red blood cell. *J. Theor. Biol.*, 26:61–81, 1970.
- [22] W. Helfrich. Elastic properties of lipid bilayers: theory and possible experiments. *Z. Naturforsch. C*, 28:693–703, 1973.
- [23] E. A. Evans. Bending resistance and chemically induced moments in membrane bilayers. *Biophys. J.*, 14:923–931, 1974.

- [24] J. F. Faucon, M. D. Mitov, P. Méléard, I. Bivas, and P. Bothorel. Bending elasticity and thermal fluctuations of lipid membranes. Theoretical and experimental requirements. *J. Phys. France*, 50:2389–2414, 1989.
- [25] G. Niggemann, M. Kummrow, and W. Helfrich. The bending rigidity of phosphatidylcholine bilayers: dependences on experimental method, sample cell sealing and temperature. *J. Phys. II*, 5:413–425, 1995.
- [26] P. Méléard, C. Gerbeaud, T. Pott, L. Fernandez-Puente, I. Bivas, M. D. Mitov, J. Dufourcq, and P. Bothorel. Bending elasticities of model membranes: influences of temperature and sterol content. *Biophys. J.*, 72:2616–2629, 1997.
- [27] J. Henriksen, A. C. Rowat, and J. H. Ipsen. Vesicle fluctuation analysis of the effects of sterols on membrane bending rigidity. *Eur. Biophys. J.*, 33:732–741, 2004.
- [28] P. Schuille and S. Diez. Synthetic biology of minimal systems. *Crit. Rev. Biochem. Mol. Biol.*, 44:223–242, 2009.
- [29] M. Montal and P. Mueller. Formation of bimolecular membranes from lipid monolayers and a study of their electrical properties. *Proc. Natl. Acad. Sci. USA*, 69:3561–3566, 1972.
- [30] F. Heinemann and P. Schuille. Preparation of micrometer-sized free-standing membranes. *ChemPhysChem*, 12:2568–2571, 2011.
- [31] A. Sonnleitner, G. J. Schütz, and T. Schmidt. Free Brownian motion of individual lipid molecules in biomembranes. *Biophys. J.*, 77:2638–2642, 1999.
- [32] F. Tokumasu, A. J. Jin, G. W. Feigenson, and J. A. Dvorak. Atomic force microscopy of nanometric liposome adsorption and nanoscopic membrane domain formation. *Ultra-microscopy*, 97:217–227, 2003.
- [33] A. Charrier and F. Thibaudau. Main phase transitions in supported lipid single-bilayer. *Biophys. J.*, 89:1094–1101, 2005.
- [34] E. Sackmann. Supported membranes: scientific and practical applications. *Science*, 271:43–48, 1996.
- [35] A. Xie, R. Yamada, A. Gewirth, and S. Granick. Materials science of the gel to fluid phase transition in a supported phospholipid bilayer. *Phys. Rev. Lett.*, 89:246103, 2002.
- [36] Z. V. Leonenko, D. Merkle, S. P. Lees-Miller, and D. T. Cramb. Lipid phase dependence of DNA-cationic phospholipid bilayer interactions examined using atomic force microscopy. *Langmuir*, 18:4873–4884, 2002.

- [37] R. Brown. A brief account of microscopical observations made in the months of June, July and August 1827 on the particles contained in the pollen of plants. *Edinburgh New Phil. J.*, 5:358–371, 1828.
- [38] S. Chandrasekhar. Stochastic problems in physics and astronomy. *Rev. Mod. Phys.*, 15:1–89, 1943.
- [39] V. Vladimirov and Ya. Terletsky. Hydrodynamic theory of translational Brownian motion. *Zh. Eksp. Teor. Fiz.*, 15:258–263, 1945.
- [40] R. M. Mazo. *Brownian Motion. Fluctuations, Dynamics and Applications*. Oxford University Press, 2002.
- [41] A. Einstein. Über die von der molekularkinetischen Theorie der Wärme geforderte Bewegung von in ruhenden Flüssigkeiten suspendierten Teilchen. *Ann. Phys.*, 322:549–560, 1905.
- [42] J. Perrin. Mouvement brownien et réalité moléculaire. *Ann. Chim. Phys.*, 18:5–104, 1909.
- [43] M. von Smoluchowski. Zur kinetischen Theorie der Brownschen Molekularbewegung und der Suspensionen. *Ann. Phys.*, 326:756–780, 1906.
- [44] H. Qian, M. P. Sheetz, and E. L. Elson. Single particle tracking. Analysis of diffusion and flow in two-dimensional systems. *Biophys. J.*, 60:910–921, 1991.
- [45] A. Einstein. Zur Theorie der Brownschen Bewegung. *Ann. Phys.*, 324:371–381, 1906.
- [46] S. Childress. *An Introduction to Theoretical Fluid Mechanics*. American Mathematical Society, 2009.
- [47] P. G. Saffman and M. Delbrück. Brownian motion in biological membranes. *Proc. Natl. Acad. Sci. USA*, 72:3111–3113, 1975.
- [48] P. G. Saffman. Brownian motion in thin sheets of viscous fluid. *J. Fluid Mech.*, 73:593–602, 1976.
- [49] H. A. Stone. Interfaces: in fluid mechanics and across disciplines. *J. Fluid Mech.*, 645:1–25, 2010.
- [50] R. E. Waugh. Surface viscosity measurements from large bilayer vesicle tether formation. II. Experiments. *Biophys. J.*, 38:29–37, 1982.

- [51] J. Kriegsmann, I. Gregor, I. von der Hocht, J. Klare, M. Engelhard, J. Enderlein, and J. Fitter. Translational diffusion and interaction of a photoreceptor and its cognate transducer observed in giant unilamellar vesicles by using dual-focus FCS. *Chem-BioChem*, 10:1823–1829, 2009.
- [52] Y. Gambin, R. Lopez-Esparza, M. Reffay, E. Sierrecki, N. S. Gov, M. Genest, R. S. Hodges, and W. Urbach. Lateral mobility of proteins in liquid membranes revisited. *Proc. Natl. Acad. Sci. USA*, 103:2098–2102, 2006.
- [53] B. D. Hughes, B. A. Pailthorpe, and L. R. White. The translational and rotational drag on a cylinder moving in a membrane. *J. Fluid Mech.*, 110:349–372, 1981.
- [54] E. P. Petrov and P. Schwille. Translational diffusion in lipid membranes beyond the Saffman-Delbrück approximation. *Biophys. J.*, 94:L41–L43, 2008.
- [55] E. P. Petrov, R. Petrosyan, and P. Schwille. Translational and rotational diffusion of micrometer-sized solid domains in lipid membranes. *Soft Matter*, 8:7552–7555, 2012.
- [56] J. R. C. van der Maarel. *Introduction to Biopolymer Physics*. World Scientific, 2008.
- [57] O. Kratky and G. Porod. Röntgenuntersuchung gelöster Fadenmoleküle. *Rec. Trav. Chim.*, 68:1106–1122, 1949.
- [58] X. Liu and G. H. Pollack. Mechanics of F-actin characterized with microfabricated cantilevers. *Biophys. J.*, 83:2705–2715, 2002.
- [59] C. Rivetti, M. Guthold, and C. Bustamante. Scanning force microscopy of DNA deposited onto mica: Equilibration versus kinetic trapping studied by statistical polymer chain analysis. *J. Mol. Biol.*, 264:919–932, 1996.
- [60] C. Bustamante, S. B. Smith, J. Liphardt, and D. Smith. Single-molecule studies of DNA mechanics. *Curr. Opin. Struct. Biol.*, 10:279–285, 2000.
- [61] K. Rechendorff, G. Witz, J. Adamcik, and G. Dietler. Persistence length and scaling properties of single-stranded DNA adsorbed on modified graphite. *J. Chem. Phys.*, 131:095103, 2009.
- [62] S. Ramachandran, S. Komura, K. Seki, and G. Gompper. Dynamics of a polymer chain confined in a membrane. *Eur. Phys. J. E*, 34:11046–3, 2011.
- [63] A. J. Levine, T. B. Liverpool, and F. C. MacKintosh. Dynamics of rigid and flexible extended bodies in viscous films and membranes. *Phys. Rev. Lett.*, 93:038102, 2004.
- [64] A. J. Levine, T. B. Liverpool, and F. C. MacKintosh. Mobility of extended bodies in viscous films and membranes. *Phys. Rev. E*, 69:021503, 2004.

- [65] T. M. Fischer. The drag on needles moving in a Langmuir monolayer. *J. Fluid Mech.*, 498:123–137, 2004.
- [66] P. Dhar, T. M. Fischer, Y. Wang, T. E. Mallouk, W. F. Paxton, and A. Sen. Autonomously moving nanorods at a viscous interface. *Nano Lett.*, 6:66–72, 2006.
- [67] R. S. Dias. Solution behavior of nucleic acids. In R. S. Dias and B. Lindman, editors, *DNA Interactions with Polymers and Surfactants*. Wiley-Interscience, 2008.
- [68] H. Rozenberg, D. Rabinovich, F. Frolov, R. S. Hegde, and Z. Shakked. Structural code for DNA recognition revealed in crystal structures of papillomavirus E2-DNA targets. *Proc. Natl. Acad. Sci. USA*, 95:15194–15199, 1998.
- [69] *Nucleic Acid Database*. <http://ndbserver.rutgers.edu/atlas/xray/structures/B/bd0001/bd0001.html>.
- [70] T. Odijk. Polyelectrolytes near the rod limit. *J. Polym. Sci., Polym. Phys. Ed.*, 15:477–483, 1977.
- [71] J. Skolnick and M. Fixman. Electrostatic persistence length of a wormlike polyelectrolyte. *Macromolecules*, 10:944–948, 1977.
- [72] M. Ullner. Polyelectrolytes. Physicochemical aspects and biological significance. In R. S. Dias and B. Lindman, editors, *DNA Interactions with Polymers and Surfactants*. Wiley-Interscience, 2008.
- [73] E. P. Petrov, T. Ohrt, R. G. Winkler, and P. Schuille. Diffusion and segmental dynamics of double-stranded DNA. *Phys. Rev. Lett.*, 97:258101, 2006.
- [74] N. Makita, M. Ullner, and K. Yoshikawa. Conformational change of giant DNA with added salt as revealed by single molecular observation. *Macromolecules*, 39:6200–6206, 2006.
- [75] L. A. Day, C. J. Marzec, S. A. Reisberg, and A. Casadevall. DNA packing in filamentous bacteriophages. *Annu. Rev. Biophys. Chem.*, 17:509–539, 1988.
- [76] S. Fraden. Phase transition in colloidal suspensions of virus particles. In M. Baus, L. F. Rull, and J.P. Ryckaert, editors, *Observation, Prediction, and Simulation of Phase Transitions in Complex Fluids*. Kluwer Academic Publishers, 1995.
- [77] Z. Dogic and S. Fraden. Phase behavior of rod-like viruses and virus–sphere mixtures. In G. Gompper and M. Schick, editors, *Soft Matter, Vol. 2: Complex Colloidal Suspensions*. Wiley-VCH, 2006.

- [78] J. Tang and S. Fraden. Isotropic-cholesteric phase transition in colloidal suspensions of filamentous bacteriophage fd. *Liquid Crystals*, 19:459–467, 1995.
- [79] K. Zimmermann, H. Hagedorn, C. C. Heuck, M. Hinrichsen, and H. Ludwig. The ionic properties of the filamentous bacteriophages Pf1 and fd. *J. Biol. Chem.*, 261:1653–1655, 1986.
- [80] E. Barry, D. Beller, and Z. Dogic. A model liquid crystalline system based on rodlike viruses with variable chirality and persistence length. *Soft Matter*, 5:2563–2570, 2009.
- [81] R. Zantl, L. Baicu, F. Artzner, I. Sprenger, G. Rapp, and J. O. Rädler. Thermotropic phase behavior of cationic lipid–DNA complexes compared to binary lipid mixtures. *J. Phys. Chem. B*, 103:10300–10310, 1999.
- [82] A. A. Brian and H. M. McConnell. Allogeneic stimulation of cytotoxic T cells by supported planar membranes. *Proc. Natl. Acad. Sci. USA*, 81:6159–6163, 1984.
- [83] R. P. Richter, R. Bérat, and A. R. Brisson. Formation of solid-supported lipid bilayers: An integrated view. *Langmuir*, 22:3497–3505, 2006.
- [84] E. Thormann, A. C. Simonsen, L. K. Nielsen, and O. G. Mouritsen. Ligand-receptor interactions and membrane structure investigated by AFM and time-resolved fluorescence microscopy. *J. Mol. Recognit.*, 20:554–560, 2007.
- [85] M. I. Angelova and D. Dimitrov. Liposome electroformation. *Faraday Discuss.*, 81:303–311, 1986.
- [86] D. Dimitrov and M. I. Angelova. Lipid swelling and liposome formation mediated by electric fields. *Bioelectrochem. Bioenerg.*, 19:323–336, 1988.
- [87] M. I. Angelova, S. Soleau, P. Méléard, J. F. Faucon, and P. Bothorel. Preparation of giant vesicles by external AC electric fields. Kinetics and applications. *Progr. Colloid Polym. Sci.*, 89:127–131, 1992.
- [88] D. J. Estes and M. Mayer. Electroformation of giant liposomes from spin-coated films of lipids. *Colloids Surf. B*, 42:115–123, 2005.
- [89] H. Bouvrais, T. Pott, Luis A. B., J. H. Ipsen, and P. Méléard. Impact of membrane-anchored fluorescent probes on the mechanical properties of lipid bilayers. *Biochim. Biophys. Acta*, 1798:1333–1337, 2010.
- [90] H. S. Rye, S. Yue, D. E. Wemmer, M. A. Quesada, R. P. Haugland, R. A. Mathies, and A. N. Glazer. Stable fluorescent complexes of double-stranded DNA with bis-intercalating asymmetric cyanine dyes: properties and applications. *Nucl. Acids Res.*, 20:2803–2812, 1992.

- [91] C. Carlsson, M. Jonsson, and B. Akerman. Double bands in DNA gel-electrophoresis caused by bis-intercalating dyes. *Nucl. Acids Res.*, 23:2413–2420, 1995.
- [92] K. Günther, M. Mertig, and R. Seidel. Mechanical and structural properties of YOYO-1 complexed DNA. *Nucl. Acids Res.*, 38:6526–6532, 2010.
- [93] M. P. Lettinga, E. Barry, and Z. Dogic. Self-diffusion of rod-like viruses in the nematic phase. *Europhys. Lett.*, 71:692–698, 2005.
- [94] C. Kanony, B. Akerman, and E. Tuite. Photobleaching of asymmetric cyanines used for fluorescence imaging of single DNA molecules. *J. Am. Chem. Soc.*, 123:7985–7995, 2001.
- [95] C. J. R. Sheppard and P. Török. An electromagnetic theory of imaging in fluorescence microscopy, and imaging in polarization fluorescence microscopy. *Bioimaging*, 5:205–218, 1997.
- [96] M. Guizar-Sicairos and J. C. Gutierrez-Vega. Computation of quasi-discrete Hankel transforms of integer order for propagating optical wave fields. *J. Opt. Soc. Am. A*, 21:53–58, 2004.
- [97] A. Diaspro, editor. *Confocal and Two-Photon Microscopy: Foundations, Applications, and Advances*. Wiley-Liss, New York, 2002.
- [98] E. Abbé. Beiträge zur Theorie des Mikroskops und der mikroskopischen Wahrnehmung. *M. Schultze's Arch. Microsc. Anat.*, 9:413–468, 1873.
- [99] Lord Rayleigh. On the theory of optical images, with special reference to the microscope. *Phil. Mag.*, 54:167–195, 1896.
- [100] J. C. Crocker and D. G. Grier. Methods of digital video microscopy for colloidal studies. *J. Colloid Interf. Sci.*, 179:298–310, 1996.
- [101] D. Blair and E. Dufresne. <http://www.physics.georgetown.edu/matlab/index.html>.
- [102] M. K. Cheezum, W. F. Walker, and W. H. Guilford. Quantitative comparison of algorithms for tracking single fluorescent particles. *Biophys. J.*, 81:2378–2388, 2001.
- [103] R. E. Thompson, D. R. Larson, and W. W. Webb. Precise nanometer localization analysis for individual fluorescent probes. *Biophys. J.*, 82:2775–2783, 2002.
- [104] A. Yildiz, J. N. Forkey, S. A. McKinney, T. Ha, Y. E. Goldman, and P. R. Selvin. Myosin V walks hand-over-hand: single fluorophore imaging with 1.5-nm localization. *Science*, 300:2061–2065, 2003.

- [105] C. P. Brangwynne, G. H. Koenderink, E. Barry, Z. Dogic, F. C. MacKintosh, and D. A. Weitz. Bending dynamics of fluctuating biopolymers probed by automated high-resolution filament tracking. *Biophys. J.*, 93:346–359, 2007.
- [106] S. Wieser and G. J. Schütz. Tracking single molecules in the live cell plasma membrane – Do’s and Don’t’s. *Methods*, 46:131–140, 2008.
- [107] D. Freedman and P. Diaconis. On the histogram as a density estimator – L2 theory. *Z. Wahrscheinlichkeitstheorie*, 57:453–476, 1981.
- [108] M. Loose, E. Fischer-Friedrich, C. Herold, K. Kruse, and P. Schwille. Min protein patterns emerge from rapid rebinding and membrane interaction of MinE. *Nat. Struct. Mol. Biol.*, 18:577–583, 2011.
- [109] X. Michalet. Mean square displacement analysis of single-particle trajectories with localization error: Brownian motion in an isotropic medium. *Phys. Rev. E*, 82:041914, 2010.
- [110] A. J. Berglund. Statistics of camera-based single-particle tracking. *Phys. Rev. E*, 82:011917, 2010.
- [111] D. S. Martin, M. B. Forstner, and J. A. Käs. Apparent subdiffusion inherent to single particle tracking. *Biophys. J.*, 83:2109–2117, 2002.
- [112] M. Goulian and S. M. Simon. Tracking single proteins within cells. *Biophys. J.*, 79:2188–2198, 2000.
- [113] T. Savin and P. S. Doyle. Static and dynamic errors in particle tracking microrheology. *Biophys. J.*, 88:623–638, 2005.
- [114] Y. Han, A. M. Alsayed, M. Nobili, J. Zhang, T. C. Lubensky, and A. G. Yodh. Brownian motion of an ellipsoid. *Science*, 314:626–630, 2006.
- [115] F. Perrin. Mouvement brownien d’un ellipsoïde (I). Dispersion diélectrique pour des molécules ellipsoïdales. *J. Phys. Radium*, 5:497–511, 1934.
- [116] F. Perrin. Mouvement brownien d’un ellipsoïde (II). Rotation libre et dépolariation des fluorescences. Translation et diffusion de molécules ellipsoïdales. *J. Phys. Radium*, 7:1–11, 1936.
- [117] N. I. Hristova, M. I. Angelova, and I. Tsoneva. An experimental approach for direct observation of the interaction of polyanions with sphingosine-containing giant vesicles. *Bioelectrochem. Bioenerg.*, 58:65–73, 2002.

- [118] M. I. Angelova and I. Tsoneva. Interactions of DNA with giant liposomes. *Chem. Phys. Lipids*, 101:123–137, 1999.
- [119] I. Koltover, J. O. Rädler, and C. R. Safinya. Membrane mediated attraction and ordered aggregation of colloidal particles bound to giant phospholipid vesicles. *Phys. Rev. Lett.*, 82:1991–1994, 1999.
- [120] A. Fery, S. Moya, P.-H. Puech, F. Brochard-Wyart, and H. Mohwald. Interaction of polyelectrolyte coated beads with phospholipid vesicles. *C. R. Physique*, 4:259–264, 2003.
- [121] C. Herold, P. Schwille, and E. P. Petrov. DNA condensation at freestanding cationic lipid bilayers. *Phys. Rev. Lett.*, 104:148102, 2010.
- [122] F. Quemeneur, M. Rinaudo, G. Maret, and B. Pépin-Donat. Decoration of lipid vesicles by polyelectrolytes: mechanism and structure. *Soft Matter*, 6:4471–4481, 2010.
- [123] M. Laurencin, T. Georgelin, B. Malezieux, J.-M. Siaugue, and C. Ménager. Interactions between giant unilamellar vesicles and charged core-shell magnetic nanoparticles. *Langmuir*, 26:16025–16030, 2010.
- [124] D. J. Müller, D. Fotiadis, S. Scheuring, S. A. Müller, and A. Engel. Electrostatically balanced subnanometer imaging of biological specimens by atomic force microscope. *Biophys. J.*, 76:1101–1111, 1999.
- [125] M. G. Mason, L. S. Hung, C. W. Tang, S. T. Lee, K. W. Wong, and M. Wang. Characterization of treated indium–tin–oxide surfaces used in electroluminescent devices. *J. Appl. Phys.*, 86:1688–1692, 1999.
- [126] K. Sugiyama, H. Ishii, Y. Ouchi, and K. Seki. Dependence of indium–tin–oxide work function on surface cleaning method as studied by ultraviolet and x-ray photoemission spectroscopies. *J. Appl. Phys.*, 87:295–298, 2000.
- [127] R. Peters and R. J. Cherry. Lateral and rotational diffusion of bacteriorhodopsin in lipid bilayers: experimental test of the Saffman-Delbrück equations. *Proc. Natl. Acad. Sci. USA*, 79:4317–4321, 1982.
- [128] S. Ramadurai, A. Holt, V. Krasnikov, G. van den Bogaart, J. A. Killian, and B. Poolman. Lateral diffusion of membrane proteins. *J. Am. Chem. Soc.*, 131:12650–12656, 2009.
- [129] R. E. Waugh. Surface viscosity measurements from large bilayer vesicle tether formation. I. Analysis. *Biophys. J.*, 38:19–27, 1982.

- [130] B. A. Camley, C. Esposito, T. Baumgart, and F. L. H. Brown. Lipid bilayer domain fluctuations as a probe of membrane viscosity. *Biophys. J.*, 99:L44–L46, 2010.
- [131] K. Velikov, C. Dietrich, A. Hadjiisky, K. Danov, and B. Pouligny. Motion of a massive microsphere bound to a spherical vesicle. *Europhys. Lett.*, 40:405–410, 1997.
- [132] R. Dimova, C. Dietrich, A. Hadjiisky, K. Danov, and B. Pouligny. Falling ball viscosimetry of giant vesicle membranes: finite-size effects. *Eur. Phys. J. B*, 12:589–598, 1999.
- [133] M. Anton. Interaction of Charged Colloidal Beads with Oppositely Charged Freestanding Lipid Membranes. Diploma thesis, Technische Universität Dresden, 2011.
- [134] L. Ramos, T. C. Lubensky, N. Dan, P. Nelson, and D. A. Weitz. Surfactant-mediated two-dimensional crystallization of colloidal crystals. *Science*, 286:2325–2328, 1999.
- [135] H. Aranda-Espinoza, Y. Chen, N. Dan, T. C. Lubensky, P. Nelson, L. Ramos, and D. A. Weitz. Electrostatic repulsion of positively charged vesicles and negatively charged objects. *Science*, 285:394–397, 1999.
- [136] J. Kestin, M. Sokolov, and W. A. Wakeham. Viscosity of liquid water in the range -8 °C to 150 °C. *J. Phys. Chem. Ref. Data*, 7:941–948, 1978.
- [137] T. M. Fischer, P. Dhar, and P. Heinig. The viscous drag of spheres and filaments moving in membranes or monolayers. *J. Fluid Mech.*, 558:451–475, 2006.
- [138] M. Sickert, F. Rondelez, and H. A. Stone. Single-particle Brownian dynamics for characterizing the rheology of fluid Langmuir monolayers. *Europhys. Lett.*, 79:66005, 2007.
- [139] C. Tribet and F. Vial. Flexible macromolecules attached to lipid bilayers: impact on fluidity, curvature, permeability and stability of the membranes. *Soft Matter*, 4:68–81, 2008.
- [140] P. Nelson. *Biological Physics: Energy, Information, Life*. W. H. Freeman, 2004.
- [141] J. O. Rädler, I. Koltover, T. Salditt, and C. R. Safinya. Structure of DNA-cationic liposome complexes: DNA intercalation in multilamellar membranes in distinct interhelical packing regimes. *Science*, 275:810–814, 1997.
- [142] D. D. Lasic, H. Strey, M. C. A. Stuart, R. Podgornik, and P. M. Frederik. The structure of DNA-liposome complexes. *J. Am. Chem. Soc.*, 119:832–833, 1997.
- [143] A. R. Thierry, V. Norris, F. Molina, and M. Schmutz. Lipoplex nanostructures reveal a general self-organization of nucleic acids. *Biochim. Biophys. Acta*, 1790:385–394, 2009.

- [144] V. A. Bloomfield. DNA condensation. *Curr. Opin. Struct. Biol.*, 6:334–341, 1996.
- [145] A. A. Zinchenko, O. A. Pyshkina, A. V. Lezov, V. G. Sergeyev, and K. Yoshikawa. Single DNA molecules: compaction and decompaction. In R. S. Dias and B. Lindman, editors, *DNA Interactions with Polymers and Surfactants*, pages 59–88. John Wiley & Sons, Inc., 2008.
- [146] E. G. Nabel, G. Plautz, and G. J. Nabel. Site-specific gene expression in vivo by direct gene transfer into the arterial wall. *Science*, 249:1285–1288, 1990.
- [147] M. B. Hochrein, J. A. Leierseder, L. Golubović, and J. O. Rädler. DNA molecules on periodically microstructured lipid membranes: localization and coil stretching. *Phys. Rev. E*, 75:021901, 2007.
- [148] C. Herold, G. Chwastek, P. Schwille, and E. P. Petrov. Efficient electroformation of supergiant unilamellar vesicles containing cationic lipids on ITO-coated electrodes. *Langmuir*, 28:5518–5521, 2012.
- [149] S. M. Mel’nikov, R. S. Dias, Y. S. Mel’nikova, E. F. Marques, M. G. Miguel, and B. Lindman. DNA conformational dynamics in the presence of catanionic mixtures. *FEBS Lett.*, 453:113–118, 1999.
- [150] Y. Sato, S. M. Nomura, and K. Yoshikawa. Enhanced uptake of giant DNA in cell-sized liposomes. *Chem. Phys. Lett.*, 380:279–285, 2003.
- [151] C.-Y. Shew and K. Yoshikawa. Mean field theory for the intermolecular and intramolecular conformational transitions of a single flexible polyelectrolyte chain. *J. Chem. Phys.*, 126:144913, 2007.
- [152] A. A. Zinchenko, V. G. Sergeyev, S. Murata, and K. Yoshikawa. Controlling the intrachain segregation on a single DNA molecule. *J. Am. Chem. Soc.*, 125:4414–4415, 2003.
- [153] S. M. Melnikov, V. G. Sergeyev, and K. Yoshikawa. Discrete coil–globule transition of large DNA induced by cationic surfactant. *J. Am. Chem. Soc.*, 117:2401–2408, 1995.
- [154] C. Fleck, R. R. Netz, and H. H. von Grünberg. Poisson-Boltzmann theory for membranes with mobile charged lipids and the pH-dependent interaction of a DNA molecule with a membrane. *Biophys. J.*, 82:76–92, 2002.
- [155] R. S. Dias, A. A. C. C. Pais, P. Linse, M. G. Miguel, and B. Lindman. Polyion adsorption onto catanionic surfaces. A Monte Carlo study. *J. Phys. Chem. B*, 109:11781–11788, 2005.

- [156] S. Tzlil and A. Ben-Shaul. Flexible charged macromolecules on mixed fluid lipid membranes: theory and Monte Carlo simulations. *Biophys. J.*, 89:2972–2987, 2005.
- [157] Y. W. Kim and W. Sung. Membrane curvature induced by polymer adsorption. *Phys. Rev. E*, 63:041910, 2001.
- [158] V. Kahl, M. Hennig, B. Maier, and J. O. Rädler. Conformational dynamics of DNA-electrophoresis on cationic membranes. *Electrophoresis*, 30:1276–1281, 2009.
- [159] D. Harries, S. May, W. M. Gelbart, and A. Ben-Shaul. Structure, stability, and thermodynamics of lamellar DNA-lipid complexes. *Biophys. J.*, 75:159–173, 1998.
- [160] S. Tristram-Nagle, H. I. Petrache, and J. F. Nagle. Structure and interactions of fully hydrated dioleoylphosphatidylcholine bilayers. *Biophys. J.*, 75:917–925, 1998.
- [161] M. Wheeler, X. Cortez-Gonzalez, R. Frazzi, and M. Zanetti. Ex vivo programming of antigen-presenting B lymphocytes: considerations on DNA uptake and cell activation. *Int. Rev. Immunol.*, 25:83–97, 2006.
- [162] J. Villemejeane and L. M. Mir. Physical methods of nucleic acid transfer: general concepts and applications. *Br. J. Pharmacol.*, 157:207–219, 2009.
- [163] S.-P. Riechers, U. Stahl, and C. Lang. Endocytic uptake of fluorescence labelled DNA in yeast. *J. Basic Microbiol.*, 50:83–89, 2010.
- [164] R. M. Bennett, G. T. Gabor, and M. M. Merritt. DNA binding to human leukocytes. Evidence for a receptor-mediated association, internalization, and degradation of DNA. *J. Clin. Invest.*, 76:2182–2190, 1985.
- [165] V. Budker, T. Budker, G. Zhang, V. Subbotin, A. Loomis, and J. A. Wolff. Hypothesis: naked plasmid DNA is taken up by cells in vivo by a receptor-mediated process. *J. Gene Med.*, 2:76–88, 2000.
- [166] A. Wittrup, S. Sandgren, J. Lilja, C. Bratt, N. Gustavsson, M. Mörgelin, and M. Belting. Identification of proteins released by mammalian cells that mediate DNA internalization through proteoglycan-dependent macropinocytosis. *J. Biol. Chem.*, 282:27897–27904, 2007.
- [167] M. Gudmand, M. Fidorra, T. Bjørnholm, and T. Heimburg. Diffusion and partitioning of fluorescent lipid probes in phospholipid monolayers. *Biophys. J.*, 96:4598–4609, 2009.
- [168] R. D. Klausner and D. E. Wolf. Selectivity of fluorescent lipid analogs for lipid domains. *Biochemistry*, 19:6199–6203, 1980.

-
- [169] A. V. Dobrynin and J. M. Y. Carrillo. Swelling of biological and semiflexible polyelectrolytes. *J. Phys.: Condens. Matter*, 21:424112, 2009.
- [170] S. F. Edwards. Statistical mechanics of polymers with excluded volume. *Proc. Phys. Soc. London*, 85:613–624, 1965.
- [171] M. D. Wang, H. Yin, R. Landick, J. Gelles, and S. M. Block. Stretching DNA with optical tweezers. *Biophys. J.*, 72:1335–1346, 1997.
- [172] N. Yoshinaga, K. Yoshikawa, and S. Kidoaki. Multiscaling in a long semiflexible polymer chain in two dimensions. *J. Chem. Phys.*, 116:9926–9929, 2002.

Acknowledgements

The research presented in this doctoral thesis has been carried out between October 2007 and June 2012 at the Biotechnology Center (BIOTEC) of the Technische Universität Dresden in the laboratory of Prof. Dr. Petra Schwille. Although only my name appears on the cover of this dissertation, numerous people have contributed to this work. Hereby, I would like to acknowledge the individuals whose efforts not only provided scientific advancement, but also turned the last years into a memorable and greatly appreciated enjoyment.

Petra, I would like to express my deep and sincere gratitude to you. Thank you for giving me the wonderful opportunity to conduct my doctoral research in your group and for providing a fantastic working environment. Thank you also for your untiring and dedicated support, the freedom to pursue my own ideas and the financial means to allow for my research and the presentation thereof at numerous conferences around the world.

I would like to thank Prof. Dr. Josef A. Käs for kindly agreeing to review this thesis.

Eugene, you are a great mentor and friend to me. Your contribution to the success of this thesis is truly invaluable. Thank you for always being available, motivating and supportive; for sharing your extensive knowledge and commitment; for sharing my excitement about newly obtained scientific results; for all the critical and constructive discussions; and for being my proofreader in chief.

Grzesiek, thank you for our enjoyable collaboration and your help with the AFM measurements.

I would also like to thank Pavlik Lettinga, Forschungszentrum Jülich, for supplying a stock of labeled *fd*-virus particles and making us aware of this handy model system in the first place.

I thank the Deutsche Forschungsgemeinschaft for funding of the research project via Forschergruppe 877, “From Local Constraints to Macroscopic Transport”.

Furthermore, I would like to express my gratitude to Claudia and Susanne for handling the

bureaucracy in such miraculous ways that it almost appeared as if there was none.

My outmost appreciation goes to Karin, the heart and soul of our group, who always helps out a physicist who wandered off to the biochemistry lab.

I want to thank all past and present members of Petra's group and the people who share our floor for all the little things that might be easily forgotten but are essential for the daily work. Thank you for the great atmosphere, plenty of fruitful discussions and suggestions, as well as fun inside and outside the lab. Special thanks go to Jörg, Jens, Thomas O., Deef, Friedrich, Mohammed, Jonas, Salvo, Jakob, Madhavi, Martin, Heiko, Zdenek, Markus A., Ana, Franziska, Wolfgang, Markus B., Thomas W., Viktoria, Fabian, Sven, Ilaria, Remi, Dolores, Erdinc, Senthil, Oleg, Robert S. and Elke.

I thank all members of the Sächsische Forschergruppe for interesting and productive discussions.

Ich danke meinen Eltern, Großeltern und Geschwistern die mich unterstützen seit ich denken kann, und auch davor. Und nicht zuletzt, Stephanie, danke für all deine Unterstützung, deine Toleranz gegenüber meiner festen Überzeugung, dass die besten Ergebnisse in Nachtschichten erzielt werden, und deine Liebe die mich trägt.

Declaration

Hiermit versichere ich, dass ich die vorliegende Arbeit ohne unzulässige Hilfe Dritter und ohne Benutzung anderer als der angegebenen Hilfsmittel angefertigt habe; die aus fremden Quellen direkt oder indirekt übernommenen Gedanken sind als solche kenntlich gemacht. Die Arbeit wurde bisher weder im Inland noch im Ausland in gleicher oder ähnlicher Form einer anderen Prüfungsbehörde vorgelegt.

Ich erkenne die Promotionsordnung der Fakultät Mathematik und Naturwissenschaften der Technischen Universität Dresden an.

Dresden, 08. Juni 2012

Christoph Herold